LIÈGE université Library

https://lib.uliege.be

https://matheo.uliege.be

Microstructural Characterization and Mechanical Properties of Inconel 718 Produced by LPBF Using Optimized Processing Parameters

Auteur : Ouchem, Yassine
Promoteur(s) : Tchuindjang, Jérôme Tchoufack; Mertens, Anne
Faculté : Faculté des Sciences appliquées
Diplôme : Master en ingénieur civil en aérospatiale, à finalité spécialisée en "aerospace engineering"
Année académique : 2025-2026
URI/URL : http://hdl.handle.net/2268.2/26186

Avertissement à l'attention des usagers :

Tous les documents placés en accès ouvert sur le site le site MatheO sont protégés par le droit d'auteur. Conformément aux principes énoncés par la "Budapest Open Access Initiative"(BOAI, 2002), l'utilisateur du site peut lire, télécharger, copier, transmettre, imprimer, chercher ou faire un lien vers le texte intégral de ces documents, les disséquer pour les indexer, s'en servir de données pour un logiciel, ou s'en servir à toute autre fin légale (ou prévue par la réglementation relative au droit d'auteur). Toute utilisation du document à des fins commerciales est strictement interdite.

Par ailleurs, l'utilisateur s'engage à respecter les droits moraux de l'auteur, principalement le droit à l'intégrité de l'oeuvre et le droit de paternité et ce dans toute utilisation que l'utilisateur entreprend. Ainsi, à titre d'exemple, lorsqu'il reproduira un document par extrait ou dans son intégralité, l'utilisateur citera de manière complète les sources telles que mentionnées ci-dessus. Toute utilisation non explicitement autorisée ci-avant (telle que par exemple, la modification du document ou son résumé) nécessite l'autorisation préalable et expresse des auteurs ou de leurs ayants droit.

UNIVERSITE DE LIEGE
FACULTE DES SCIENCES APPLIQUEES

Microstructural Characterization and Mechanical Properties of Inconel 718 Produced by LPBF Using Optimized Processing Parameters

Ouchem Yassine

Thesis presented to obtain the degree of :
Master of Science in Aerospace Engineering

Thesis supervisors :
Tchuindjang Jerome Tchoufang
Mertens Anne

Academic year: **2025 - 2026**

Acknowledgments

First and foremost, I would like to thank Professor Anne Mertens, Head of the Laboratory and co-supervisor of this work, for giving me the chance to join the Metallic Materials Science Laboratory and pursue this research project in such a stimulating environment.

I would also like to thank Abdul Herrim Seidou for his valuable advice, availability, and guidance throughout this project, as well as Olivier Dedry for his assistance during this work.

My thanks also go to Sylvie Salieri and Antonio Martinez Aguilera for their contribution, invaluable assistance, and good spirits, which made this semester both enriching and enjoyable.

Finally, I would like to express my deepest gratitude to my supervisor, Jérôme Tchoufang Tchuindjang, for his supervision, availability, insightful advice, and the time he dedicated to me throughout this work. His guidance was instrumental in the successful completion of this project.

To all of these individuals, I extend my heartfelt thanks.

Abstract

Inconel 718, largely used in many fields of activity, is one of the superalloys which can be manufactured by additive methods such as Laser powder bed fusion. This method involves many parameters which impact the material properties. This work focuses on the variation in the laser power, scan speed, scanning strategy and the impact of a 200°C preheating temperature of the base plate. Twenty 1 cm^3 cubic samples were printed with varying laser power in the range of 100-200 W and scan velocities in the range of 700-1000 mm/s while keeping the hatch spacing constant at 80 μm and the layer thickness at 30 μm using a 90° scanning strategy. The cube densities were measured using a gas pycnometer and an internal porosity characterisation was conducted using an optical microscope. These cubes were used to study the melt pool shape, also using an optical microscope and the cellular microstructure, the chemical composition and the grain geometry using scanning electron microscopy. Macro-, micro- and nano-hardness tests were performed using HV10, HV0.3 and an indentation depth of 500 nm, respectively. In parallel, four 20 x 40 x 30 mm blocks using 900 mm/s scan speed, 200 W laser power, the same hatch spacing and layer thickness as the cubes, but using 90° and 67° scanning strategies were printed. These blocks were used for grain characterisation and macro- and micro-hardness tests were performed in the same way as for the cubes. Tensile specimens were machined perpendicular to the building direction for uniaxial tensile tests followed by a fractographic analyses. The results of these tests highlighted significant differences in the mechanical properties between the scanning strategies. The 67° strategy gives a higher Young's modulus, yield strength and ultimate tensile strength but all specimens presented a ductile failure mode. The 200°C preheating temperature allows the production of near fully dense material with a relative density higher than 99.7% while mitigating the formation of hot cracks and oxide inclusions. A higher VED tends to monotonically increase the melt pool (MP) depth, while the grain size first decreases, reaches a minimum, and then increases. The grains maintain a fan-shaped morphology since the VED* range is restricted due to the already optimised processing parameter window studied here.

Contents

Introduction **1**

1 State of the art **3**
1.1 Inconel alloy . . . 3
1.1.1 Inconel types . . . 3
1.1.2 Inconel 718 . . . 4
1.2 Conventional manufacturing methods for In718 . . . 6
1.3 Additive manufacturing methods . . . 6
1.3.1 AM of Inconel . . . 8
1.3.2 LPBF technique . . . 9
1.3.2.1 Impact of parameters on porosity/density . . . 10
1.3.2.2 Preheated base plate . . . 12
1.3.2.3 Energy measurement . . . 13
1.3.2.4 Scan direction . . . 15
1.3.3 Microstructure in AM . . . 16
1.4 Mechanical properties . . . 18
1.5 Mixed powder . . . 19

2 Materials and methods **21**
2.1 LPBF machine . . . 21
2.2 Powder . . . 23
2.3 Jobs parameters and configurations . . . 23
2.3.1 Cuboid samples . . . 23
2.3.2 Blocks . . . 24
2.4 Profilometer analysis . . . 25
2.5 Blocks purposes . . . 26
2.5.1 Machining equipment . . . 26
2.5.2 Tensile specimens design and machining approach . . . 27
2.5.3 Tensile test approach and equipment . . . 28
2.6 Samples preparation . . . 29
2.7 Density and porosity characterisation . . . 31
2.7.1 Pycnometer measurement . . . 31

2.7.2 Optical microscope . . . 32
2.8 Macro- and Micro-hardness measurements . . . 33
2.8.1 Equipment used . . . 33
2.8.2 Hardness on cubic samples . . . 34
2.8.3 Hardness on slices from the block . . . 35
2.9 Nano-indentation analysis . . . 36
2.9.1 Equipment used . . . 36
2.9.2 Experimental approach . . . 38
2.10 Scanning electron microscope (SEM) analysis . . . 38
2.10.1 Equipment . . . 38
2.10.2 Samples preparation . . . 39
2.10.3 Analyses conducted . . . 40

3 Results **41**
3.1 Cubes analysis . . . 41
3.1.1 Density . . . 41
3.1.1.1 Pycnometer analysis . . . 41
3.1.1.2 Optical microscope analysis . . . 43
3.1.2 Melt pool (MP) characterisation . . . 47
3.1.3 Microstructure characterisation . . . 49
3.1.3.1 Cellular structure and chemical composition . . . 49
3.1.3.2 Grain size characterisation . . . 51
3.1.4 Hardness analysis . . . 52
3.1.4.1 Macro- and micro-hardness . . . 52
3.1.4.2 Nanohardness . . . 53
3.2 Blocks analysis . . . 56
3.2.1 Block top surfaces roughness . . . 57
3.2.2 Macro- and micro-hardness on the slices . . . 61
3.2.3 Grain morphology . . . 62
3.2.4 Tensile specimens analysis . . . 63
3.2.4.1 Verification of failure section locations . . . 63
3.2.4.2 Tensile tests . . . 64
3.2.4.3 Fractographic analysis . . . 65

4 Discussions **68**
4.1 Validation of 200 °C as optimal experimental preheating temperature . . . 68
4.2 Impact of VED on material properties . . . 70
4.3 Impact of scanning strategy on microstructure and mechanical properties . . . 73

5 Conclusions and perspectives **75**
5.1 Conclusions . . . 75
5.2 Perspectives . . . 76

Appendices **78**
i 78
ii 79
iii 80
iv 81
v 83
vi 84
vii 84
viii 86
ix 87

Bibliographie **88**

List of Figures

1.1 Crystal structure of the principal phases in Inconel 718. a):FCC, b): cubic ($L1_2$), c)BCT. [44] 5
1.2 Scheme of LPBF system. [51] 8
1.3 Scheme of melt pools and laser track on a powder bed. [1] 10
1.4 a) Theoretical PV processing map with different defect areas. b) Melt pool shape for each mode. Scheme of melt pool sections c) optimal mode, d) lack of fusion, e) balling, f) keyhole. [4] 11
1.5 Optical micrographs with different PV values, a,b) Gas porosity, c,d) Optimal mode, e,f) Lack of fusion. [27] 12
1.6 Scheme of scanning strategies: a) with different rotation angles betwen layers [75], b) island scan with a90° rotation angle. [36] 15
1.7 Microstructure formation modes as a function of temperature gradient and solidification rate [34]. 17
1.8 SEM images of melt pools with a) CLM, b) SCM, c) PCM. [21] 17

2.1 Aconity mini LPBF system with the build area on the left and control panel on the right. [5] 22
2.2 Top view of the twenty cubes on the build platform preheated at 200°C and varying scan speed and laser power. 24
2.3 Arrangement of the blocks on the build platform with Autodesk Netfabb software, a) side view and b) top view with scanning strategy rotation angles. 25
2.4 Alicona - Infinite Focus G5 Profilometer. [64] 26
2.5 Electrical Discharge Machine Robofil 310 by Charmilles Technologies. [20] 27
2.6 Scheme of a) a block and b) a tensile specimen with dimensions in mm [68] 27
2.7 Arrangement of tensile specimens within the block, a) side view and b) top view. 28
2.8 Scheme of the location of the cutting section with regard to the building direction and the top layer scan direction on cuboid sample. 29
2.9 Metallographic automatic cutter Micracut 202 from Metkon [39]. 29
2.10 Samples embedded in Bakelite cylinder after polishing. 30
2.11 Hot mounting press Citopress-1 supplied by Struers. [54] 30
2.12 Polishing machine Tegramin-30 supplied by Struers. [55] 31

2.13 Gas pycnometer AccuPyc II 1340 by Micromeritics. [46]. 31
2.14 Microscope BX60M by Olympus [10]. 32
2.15 Shape of the top right indentation on sample 19, a) mark after macro hardness test observed with 10× magnification OM, b) mark after micro hardness test observed using 20× magnification OM. 33
2.16 Automatic hardness tester Falcon 500 G2 by Innovatest. [29] 34
2.17 Locations of macro- and micro-hardness indentations on cubic sample cross-section embedded in Bakelite, a) indentation on samples 19 observed using OM at 2.5× magnification, b) scheme of indented sample with the dimensions of the grids. 35
2.18 Surfaces highlighted in green on remaining material after machining corresponding the area used for macro- and micro-hardness tests, with a) surface along x and b) surface along y. 36
2.19 Locations of macro- and micro-hardness indentations on cross-section along x and along y inside slices, with micro-indentations in red frames. 36
2.20 Hysitron TI 980 Nanoindenter [8]. 37
2.21 41 x 41 nano-indentation grid on sample 12 observed with OM using a) 2.5x magnification and b) 20x magnification. 38
2.22 Tescan Clara scanning electron microscope with ultra-hight resolution multimodal imaging [62]. 39
2.23 Samples after chemical treatment with silver paint near the first layer. . . . 39

3.1 a) Sample densities and b) relative densities as a function of VED^* with the reference density of 8.19 g/cm^3 indicated with the green line and the near fully dense material threshold of 99.7% indicated with the red dashed line. 42
3.2 PV processing map 43
3.3 Linear and quadratic regression of the relative surface density values obtained with OM as a function of the relative densities obtained from pycnometer measurements. 44
3.4 Cross-section view of sample 7 on the right and sample 8 on the left with 2.5x magnification. 45
3.5 Cross-section of samples with the best internal densities observed using OM at 2.5x magnification. 46
3.6 Cross-section view of: a) sample 13 and b) sample 17 at 2.5x magnification showing spherical porosity corresponding to entrapped gas during solidification. 47
3.7 a) Optical microscope view of sample 1 cross-section observed with 2.5x magnification b) close-up view showing porosity with characteristic lack of fusion shape observed with 10x magnification. 47
3.8 Characterisation of melt pool geometry for sample 11 using Stream Motion software using a 20x magnification lens. 48

3.9 Melt pool dimensions as a function of VED* with a) the melt pool depth of the first layer and b) the curvature radius. 48
3.10 Linear EDX analysis locations on a) sample 19 and b) sample 17. 49
3.11 a) Mass percentage, b) atomic percentage obtained from EDX analysis on sample 17 along the straight line in c), enhancing the local chemical gradients due to the cellular-like structure. 50
3.12 a) Mass percentage, b) atomic percentage obtained by EDX analysis on sample 19 along the straight line in c). 51
3.13 EBSD analysis performed near the top layer in the XZ plane of a) sample 12 with VED* = 72.01 J/mm^3, b) sample 11 with VED*=80.01 J/mm^3, c) sample 15 with VED* = 93.35 J/mm^3, d) sample 19 with VED* = 106.69 J/mm^3 52
3.14 Vickers hardness values of each sample with a) macro-hardness (HV10) and b) micro-hardness (HV0.3). 53
3.15 41 x 41 nano indentation grids near the last layer covering a 300 x 300 μm^2 areas with imposed depth of 500 μm on a) sample 12, b) sample 15 and c) sample 19. 53
3.16 Nanohardness of a) sample 12 and b) sample 15 and c) sample 19 with imposed displacement of 500 μm on 41x41 indentation grid. 54
3.17 Histogram of nanohardness frequency in a) sample 12, b) sample 15 and c) sample 19. 55
3.18 Top view of the 4 blocks at the end of the printing process, on the build platform preheated to 200°C, with 90° scanning strategy top left and bottom right and 67° top right and bottom left. 56
3.19 Top layer roughness obtained with a 90° scanning strategy with a,b) block 1 and c,d) block 4. 57
3.20 Top layer roughness obtained with a 67° scanning strategy with a,b) block 2 and c,d) block 3. 58
3.21 Histogram of peak height and valley depth distributions on the top layer. . 60
3.22 Hardness in sections parallel to the x and y directions in each slices with a) macro-hardness (HV10) and b) micro-hardness (HV0.3). 61
3.23 EBSD analysis of slices with cross-section in YZ plane with a) 90° scanning strategy, b) 67° scanning strategy with equiaxed grains highlighted in white rectangle, c) close-up view on the center of the ROI with cup-shaped grains. 63
3.24 Post-fracture gauge length measurements from the failure section to the grip section edge of TS1 using Stream Motion software with OM. 64
3.25 Stress as a function of strain in tensile specimens under unidirectional tensile tests with a) a 90° scanning strategy and b) a 67° scanning strategy. . . . 64
3.26 Fractography of TS3 with a) overview of the fracture section with rough central area inside dashed line corresponding to the fracture initiation, b) close-up view on dimples and flat area, c) close-up view on secondary crack causing a step-like structure with sheared dimples. 66

3.27 a) Highly irregular and rough area on fracture section of TS2, b) close-up view on red rectangle in Figure a) showing sheared dimples. 67
3.28 a) Porosity surrounded by dimples in TS5, b) Al oxide inclusion surrounded by dimples in TS1', c) Smearing area in TS3'. 67

4.1 PV processing map of the twenty cubic samples with different porosity regions and optimal window, showing iso-VED* lines and highlighting the near fully dense samples with relative densities above 99.7% 69
4.2 Comparison of hardness between samples printed using a 200°C preheating temperature from this work and samples printed using 80°C, 300°C and 500°C from previous research [60] with a) macro-hardness HV10 and b) micro-hardness HV0.3. 72

A.1 Threshold used for porosity percentage estimation with OM analysis, with sample 1 on the right and sample 2 on the left. 79
A.2 EDX mapping of porosity on sample 17 (P=200 W, V=700 mm/s). 81
A.3 EDX mapping of porosity on sample 17 (P=200 W, V=700 mm/s). 82
A.4 Precedent tensile specimen designs leading to unsuccessful results with same gauge dimensions and the same total length, with dimensions in mm. . . . 84
A.5 Fracture section of tensile specimens printed using a 90° scanning strategy. 84
A.6 Fracture section of tensile specimens printed using a 67° scanning strategy. 85
A.7 Composition spectrum obtained by EDX analyses inside and around oxide inclusion on fracture section of TS1'. 86
A.8 Kernel average misorientation (KAM) of a) slice 1 and b) slice 1'. 87

List of Tables

1.1 Chemical composition in weight percentage of the principal elements of different type of Inconel. [30] [56] 4
1.2 Chemical formulas, crystal structures and roles and effects of the phases present in Inconel 718. [44] [31] 6

2.1 Chemical composition in weight percentage of Inconel 718 powder from VDM Metals GmbH [60] 23

3.1 Density and relative density obtained from pycnometer and 2D optical cross-sections analysis respectively, with scan speed and laser power and the corresponding classical and modified VED of each sample. 42
3.2 Relative densities obtained with pycnometer measurements and relative surface densities obtained with OM with the corresponding VED^*. 44
3.3 Melt pool dimensions for varying VED* obtained with optical microscope measurements. 49
3.4 Height parameters of peaks and valleys on the four block top surfaces. . . . 59
3.5 Mean Values (MV) and Standard Deviation (SD) of macro- and microhardness in x and y directions of each slice. 62
3.6 Post-fracture gauge length measured from the fracture section to the edge of the grip section. 63
3.7 Mechanical properties (i.e., Young's modulus, yield strength, ultimate tensile strength, and elongation) obtained by DIC from tensile tests on specimens printed using 90° and 67° scanning strategies compared with literature data from [12] and [52], both using a 67° scanning strategy and a 200°C and 80°C preheating temperature respectively. 65

A.1 Iterations of density measurement with pycnometer and their averages for each cubic sample. 78
A.2 Areas of interest measured using Image J for each sample for porosity percentage estimation with OM. 80
A.3 Mean Values (MV) and Standard Deviation (SD) of macro- and microhardness of each sample. 83

Introduction

For several years, additive manufacturing of metallic materials has generated a great deal of interest in many fields related to engineering because of the complex shape and potential material savings. However, the phenomena involved during the manufacturing process are very different from what is already known with conventional methods and sometimes lead to very different properties for the same material. Many parameters directly chosen by the user have an important impact on the properties of the final part and therefore need to be studied.

Due to the number of processing parameters involved in an additive manufacturing technique such as LPBF, experimental research is a long and laborious process. Therefore, there is a real need to develop accurate simulation models. They must be able to predict the microstructure formed or the appropriate post-treatment to apply when processing parameters vary. The final goal is of course to predict the associated mechanical properties of the material and find the optimal set of parameters. This study is part of a longer research programme originally launched to provide experimental results for a project called "Smart Enhancement of Ni-based superalloys for-Additive-Manufacturing towards improved creep resistance at high temperature (Sensam+)", in which three different teams are involved. The project wants to improve the mechanical properties, more specifically the creep behaviour of Ni-based superalloy, printed by LPBF techniques. Two teams work on numerical simulations: one focuses on the process modelling and the second on the material behaviour modelling. The first team works with a PFEM model to predict the microstructure formed by simulating the phenomena encountered in the melt pool and tries to find the most suitable heat treatment to apply. In addition, a team focusing on experimental data, also allows to validate experimentally the results at the end of the simulation. The second team working on simulations links the microstructure to the creep behaviour by developing Phase Field and Representative Volume Element model.

The aim of this study is to characterise the microstructure and the mechanical properties of Inconel 718 obtained using the LPBF technique, to find the most suitable set of printing parameters. The study is based on previous research which is presented in Tchuindjang et al. (2026) [60], where different base plate temperatures are compared. Considering the identified optimal preheating temperature, the goal here is to identify the optimal processing window to reach a nearly fully dense material with enhanced mechanical properties.

Different tests at different scales were conducted to analyse the behaviour and the microstructure of the material. The analyses are divided in two parts conducted in parallel: the first is the analysis of twenty samples printed with varying laser scan speeds and laser powers, the second part focuses on the analysis of larger blocks printed using different scanning strategy in which tensile specimens are machined. The samples allow the analysis of the different kinds of porosity encountered with LPBF while the tensile specimens give the behaviour of the material under tensile stress, depending on scan rotation angle. Then, both types of sample, the cubes and the blocks can be analysed to study the microstructure and the hardness. In that way, all the results can be linked to compare and understand the impact of the processing parameters on the final material.

Therefore, this work provides a state-of-the-art overview of the properties of the alloy and the associated manufacturing methods. It then details all the equipments and methods used for the analyses and presents all the results obtained. A discussion of these results is provided, followed by a conclusion and possible future analyses.

Chapter 1

State of the art

1.1 Inconel alloy

Inconel is a superalloy developed in the 1940s by the International Nickel Company. Superalloys are specific materials made of several metallic constituents that exhibit very high mechanical properties even at high temperatures and can resist extreme conditions. There exist various families of superalloys which are classified according to their principal element; these are cobalt-based, iron-based, and nickel-based superalloys [51] [50].

Inconel is a nickel-based alloy; the second most important element is chromium (Cr). The other elements are molybdenum (Mo), iron (Fe), cobalt (Co), niobium (Nb), titanium (Ti), and aluminium (Al). Inconel was developed to have an excellent resistance to corrosion and to remain stable at high temperatures due to the nickel matrix with a face-centred cubic (FCC) structure, shown in Fig.1.1a, which is stable up to 1450°C [44]. It is also characterised by low rates of diffusion, a high fatigue resistance, a good wear resistance, a good creep behaviour, a high strength, and the FCC matrix also confers ductility and toughness [51] [30].

Inconel can keep its mechanical properties in a temperature range between -252 and 650°C [32]. With such capabilities, Inconel is used in harsh environments. Indeed, Inconel was created to be used in demanding application fields in terms of material properties such as aerospace and energy for turbine blades, combustion chambers, gas turbines, nuclear power plants and heat exchanger equipment, or even for oil and gas systems [2] [76].

1.1.1 Inconel types

Many types of Inconel have been developed, they all exhibit similar characteristics listed above, but each has its own specificities and they have been developed for specific applications [30]. A few of them are listed in the following Table 1.1 with their principal constituents. A slight variation in the mass proportion of certain elements leads to signifi-

cant variation in the mechanical properties of the material. Other elements may be present in smaller quantities such as carbon, sulphur and phosphorus.

As can be seen in Table 1.1 the mass proportion of niobium (Nb) is much larger in Inconel 718 compared to the others. This element forms the strengthening phases which give the excellent strength to this type of Inconel [51]. In718 contains a relatively high proportion of chromium (Cr), which gives it a high resistance to corrosion and oxidation. Depending on the desired application, the proportion of this element can change; for instance, In601 and In693 have a higher percentage of Cr and are therefore more suitable for applications in very corrosive environments [44]. The presence of Mo also provides better properties regarding pitting corrosion [32].

In	**Ni%**	**Cr%**	**Nb%**	**Mo%**	**Co%**	**Fe%**	**Ti%**	**Al%**	**Mn%**	**Si%**	**C%**
601	60.5	23	-	-	0.05	18	-	1.35	1	0.5	1
625	58	21.5	-	9	1	5	0.4	0.4	0.5	0.5	-
693	53	29	1.5	-	-	4.25	1	3.25 1	0.5	0.5	0.5
718	**50–55**	**17–21**	**4.75–5.5**	**3.05**	**1**	**Bal**	**1.15**	**0.5**	**0.35**	**0.35**	**0.3**
783	28	3	3	-	-	25.5	-	5.5	0.5	0.5	0.5

Table 1.1: Chemical composition in weight percentage of the principal elements of different type of Inconel. [30] [56]

1.1.2 Inconel 718

In718 was developed in the 1950s to optimise the strength of Ni-based superalloys already existing [51]. As explained above, the constituents and their proportions cause the mechanical properties of the material to vary, it is due to the formation of different phases. These phases confer different properties to the material with the adequate microstructure, which depend on the manufacturing process used.

In Inconel 718, in addition to the main nickel matrix called the γ phase, some oxides can be present in the matrix. With the presence of Al and Cr, some precipitates such as Al_2O_3 and Cr_2O_3 are formed. In small quantities, they are responsible for the good corrosion and oxidation resistance. There are also Co, Cr, Mo and W dissolved in the matrix, which can also involve lattice distortion [24] [14].

The γ' phase can be found, composed of Ni_3(Al,Ti) with a cubic crystal structure, where Ni atoms are located at the centre of the faces and Al or Ti atoms at the corners of the cubic structure as shown in Fig.1.1. This phase helps to harden the material; it can be formed between 500 and 565°C [33].

The second important phase formed is γ'' composed of Ni_3Nb with a body-centred tetragonal (BCT) structure shown in Fig.1.1. It is therefore the main hardening phase and begins to form around 700°C [33]. For these reasons, post-processes such as age hardening are performed around 720°C and 620°C [47]; most of the time, it is performed in two steps and

is then called double ageing (DA) [6]. The structures of these three principal phases are represented in Figure 1.1. These phases block dislocations and a larger amount of energy is needed for their propagation through the grains [51] [44]. At elevated temperatures, γ'' can precipitate to form the δ phase, the typical service temperature is therefore limited between 650 and 700°C [24].

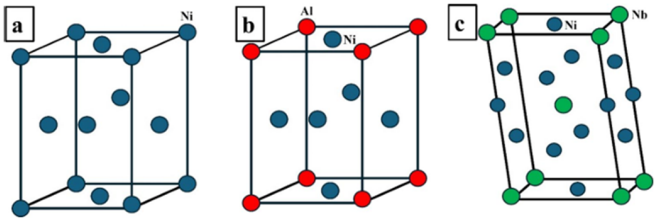

Figure 1.1: Crystal structure of the principal phases in Inconel 718. a):FCC, b): cubic ($L1_2$), c)BCT. [44]

The δ phase composed of Ni_3Nb, which has the same chemical formula as γ'', but it has an orthorhombic structure which confers very different properties. This phase can be useful in small quantities because it limits the grain size, but it uses Nb, which is preferable to be used for the hardening phase γ''. The δ phase can be stable up to 1050°C [33]. The different thermal treatments must be well controlled to dissolve this phase correctly and not to form too much during the ageing step.

The Laves phase, composed of $(Ni,Fe,Cr)_2(Nb,Mo,Ti)$ with a hexagonal structure [31], is formed during solidification and is therefore difficult to avoid, but it is very brittle and therefore initiates crack propagation [45]. This phase is stable up to 1050°C; heat treatments such as homogenisation (above 1050°C) and solution treatment (around 980°C) can be used to dissolve these undesirable phases in the matrix [49] and obtain a single-phase supersaturated solid solution (SSSS), followed by a quench to prevent the formation of the other phases such as δ phase.

Carbon can combine with segregated elements and form metallic carbides (MC) composed of (Nb,Ti)C [31]. These metallic compounds are also formed during solidification at the grain boundaries [14] where the segregated elements are pushed during crystal structure formation. With a cubic structure, they can be stable up to 1200°C and are therefore very difficult to dissolve by heat treatment; they rather transform into finer compounds such as $M_{23}C_6$ and M_6C. These carbides retard creep by blocking the movement of dislocations at grain boundaries. Also, by distributing the stress over the grain boundaries, thus avoiding stress concentrations [51], and limit grain growth by pinning effect. Like the δ phase, they are composed of Nb and, for the same reason explained above, this phase is unwanted in large quantities; this is why only a small amount of C is introduced, less than 0.3%. MC are also very hard and brittle and therefore affect the resistance of the material. The next table 1.2 summarises the different phases and their characteristics.

Phases	Chemical formula	Crystal structure	Role / Effect
γ	Ni	FCC	Principle matrix: very stable
γ'	Ni_3(Al,Ti)	Cubic ($L1_2$)	Hardening
γ''	Ni_3Nb	BCT	Hardening
δ	Ni_3Nb	Orthorhombic	Limits grain size but uses Nb
Laves phase	$(Ni,Fe,Cr)_2(Nb,Mo,Ti)$	Hexagonal	not wanted: very brittle
MC	(Nb,Ti)C	Cubic	Retards creep but uses Nb

Table 1.2: Chemical formulas, crystal structures and roles and effects of the phases present in Inconel 718. [44] [31]

1.2 Conventional manufacturing methods for In718

There are many feasible methods, each with its advantages and drawbacks, to manufacture Inconel with acceptable properties. The conventional methods (CM) are casting and machining, such as milling and turning; welding is also possible because Inconel 718 presents a low risk of oxidation and hot cracking. There is also wrought Inconel, which in most cases shows better mechanical properties than cast Inconel in particular when it is followed by adequate heat treatment, but it is also more expensive. Casting allows complex shapes to be obtained, but many defects can occur and undesirable phases can form; this alters the density and the mechanical properties. Casting is therefore usually followed by heat treatment [60]. Machining is very difficult because of the strength of Inconel, so these methods require specific tools and cooling control [30]; however, due to these properties, it can conversely be used as a tool to machine other materials [30].

CM most of the time give a homogeneous microstructure composed of equiaxed grains, which confers isotropic behaviour to the material [2]. However, with casting significant thermal gradients can occur at certain locations in the part, leading to the formation of columnar grains which locally lead to anisotropic behaviour.

Many phases may have precipitated in the matrix at the end of the process, but not necessarily in sufficient quantities such as γ' and γ'', or they may be unwanted phases like the δ phase and Laves phase. Therefore, these methods are often followed by heat treatments to obtain the desired phases and enhance the mechanical properties. These may be the processes mentioned in the previous section, namely homogenisation plus solution treatment and ageing (HSTA), or hot isostatic pressing (HIP), used to reduce porosity and anisotropy by promoting recrystallisation in order to form a more homogeneous structure [28].

1.3 Additive manufacturing methods

Initially developed for polymer materials, additive manufacturing (AM) also called 3D printing has been extended to other materials with the emergence of new innovative tech-

niques. Despite the difference between the technology involved, for each technique the principle is the same: the parts are manufactured by adding material, layer by layer. Among the seven groups of AM techniques listed by ASTM 52910 : vat photopolymerisation, material extrusion, material jetting, binder jetting, powder bed fusion (PBF), directed energy deposition (DED) and sheet lamination [73], four are suitable for metals:

- DED composed of Laser Engineering Net Shape (LENS), Electron Beam Freeform Fabrication (EBF3) and Wire Arc Additive Manufacturing (WAAM)
- Binder Jetting (BJ)
- Material jetting with nanoparticle jetting techniques (NPJ)
- PBF composed of Laser Powder Bed Fusion (LPBF), also called Selective Laser Melting (SLM), and Electron Beam Melting (EBM) [51] [24] [19].

Like all additive methods, they allow to reduce the production time from the design phase to the final piece and therefore, it is useful when only a small number of part is needed [48] [59]. It only requires an STL file made by triangulation based on the CAD model. This means that the file converts all the surfaces (outer and inner) into triangles. Then the model from the STL file is sliced, it consists of decomposing the model in several 2D layers by a printer's software [76]. The other parameters are set and then the information is converted into a clt file or an ilt file which can also contain parameters relative to the laser. The clt file can be interpreted by the printing machine and contains all the information needed for the printing, the laser parameters can be set directly on the machine when using a clt file. All these steps are quite fast when the behaviour of the material is well known, allowing the printing parameters to be correctly adjusted depending on the shape and the quality expectations of the final part.

The main advantage is obviously the complex geometries that are feasible with AM and impossible to manufacture using CM [59], as well as the reduction of post-machining treatments [18], which can be difficult for very strong alloys such as Inconel, as explained in the previous section 1.2. AM also allows the reduction of assembly steps by manufacturing a single piece that would otherwise be made of several parts using CM. They are particularly interesting for applications requiring complex internal channels, as can be the case for cooling devices, for instance [51]. So using AM techniques allows to expand the fields of possibility in terms of design and therefore also improve the technical capabilities of certain systems. This is directly linked to another field highly studied in engineering called topology optimisation. This technique allows to design pieces with enhanced mechanical properties while saving material. Topology optimisation leads to complex design with organic shapes that can usually not be manufactured with CM. AM is the way to make the part designed feasible thanks to this technique. So, AM and topology optimisation are two complementary methods for designing and manufacturing part with low material waste and enhanced mechanical properties.

1.3.1 AM of Inconel

Inconel being a weldable alloy, it is suitable for many AM techniques [9] which basically relies on similar processes. The AM techniques possible for Inconel are BJ, DED, and PBF; the latter two are the most widely used and the most studied [60] due to their flexibility and robustness.

DED consists of depositing the material (powder or wire) at a specific location while simultaneously heating it. Several sources of energy are available: laser, electron beam and electric arc. This method can also be used not for manufacturing but for remanufacturing, if a part presents damage at its surface.

The difference compared with PBF methods is that, with EBM and LPBF, the powder is stored in a tank and at each layer the build platform moves down of a distance of a layer thickness and the powder platform moves up. Then the powder is spread by a recoater from the storage area to the build area to form a complete layer. Then the energy source (laser or electron beam) melts the powder at the right locations [51] as illustrated in Fig.1.2, the layer is melted sufficiently to stick with the previous layer. At the end, the excess powder can be reused.

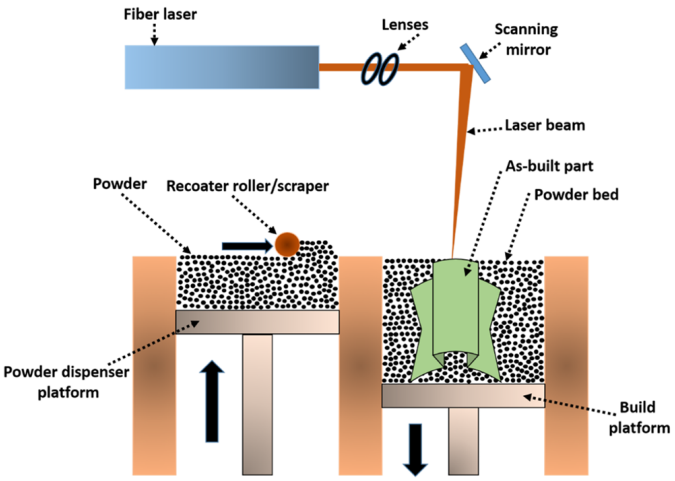

Figure 1.2: Scheme of LPBF system. [51]

The main difference between LPBF and EBM, except for the power source, is the power ranges; while LPBF rarely exceeds 1000 W, EBM can reach 60 kW. Then many parameters change, such as the powder particles, which vary from 10 to 60 μm with LPBF and from 60 to 105 μm for EBM. The layer thickness can also be two times bigger with EBM, and the scan speeds are much larger too. The spot size of the beam is smaller with a laser beam, so LPBF allows more precise details, but the process takes more time. The environment in the build volume is also different: LPBF uses a flow of inert gas such as argon (Ar) or nitrogen (N) and extracts the air to protect the metal from oxidation, and EBM simply

uses a vacuum chamber.

The two methods have their advantages and drawbacks, which can enhance or alter the strength and hardness of the material. EBM uses a powder bed preheated at high temperature to get a pre-sintered powder which forms what is called a cake, this reduces thermal gradients and prevents residual stresses and cracks, which are frequent issues encountered with LPBF. The cake can be difficult to remove depending on the part geometry but no support is needed, unlike LPBF which requires support to prevent excessively large thermal gradients. However, LPBF makes finer grains than EBM, which give a harder material [60] [51]. Both PBF techniques offer low material waste because unmelted powder can be reused, best practice recommends using only one third reused powder. Despite the precise dimensions that can be obtained with LPBF, they can present a poor surface finish [57].

The scan speed with DED is lower than with PBF, but the spot size is much larger; therefore, DED is less precise but still faster and is more suitable for large-scale parts [24]. The size of the powder particles used for DED is comparable to those used for EBM due to the larger power supplied with these two methods [51] [24]. The geometries that can be made are also different, with PBF the powder must be removed, therefore no closed volume can be designed which is not the case with DED.

1.3.2 LPBF technique

LPBF method requires a huge number of parameters to set. Each parameter can have a large influence on the properties of the material; that is why each of them has to be analysed which makes the experiment difficult to carry out given the time required to compare variations in a parameter. The principal parameters are [57] [4]:

- the laser power, which corresponds to the power delivered by the laser to the powder,
- the scanning speed simply corresponds to the speed at which the laser sweeps the powder,
- the laser scan direction or scan strategy is the direction of the laser track that can change at each layer,
- the laser focus diameter corresponds to the diameter of the laser spot on the powder surface,
- the hatch distance is the distance between the middle of two adjacent tracks as shown in Fig.1.3,
- the layer thickness is the thickness of the layer of powder that is spread over the entire build area,
- the base plate temperature is the temperature at which the build platform is preheated before and during the process.

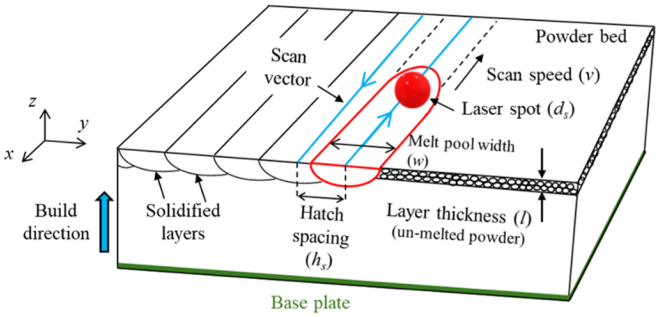

Figure 1.3: Scheme of melt pools and laser track on a powder bed. [1]

The parameters relative to the printing machine are mostly studied, but the properties of the powder are also essential in methods such as LPBF because the powder has to be correctly spread to form a smooth and homogeneous layer [41]. The main characteristics to account for are:

- the chemical composition of the powder because some contamination can occur sometimes due to poor storage conditions,
- the thermo-mechanical properties of the material such as C_p,
- the porosity of the powder, which can lead to porosity in the final parts,
- the rheology of the powder, that refers to the flowability and the packing behaviour, which depend on the size distribution and the morphology of the particles which must be spherical.

These parameters and the layer thickness (also linked to the powder) can have an impact on the surface finish and, to a lesser extent, on the density [41] [57].

1.3.2.1 Impact of parameters on porosity/density

Several types of phenomena can occur in the material obtained from LPBF during the solidification and the melting of the powder. There are three main phenomena that lead to defects like porosity inside the final part, there are called [27]:

- Lack of fusion
- Keyhole
- Balling

Usually, only two parameters are investigated to optimise the density of the material and avoid porosity [4]. The laser scanning speed and the laser power are considered, and they need to be adjusted to find an optimal configuration called conduction mode [27] and avoid the defects listed above. The base plate temperature can vary a lot depending on

the purpose of the research but the other parameters are kept constant and typical values for Inconel are around [57]:

- 0.12 for the hatch distance,
- 0.03 mm for the layer thickness,
- 0.085 mm for the laser focus diameter,
- the scanning strategy can be investigated, but the classical angle is 90°.

Then power–velocity (PV) processing maps can be obtained, as can be seen at the top left in Fig1.4. Several zones can be identified corresponding to the different types of defects. Each defect leads to porosity in the material, but the shape, the size, and the distribution are not the same. The optimal zone is between these areas, consequently, it can be difficult to find the right window.

A lack of fusion appears when there is not enough energy provided to the powder; it is the case when the scanning speed is too high and the laser power is low. It can be due to too large a hatch spacing or too thick a powder layer, but most of the time it is the scan speed and the laser power that are adjusted while keeping the hatch spacing and layer thickness constant. When the energy is not sufficient, it involves too little overlapping between adjacent tracks of the laser and leads to unmelted powder at certain locations [4] as can be seen in Fig.1.4 b) and d). It can have an impact on the spreading of the next layer and then involves more defects.

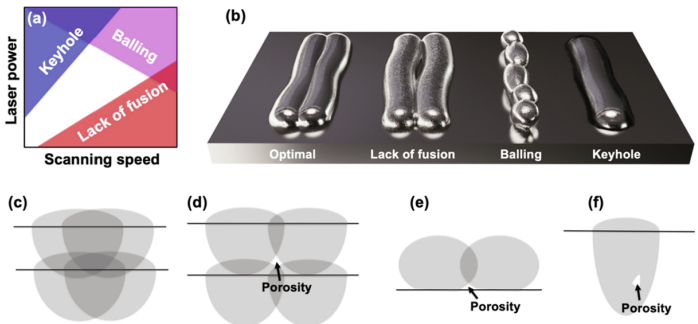

Figure 1.4: a) Theoretical PV processing map with different defect areas. b) Melt pool shape for each mode. Scheme of melt pool sections c) optimal mode, d) lack of fusion, e) balling, f) keyhole. [4]

Conversely, the keyhole mode is due to too large an amount of energy transmitted to the powder, which appears when the scanning speed is low and the laser power is high. The laser melts not only the powder layer but also the previous layer already solidified. Then the melt pool becomes very deep as can be seen in Fig.1.4 f). So, it consumes too much energy, but the main problem is the recoil pressure, which leads to evaporation of gas that can be trapped in the material. The keyhole mode can sometimes be identified as the

regime leading to spherical pores that are easily identifiable and which contrast to the lack of fusion leading to very irregular pore shapes [4] as shown in Fig.1.5. In fact, the keyhole mode appears more precisely when the gas bubbles pile up around shrinkage porosity and form a porosity with a keyhole shape giving the mode its name.

Balling is the most complex effect and occurs when the laser scan speed and the laser power are both large. The melt pool, still liquid, becomes too long, and fluid dynamics effects such as the Marangoni effect (related to the surface tension of the melt pool) appear and lead to the formation of droplets as illustrated in Fig.1.4b). This kind of defect is very problematic because after solidification, the layer is not smooth and the next layer of powder spread over it, will not be smooth either. It can lead to lack of fusion and keyhole defects due to the varying thickness; this effect can be seen in the PV processing map, where there is some superposition between the balling zone and the other ones [4].

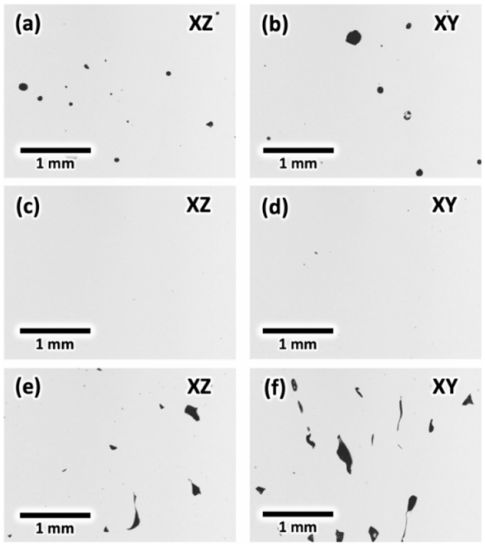

Figure 1.5: Optical micrographs with different PV values, a,b) Gas porosity, c,d) Optimal mode, e,f) Lack of fusion. [27]

1.3.2.2 Preheated base plate

With LPBF, the build platform can be heated to avoid large thermal gradients inside the part and then prevent internal stresses and reduce crack density, which is one of the most frequent issues encountered with such a method. This technique requires careful control because some properties can be altered. The behaviour of the material is not necessarily monotonic when increasing the temperature, also here the right operating window must be found. The preheating can enhance, in the matrix, the formation of Al-rich oxides and increases the size of Si-rich phases already present at low preheat temperature. So, the higher temperature makes the reactions leading to these oxides easier, and they are initiation sites for cracks. Therefore, it has the opposite effect to what was intended, i.e.

the reduction of cracks. So, the preheating temperature is useful to reduce internal defects, but the air vacuum must be very high and the powder must be of high quality to avoid oxygen contamination [60].

Also, the preheating temperature seems to allow a larger range of laser power with the same scan speed to obtain near fully dense parts. The number of pores decreases with the increase in preheating temperature, but the pore size increases [60].

However, when too high a preheating temperature is applied, the size of the melt pool increases and the risk of switching to keyhole mode increases. The overlap between adjacent melt pools increase too and the remelting leads to a different microstructure than expected [11]. So, the energy delivered to the powder must be reduced.

1.3.2.3 Energy measurement

It is necessary to quantify the energy delivered to the powder based on the laser power and the scanning speed which are the two laser parameters that can vary. There are different ways to measure this amount of energy [4]:

- The linear energy density (LED)
- The areal energy density (AED)
- The volumetric energy density (VED)
- The specific energy density (SED)

The LED considers the laser spot as a point and gives the energy distributed over a line and then is expressed in Joule per unit of length. The AED is similar to the LED but does not assume the laser spot as a single point and takes the spot radius, or sometimes the spot diameter, in its expression and is expressed in Joule per unit area. The SED and the VED both give the energy over a volume, but the SED considers the true volume of the melt pool, which requires a specific analysis to obtain w and d. The VED considers the "theoretical" dimensions of the melt pool; it only takes into account the parameters of the machine and does not depend on the final results. So, it is possible to compute it directly even before the printing process [4].

There are obtained using the following formulas:

$$LED = \frac{P}{V} \text{ [J/m]} \tag{1.1}$$

$$AED = \frac{P}{V \cdot r_l} \text{ [J/mm}^2\text{]} \tag{1.2}$$

$$VED = \frac{P}{V \cdot H \cdot L} \text{ [J/mm}^3\text{]} \tag{1.3}$$

$$SED = \frac{P}{V \cdot w \cdot d} \ [\text{J/mm}^3] \tag{1.4}$$

With P the laser power, V the scanning speed, r_l the laser spot size, H the hatch spacing, L the layer thickness, and w and d respectively the melt pool width and depth. Like the VED, the AED and LED depend only on parameters set before printing.

The most commonly used is the VED because it is more useful to work with energy per unit volume and it is much easier to compute compared to the SED as explained above. In practice, the VED is not used to determine the mode of porosity but rather for melt pool characterisation. Indeed, the same VED values with different scanning speeds and laser powers can lead to different types of porosity listed in the previous section.

However, VED must be corrected to take into account the pre-heating temperature. In fact, when the build platform is preheated to prevent large temperature gradients, some energy is already supplied to the powder by preheating and this has to be considered when computing the VED. So equation 1.5 is proposed in [60]; it suggests multiplying the classical VED by the ratio of the energy required to reach the melting point without pre-heating to the energy required with pre-heating:

$$VED^* = VED \cdot \frac{E_{melt}(T_0)}{E_{melt}(T)} \tag{1.5}$$

with $T_0 = 25°C$ and T is the preheating temperature and E_{melt} is given with the formula:

$$E_{melt}(T) = \rho c_p (T_m - T) \tag{1.6}$$

Where $T_m = 1350°$ which correspond to the melting temperature of the In718 [60]

This formula provides a simple and intuitive way to correct the VED when the build platform is preheated. Another, less simplified formula is proposed in equation 1.7; it consists of the ratio between the classical VED and the energy required to melt the powder with pre-heating:

$$\eta_E = \frac{VED}{E_{fusion}} \tag{1.7}$$

with

$$E_{fusion} = \rho[c_p(T_m - T_{preheat}) + L_f] \tag{1.8}$$

where the latent heat of fusion L_f is considered.

1.3.2.4 Scan direction

The scanning strategy can also have an impact on the properties of the material. Indeed, it is possible to rotate the direction of the scan at the same angle at each layer, as can be seen in Fig1.6. After optimizing the scan speed, the laser power and the preheating temperature, the scanning strategy helps to reduce the different defects encountered with the LPBF technique, such as porosity and residual stresses [36].

Several rotation angles are possible, the most common being: $45°, 90°, 105°$ as exposed in Fig.1.6a, but the best identified is $67°$ due to the low repetition of orientation between layers [75] [67]. With a $0°$ rotation angle, edge effects can be important and lead to an irregular surface, which enhances porosity defects due to poorly dispersed powder on the next layers. There is also what is called an island scan, as seen in Fig. 1.6b which consists of dividing a layer into several zones with different scan orientation and changing the orientation at each layer. This technique is less used because it is more complex and does not necessarily give better results. On the contrary, the border zone between the islands is exposed to a different overlap than the rest of the layer and therefore presents more defects which affect the mechanical properties [36].

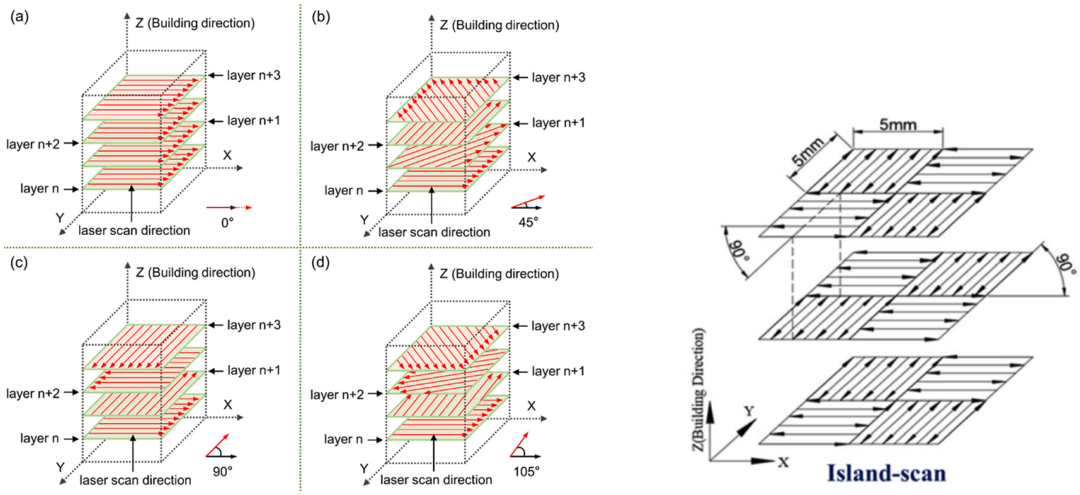

(a) (b)

Figure 1.6: Scheme of scanning strategies: a) with different rotation angles betwen layers [75], b) island scan with a90° rotation angle. [36]

The scanning strategy can also affect the grain morphology, but it remains mainly columnar grains. The epitaxial growth is not really affected even if the grains can sometimes undulate in the build direction to grow from one melt pool to another. However, the primary dendrite arm spacing (PDAS) can be affected which impacts the mechanical properties of the material. The impact on the density of the material seems to be more significant when using a high laser power [75]. It can also reduce residual stresses, which are promoted by

the high cooling rates encountered in the LPBF method. Residual stresses are due to the fact that when a layer solidifies, it wants to contract but it is prevented by the previous layer, which has already solidified. In addition, the frequent passage of the laser involves thermal cycles, which increase residual stress formation and dislocation density. By changing the scanning strategy, the thermal cycles are reduced and then it decreases residual stresses. The scanning strategy can also have an impact on the mechanical properties, by increasing the rotation angle, the yield strength (YS), the ultimate tensile strength (UTS), and the elongation (EL) seem to increase too [75] when keeping the other parameters constant.

1.3.3 Microstructure in AM

As is often the case with AM techniques, columnar grains are observed due to the epitaxial solidification through the layers. Meaning that the grains formed at a certain layer continue to grow in the next layer; there is not necessarily the formation of new grains at each layer. It forms elongated grains in the build direction; the growth occurs in the opposite direction to the heat flux, which corresponds to the direction of the thermal gradient. This phenomenon requires quite high energy because it needs to remelt the previous layer to continue the grain growth and to ensure the bonding between the adjacent layers . So, this elongated shape can be mitigated by delivering less energy while paying attention to the possible defects such as lack of fusion introduced in the previous section 1.3.2.1 [57] [26]. It was seen that a lower VED seems to provide near isotropic behaviour by mitigating the epitaxial growth and enhancing equiaxed grains [52] [57].

The grain size also tends to be proportional to the energy delivered by the laser to the powder [45]. It is explained by the change in the melt pool geometry. When the amount of energy provided increases (higher VED), the melt pool depth and width increase too, then the cooling rate decreases and the grains have more time to grow; it leads to a larger grain size. So the micro-structure can thus change from one mode of solidification to another. In conduction mode, several grain morphologies can occur in a single MP.

With AM techniques, very fast cooling rates of the order of 10^6 or 10^7 Ks^{-1} and several thermal cycles are encountered. This leads to a different structure from the CM methods, characterised by the fine sub-grain structures [30]. The type of microstructure is determined by the solidification mode which depends on two parameters: the solidification rate R and the Temperature gradient G. As illustrated in Fig.1.7, different types of solidification can occur as a function of the ratio $\frac{G}{R}$ and the product $G \cdot R$ also gives the size of the microstructure obtained; the larger the product, the finer the structure. The VED, R and G are directly linked because they depend on the laser speed and power. R and G are respectively inversely proportional and proportional to the power and the opposite relationship is observed with the scan speed [21].

AM techniques such as LPBF most of the time lead to cellular dendrite or columnar dendritic structures [52] [57] even if low VED can lead to equiaxed dendritic structures [21].

Typically, columnar cells are found at the centre and equiaxed cells at the boundaries [45]. At the MP boundary, the solidification rate is too rapid to allow columnar solidification.

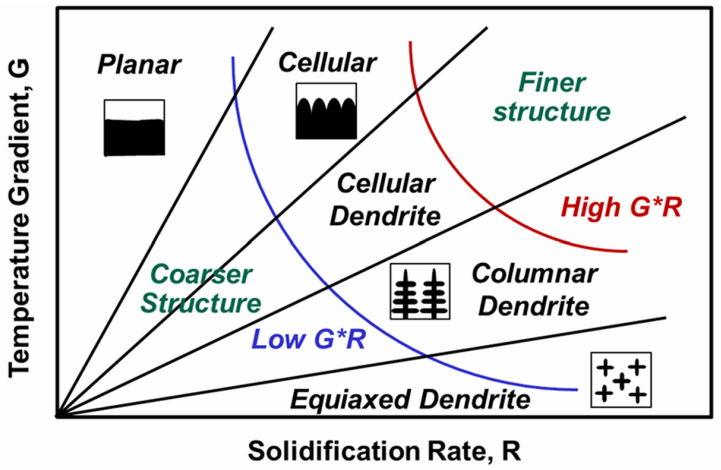

Figure 1.7: Microstructure formation modes as a function of temperature gradient and solidification rate [34].

In fact, small variations in processing parameters can lead to very different microstructures in terms of size, shape and orientation. Therefore, it is not really possible to define a single type of microstructure in AM but a trend can be found as a function of VED. With high VED, crystallographic lamellar microstructures (CLM) can be found, it presents elongated structures and oriented in the build direction as seen in Fig.1.8a). With medium VED, single-crystal-like microstructures (SCM) are observable in 1.8b) which consists of structures oriented perpendicularly to the melt pool boundary. With low VED, polycrystalline-like microstructures (PCM), shown in Fig1.8c), is obtained with elongated structures but now with a more random orientation [21]. This explains the decrease in anisotropic behaviour with a decrease in VED. The anisotropy is mainly due to the grains texture, which corresponds to the crystal orientation, and it is enhanced by the columnar grain morphology [21] [51].

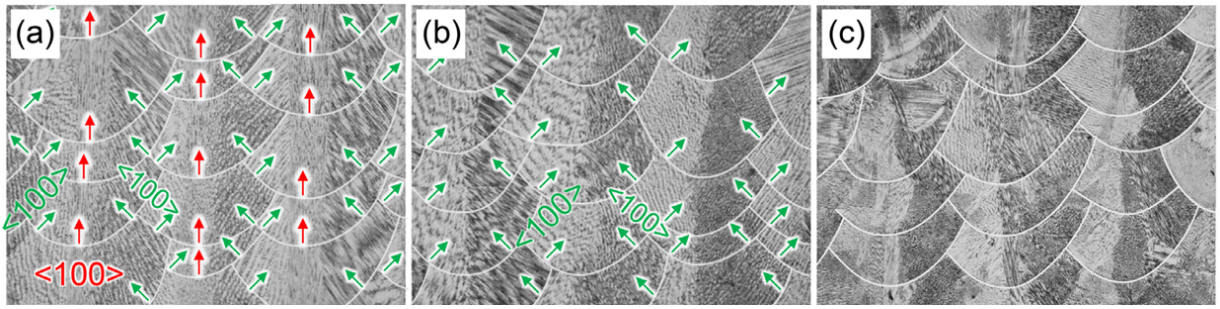

Figure 1.8: SEM images of melt pools with a) CLM, b) SCM, c) PCM. [21]

The type of microstructure has an impact on the mechanical properties of the material. The high VED leads to lower cooling rates giving coarser structures which decreases the hardness. With low VED, the inverse phenomenon is observable and the hardness increases, but with too low VED the cooling rate is too fast and residual stresses appear [70]. The grain size also has an impact on the creep behaviour. If the grains are larger, dislocations take longer to reach and accumulate at the grain boundaries. So, with AM techniques, the as-built material is weaker in creep due to the very fast cooling and the smaller structures involved. The structures that can be found in wrought alloys are very different, the grains are mainly equiaxed, the phase dispersion is more homogeneous and there is less segregation. Fewer residual stresses are found when the cooling is well controlled.

Many studies show the application of heat treatments initially developed for CM to the pieces obtained by AM. In fact, the microstructure obtained by AM in the as-built pieces is totally different from the one obtained from CM, and the heat treatments are no longer suitable. The conventional heat treatments do not allow complete recrystallisation with such structures. In addition, the only phase present is the matrix γ because the other phases do not have enough time to precipitate due to the very high cooling rates encountered in AM. Some segregation of Ti, Mo and Nb can be found near the grain boundaries because these elements do not dissolve in the γ matrix and are then pushed to the crystal structure boundary when it forms during solidification [14]. Segregated elements are not stable, and can in some cases, form Laves phases that alter the strength of the material [23] [30].

An alternative to post-treatment is in-situ ageing. With a high preheating temperature, it is possible to form strengthening phases during the printing process and then reduce the formation of Laves phases. It consists of preheating the build platform to keep the powder and the layers already solidified at a certain temperature. This technique remains challenging because it requires equipment adapted to reach preheating temperatures above 600°C to form the strengthening phases γ' and γ''. Moreover, it can reinforce oxidation if the vacuum in the build volume is not sufficiently low [60]. The real temperature in the part is difficult to know, there is always a thermal gradient and the temperature of the argon flow is not adjustable.

1.4 Mechanical properties

The mechanical properties depend on the different phases precipitated and also on the microstructure. A slight variation in the VED can lead to a significant difference in the YS, UTS and El values, which highlights the importance of finding the optimal processing window. The properties of the as-built parts obtained by LPBF and the parts obtained by CM are very different. The properties such as YS and UTS obtained with casting are most of the time also obtained with as-built parts and are even lower in some cases [33].

Cast parts have a YS of around 750 MPa and a UTS around 850 MPa [70]. The UTS of as-built parts exceeds this value and varies between 1000 and 1100 MPa [51]. The typical

values of wrought Inconel are much higher, around 1050 MPa for the YS and 1300 MPa for the UTS. The properties of wrought Inconel can be improved by heat treatment to reach a YS of 1400 MPa and a UTS of 1600 MPa. These values cannot be reached with LPBF as-built parts; after an adequate heat treatment, it is possible to achieve strengths between those of wrought and heat-treated wrought Inconel. So it is not possible for now to obtain with AM the best properties that can be reached with CM. In addition, the parts obtained with AM present anisotropic mechanical properties, the comparisons here are made considering the preferential direction of the AM parts. As explained before, AM provides a finer and oriented microstructure, which confers greater elongation to the material. The parts obtained with LPBF can show elongations between 30 and 35%, while cast and wrought Inconel present elongations of 5% and 10%, respectively [33].

The hardness of the material is very dependent on the printing parameters, and the behaviour of the hardness also depends on the scale at which it is studied. The variation in the preheating temperature shows a minimum in the micro-hardness. Firstly, the hardness decreases when the temperature increases, it can be due to the decrease in dislocation density, which decreases the hardness. Then the hardness increases with temperature that can be due to in-situ hardening, when the temperature is sufficiently high to form the hardening phases. Then two opposite effects occur: the γ'' formation and the coarsening of the microstructure, which decreases the hardness. At the macro scale, the hardness decreases and seems to stabilise after a certain temperature. This is also explained by the softening due to the reduction in residual stresses and also by structure coarsening [60].

1.5 Mixed powder

To enhance the mechanical properties of the alloy it is possible to mix some additional elements with the conventional powder which will affect the microstructure and the behaviour of the material under stress. Two types of particles are used, inoculants and nano oxides which lead to what are called oxide dispersion strengthened (ODS) alloys [69]. The two types of particles impact the material in a very different way, the first plays a significant role during the manufacturing process because it changes the type of microstructure formed, the second does not directly change the microstructure but it allows the formation of elements which affect the properties of the microstructure. These additional constituents account for less than 2 wt.% [43] [22] but can represent a few vol.%. The particle size is also much smaller than that of the initial powder particles. Their size can vary a lot but they are most of the time approximately ten times smaller than the Inconel powder particles [22].

Many types of particles are used as inoculants, the most common are: CeO_2, TiB_2, NbC, LaB6, P, TiCN, TiC. They are mainly used to influence the nucleation of the grains, during solidification [25] [38] [65]. This leads to a finer and more equiaxed structure [42]. The addition of nanoparticles such as Y_2O_3 which can constitute up to 2% of the total weight [71] are used to form oxides in the matrix but they do not directly change the

nucleation mechanism. This leads to the formation of particles which affect the material performance, by Zener pinning it can prevent the growth of the grains and also block dislocations. This phenomenon can also be obtained with inoculants [38]. Ultimately, it improves the yield strength and ultimate tensile strength and the hardness [61] and the creep resistance [66]. The main advantage is that these precipitates are very stable even at high temperature compared to classical strengthening phases such as γ' and γ'' [69]. However, in too large quantities, they can form crack nucleation sites.

Chapter 2

Materials and methods

2.1 LPBF machine

All samples in this study were printed using the LPBF technique and they were manufactured using the Aconity Mini machine, which is made for research purposes rather than industrial production, given its production capacity. The machine is able to preheat the building platform but requires to be cooled down manually at the end of the process, otherwise the preheating temperature remains constant even after the printing process is finished. The Aconity Mini LPBF system, shown in Fig.2.1, has the following characteristics [3]:

- **Build volume:** diameter of 140 mm and heigh of 190 mm reduced to 100 mm if preheating stage is used
- **Powder tank volume:**
- **Laser type:** continuous wave fibre
- **Laser power:** 200 W
- **Max scan speed:** 12 m/s
- **Layer thickness:** down to 10 μm
- **Laser spot size:** 80 μm
- **Gaz pressure:**
  - Argon 4.6 / 6 bar
  - Nitrogen / 6 bar
  - Vacuum / $<$ 2 mbar
- **Inert gas consumption:**

  - $<$ 5 l/min during process
  - $<$ 60 l/min during purging
  - 0 - 5 l/min for vacuum
- **Residual oxygen content:** $<$ 100 ppm
- **Max preheating temperature:** 500°C
- **Platform material:** 316L stainless steel
- **Recoater material:** Carbon fibre
- **Available materials:** Weldable materials
- **Dimensions (W x D X H):** 2450 x 1500 x 2320 mm^3
- **Weight:** 850 kg



Figure 2.1: Aconity mini LPBF system with the build area on the left and control panel on the right. [5]

The volume of the powder tank is much larger than the build volume because best practice recommends having a powder height three times the height of the part. The other process settings can be modified using the Aconity Studio software, which is directly connected to the machine. Most parameters, such as the powder layer and the laser tracks, are set in the CLT file, except for the power and the scan velocity.

2.2 Powder

The powder was also the same for each sample and only virgin powder was used. The chemical composition of the powder, in weight percentage, is listed in the Table2.1:

Ni%	Cr%	Nb%	Mo%	Ti%	Al%	C%	S%	P%
50–55	**17–21**	**4.75–5.5**	**2.8-3.3**	**0.6-1.15**	**0.2-0.8**	**<0.08**	**<0.015**	**0.015**

Table 2.1: Chemical composition in weight percentage of Inconel 718 powder from VDM Metals GmbH [60]

The supplier is VDM Metals GmbH, which provides a gas-atomised In718 powder with a near-spherical shape and particle sizes ranging from 15 to 52 μm, with a size distribution corresponding to: D10 = 23 μm, D50 = 37 μm and D90 = 55 μm.

2.3 Jobs parameters and configurations

2.3.1 Cuboid samples

A first batch of 20 cubes with dimensions of $10 \times 10 \times 10$ mm^3 was produced as sshown in Fig.2.2. Based on the results reported in the paper [60], a preheat temperature of 200°C was used and each cube corresponds to a combination of laser power and scan speed within the ranges [100; 125; 150; 175; 200] W and [700; 800; 900; 1000] mm/s respectively. The other parameters were kept constant and take the following values:

- Scanning strategy: 90°
- Hatch distance: 80 μm
- Layer thickness: 30 μm
- Laser spot size: 80 μm

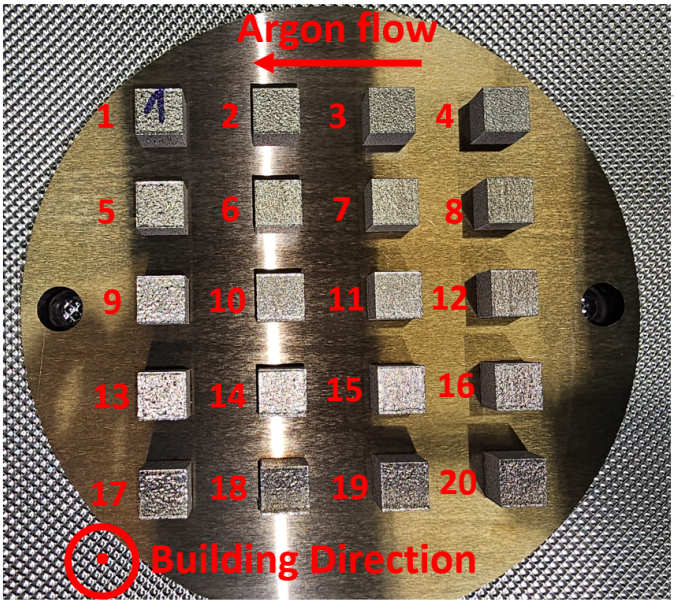

Figure 2.2: Top view of the twenty cubes on the build platform preheated at 200°C and varying scan speed and laser power.

2.3.2 Blocks

After identifying the set of parameters that give the best density for the cubes and taking into account the VED, the most suitable parameters (given in Section 3.1.1.1) have been selected to print four blocks of $40 \times 30 \times 20$ mm^3 as shown in Fig.2.6a. The CAD model was made using Siemens NX 2406 software and then the arrangement of the blocks on the build platform, the slicing and the main printing parameters such as the scanning strategy, the hatch distance and layer thickness were set using Autodesk Netfabb software.

In Fig.2.3, the top right and the bottom left blocks were printed using a scan strategy with a rotation of 90° and the other two were printed using a rotation of 67°. The configuration was chosen to have one block of each scanning strategy on the left and the right on the built platform because the argon flow goes from the right to the left as shown in Fig. 2.3b. It is interesting to have this arrangement to have a fair comparison between the scanning strategies. Indeed, the position on the build platform may have an impact due to the circulation of the argon inside the chamber, so one block of each scanning strategy is placed upstream and one downstream of the argon flow.

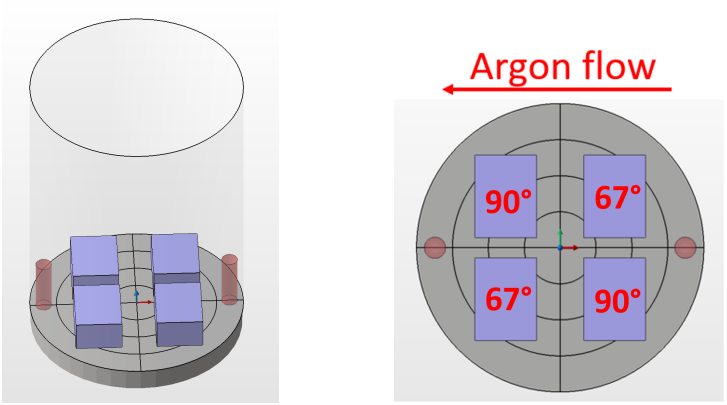

(a) (b)

Figure 2.3: Arrangement of the blocks on the build platform with Autodesk Netfabb software, a) side view and b) top view with scanning strategy rotation angles.

2.4 Profilometer analysis

For each block, a profilometer analysis was conducted using the Alicona Infinite focus G5 profilometer shown in Fig.2.4. This instrument is used to check the surface quality and to obtain the topography of the top surfaces of the blocks using 3D measurements. Its operating principle is based on focus variation, it consists of a measurement of the sharpness variation of the surface under a coaxial white LED light. It provides information about roughness and also provides a colour image which facilitates the analysis. This technique is robust and suitable for measures on complex-shaped surfaces. However, due to its measurement principle it cannot be used with transparent surfaces which is not a problem in this study.

The Alicona Infinite Focus G5 is equipped with lenses of different magnifications: 2.5×, 5×, 10×, 20×, 50×, 100× which enable a minimum vertical resolution of 10 nm. This resolution is not directly related to the vertical scanning distance. The instrument is equipped with a moving base plate in the horizontal direction and a moving lens in the vertical direction and performs the measurements automatically. The profilometer works with the MeasureSuite 5.3.1 software, which enables the user to set all the parameters of the analysis and to define manually the area of interest and the vertical range for the focus variation. Two types of analysis can be conducted: profile roughness measurements along a straight line and a surface roughness measurement over the entire surface.

Only the top surfaces of each block were analysed, but due to the dimensions of these surfaces (40 x 30 mm), too high magnification leads to excessively long measurement times and very large data files. Therefore, the most suitable lens, which provides sufficient image quality with an acceptable dataset is the 5x lens with the characteristics [17]:

- Vertical resolution: 410 nm

- Minimum roughness (Ra): 1.2 μm
- Minimum roughness (Sa): 0.6 μm



Figure 2.4: Alicona - Infinite Focus G5 Profilometer. [64]

2.5 Blocks purposes

Two blocks (one of each scanning strategy) were used to be machined by Electrical Discharge Machining (EDM), to obtain tensile specimens for uniaxial tensile tests. The other two blocks which were located close to the argon outlet can be used to extract samples for thermophysical properties analysis.

2.5.1 Machining equipment

The machine used is the Robofil 310 manufactured by Charmilles Technologies shown in Fig.2.5. This machine has quite a large working volume of 850 x 500 x 400 mm. The Robofil 310 is equipped with five axes which allow it to machine complex shapes. The brass wire has a diameter of 0.25 mm and its speed can be adjusted between 2 and 15 m/min [63].

This machining method is mainly used to machine hard materials with precise dimensions. It consists of passing a conductive wire through the part, and a potential difference is applied between the wire and the machine frame, which is then the same potential as the part being machined. An electrical discharge is formed allowing the material to melt locally without affecting the rest of the part. During the process, a water jet is projected to cool the part.



Figure 2.5: Electrical Discharge Machine Robofil 310 by Charmilles Technologies. [20]

2.5.2 Tensile specimens design and machining approach

Since no standardised specimens design fitted within the blocks, the design shown in Fig.2.6b is based on the dimensions used in [68], but with a smaller gauge and larger gripping section to suit the setup of the tensile tests. The different design iterations tested are shown in Appendix vi. The machining was performed in two steps: first, slices were cut parallel to the build platform and then the specimen geometries were cut out in each slice. The EDM method allows an average surface roughness between 2 and 5 μm. At the end, five tensile specimens were machined per block as illustrated in Fig.2.7.

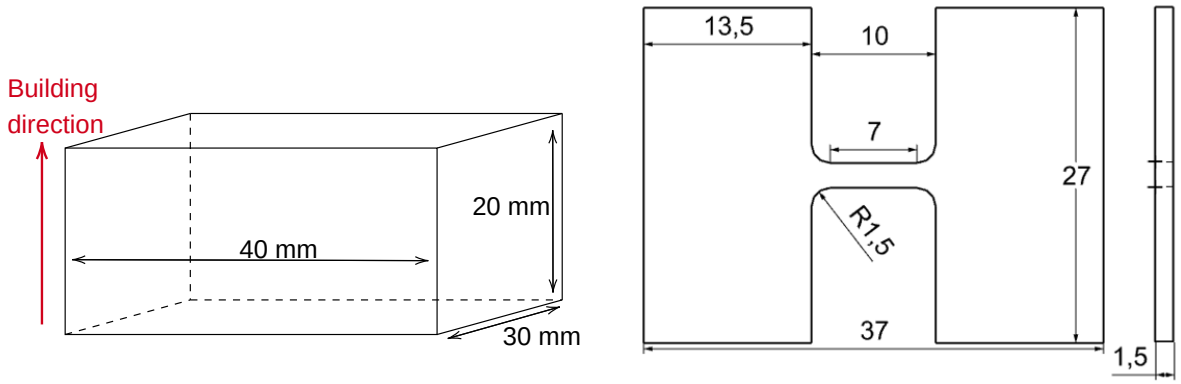

(a) (b)

Figure 2.6: Scheme of a) a block and b) a tensile specimen with dimensions in mm [68]

The five tensile specimens were taken from the middle of the block as illustrated in Fig.2.7a. Several layers at the top were used to test different designs and the bottom of the block is

avoid due to the possibility of higher residual stress levels.

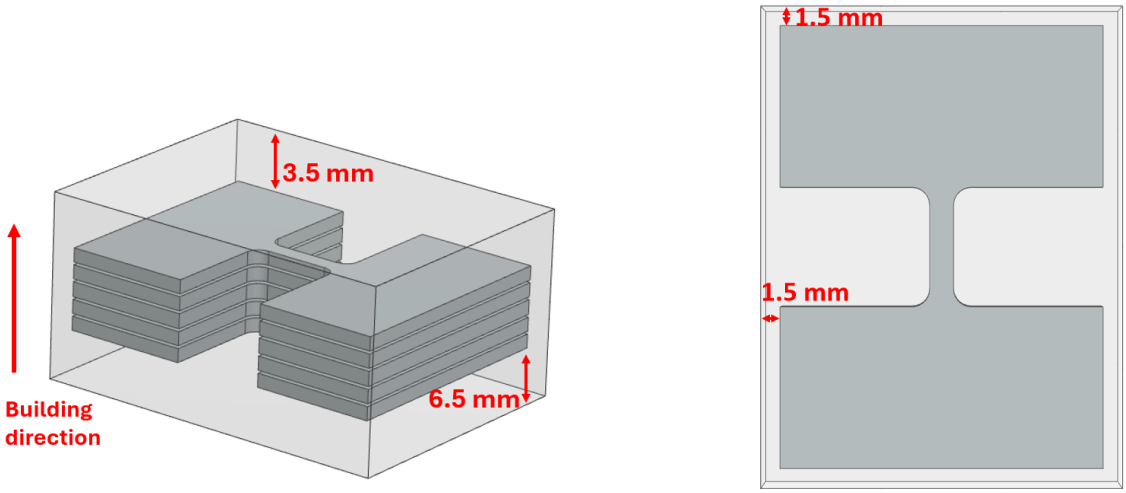

(a) (b)

Figure 2.7: Arrangement of tensile specimens within the block, a) side view and b) top view.

2.5.3 Tensile test approach and equipment

The machine used for the tensile tests is the Schenck Hydropulse. It allows a maximum load of 100 kN and is controlled using the Instron Console 8800 software. The displacement is measured by 2D Digital Image Correlation (DIC) using an AVT Pike f032b firewire camera with a Pentax TVLens (75 mm) and the results are obtained using the VIC Snap 08 software and the post-process was performed using VIC2D 09 software.

Tensile specimens were clamped to their extremities using hydraulic MTS grips applying a pressure of 2 MPa. To ensure quasi-static conditions, a strain rate of $10^{-3}s^{-1}$ is imposed, knowing that the gauge length was 7 mm and using the equation 2.1, the displacement velocity is set to 0.007 mm/s.

$$\frac{V}{L} = R \tag{2.1}$$

where V is the displacement velocity, L is the gauge length, and R is the strain rate

Given that the specimen design did not follow the standard, before analysing the results, the fracture section location needs to be checked to ensure that it is within the gauge rather than near the grip sections. Each part of the tensile specimens was measured using the optical microscope.

2.6 Samples preparation

Before any analysis, the samples needed to be removed from the base plate. No support was printed at their base, the samples were directly in contact with the build platform to obtain optimal heat transfer between the preheated base plate and the cubes. To separate the samples from the build platform, they were simply cut using an Electrical Discharge Machining (EDM) system which consists of cutting the cubes at their bases with a conductive wire as explained in the previous section 2.5.1. The density of the samples was then analysed using a pycnometer (described in more detail in section 2.7.1).

To be examined using the different microscopes, the samples had to be cut, the cross-section was taken parallel to the building direction and perpendicular to the last scan direction to easily identify the melt pool in the top layer. By convention, the section was located at the middle of the sample, as can be seen in Fig.2.8. The samples were cut using a metallographic automatic cutter, the Micracut 202 supplied by Metkon, shown in Fig.2.9.

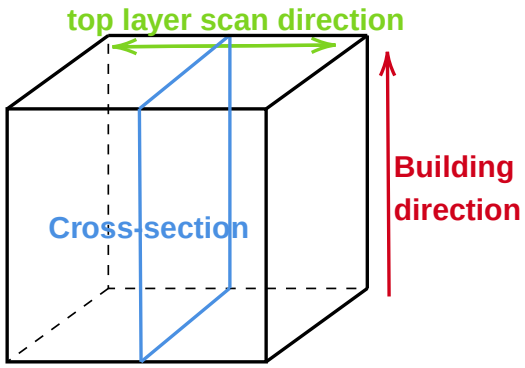

Figure 2.8: Scheme of the location of the cutting section with regard to the building direction and the top layer scan direction on cuboid sample.



Figure 2.9: Metallographic automatic cutter Micracut 202 from Metkon [39].

The cross-section then needed to be polished and the samples had to be previously embed-

ded in Bakelite using the Citopress-1 hot mounting press supplied by Struers as seen in Fig.2.11. The samples were embedded in pairs in a Bakelite cylinder as shown in Fig.2.10. This process consists of covering the samples with Bakelite powder that will be heated to 180°C under 250 bar for 5 minutes followed by 1.5 minutes of cooling. Such conditions ensure that the samples do not heat up to the same extent as the resin.

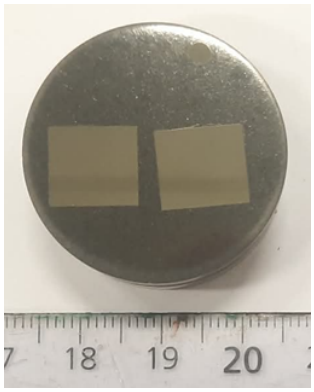

Figure 2.10: Samples embedded in Bakelite cylinder after polishing.



Figure 2.11: Hot mounting press Citopress-1 supplied by Struers. [54]

Then the sample could be polished using the Tegramin-30 polishing machine also supplied by Struers, shown in Fig.2.12. The polishing process consists of several steps.

First, a pre-polishing was conducted with water and abrasive sheets made of silicon carbide of different grain sizes. Beginning with the coarsest one, four grain sizes were used for 1 minute: 120, 220, 500 and 1200 corresponding respectively to 125 μm, 68 μm, 30 μm and 15 μm. Then, specific synthetic polishing cloths were used with a water-based solution containing micro-diamonds and cooling lubricant manually applied to the cloths. This allows to get a mirror-finish surface and to correct the planarity. Firstly, a solution with 9 μm diamond was used followed by a solution with 3 μm and then with 1 μm. The first one used a Dac cloth, while the two others used a Nap cloth also supplied by Struers.

Each polishing step lasted 4 minutes with 2 minutes in each rotation sense. The polishing using the 9 μm diamond solution was conducted for 3 minutes in each sense then the 3 μm diamond solution was used for 2 min in each sense and the 1 μm diamond solution only for 1 minute in each sense. During the polishing process, the Tegramin-30 rotates the samples in one direction and also rotates the abrasive sheets or the cloth in the inverse direction at 140 rpm, and a force of 30 N was applied to each pair of samples.



Figure 2.12: Polishing machine Tegramin-30 supplied by Struers. [55]

A similar process was applied to study the micro- and macro-hardness on the remaining material of each slice in which the tensile specimens were machined as explained in section 2.8.3.

2.7 Density and porosity characterisation

2.7.1 Pycnometer measurement

The densities of the 20 cubes printed at 200°C with varying VED were obtained by measurement with a gas pycnometer, the AccuPyc II 1340 by Micromeritics shown in Fig.2.13. This device uses a non-destructive method and therefore the internal porosities are not considered which can lead to inaccurate results. So, an analysis of the internal porosity is required to have a better estimate of the relative density.



Figure 2.13: Gas pycnometer AccuPyc II 1340 by Micromeritics. [46].

The measurement process consists of 4 steps: first, a certain quantity of inert gas (here helium) is introduced into the cylinder containing the sample. When equilibrium is obtained, the helium can go in a second cylinder. The pressure difference between the two states allows to determine the volume of the sample. By dividing the mass of the sample by the volume, it is possible to obtain its density [40]. For each sample, 5 values were calculated and their average was considered. The relative density can then be obtained by dividing the density of each sample by the reference density of the Inconel 718, following this formula:

$$\text{Relative Density} = \frac{\rho_{sample}}{\rho_{full}} \cdot 100 \tag{2.2}$$

With $\rho_{full} = 8.19$ g/cm^3

2.7.2 Optical microscope

The instrument used was the BX60M microscope seen in Fig.2.14. Supplied by Olympus, it is provided with six magnification lenses: 2.5×, 5×, 10×, 20×, 50×, 100×. Only the 2.5×, 5×, 10×, 20× lenses were used for this analysis, which consisted only of porosity characterisation. In addition, the microscope is equipped with a camera which provides a 20x digital magnification. The light can also be adjusted manually using different Nichols prism polarisers. The image processing was then conducted with the Stream Motion software also developed by Olympus and the Image J software.



Figure 2.14: Microscope BX60M by Olympus [10].

Optical microscope (OM) was used to characterise the porosity inside the samples and to get a second estimation of their densities. The estimation was therefore based only on

the area fraction of voids of a single 2D cross section. Then, the values obtained can be compared with the values from the gas-pycnometer which have to be consistent with each other. It should be noted that the OM density measurements depend on the threshold set to identify the pores on the images, the threshold was the same for each sample but it was fixed according to the appreciation of the user. Two thresholds, similar for each sample, were applied, a high and a low one, an example of thresholds used is given in Appendix ii. This analysis could also help to select the most relevant samples for the SEM analysis and to identify the samples with too much porosity, which were therefore not used for the hardness test, here, the processing parameters were already optimised, so all samples were suitable for the hardness test. The melt pool dimensions, i.e. the depth and the curvature radius were also analysed with the optical microscope. This analysis requires a specific treatment, different from the mirror polish, which is explained in the next section 2.10. Only the samples identified in the optimal processing window and the one with the highest VED will be analysed.

2.8 Macro- and Micro-hardness measurements

2.8.1 Equipment used

The machine uses a Vickers indenter which consists of a pyramidal diamond with an angle of 136° between two opposite faces [13]. The Vickers Hardness (HV) is computed using the formula 2.3:

$$HV = 1.854 \cdot \frac{F}{d^2} \tag{2.3}$$

With F the applied load expressed in Kgf and d expressed in mm, the average of the two diagonals of the square indentation, seen in Fig. 2.15 [15].

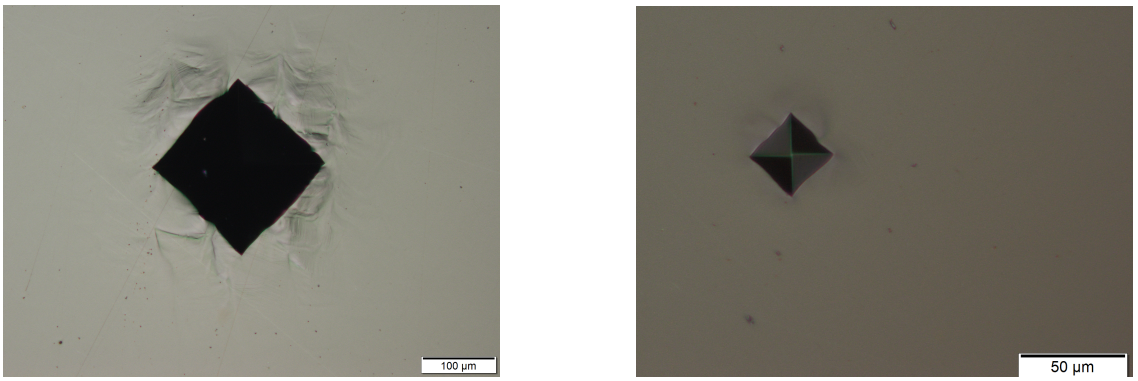

(a) (b)

Figure 2.15: Shape of the top right indentation on sample 19, a) mark after macro hardness test observed with 10× magnification OM, b) mark after micro hardness test observed using 20× magnification OM.

The macro- and micro-hardness tests were performed using the Falcon 500 G2 developed by Innovatest, shown in Fig.2.16. The machine is a stand-alone device with its own built-in computer and software. The indentation process is fully automatic after choosing the number and arrangement of test locations. The machine performs each test using a multi load cell to precisely measure the applied load and adjust it using a closed loop system. This ensures a constant load during the tests. The machine is able to apply a load in the range [0.1 gf ; 62.5 kgf]. This device is equipped with a camera and different magnification lenses are available: 2.5×, 10×, 50×, the camera focus and the measurement of the indentation dimensions are also automated [29].



Figure 2.16: Automatic hardness tester Falcon 500 G2 by Innovatest. [29]

2.8.2 Hardness on cubic samples

The hardness of the samples with an acceptable density was studied. The hardness tests were performed at two different scales, macro- and micro-scale, for each sample tested. This allows to highlight different characteristics of the material with a same method. For the macro-hardness tests, 9 values were taken at 9 different locations disposed as a 3 by 3 grid on the cross section. As can be seen in Fig.2.17b each successive location was at a distance of 3 mm from the other vertically and horizontally. Good practice recommends to separate two test locations by a distance equal to at least three times the diagonal of the indentation. A constant load of 10 kgf (HV10) was used for each test with a dwell time of 10 seconds.

A similar process was used for the micro-hardness. The load was applied to form a 3 by 3 grid, but now with a distance of 0.3 mm between successive points, and the applied load was only 0.3 kgf (HV0.3). This grid was performed at the top right of the macro-hardness test grid as illustrated in Fig.2.17b.

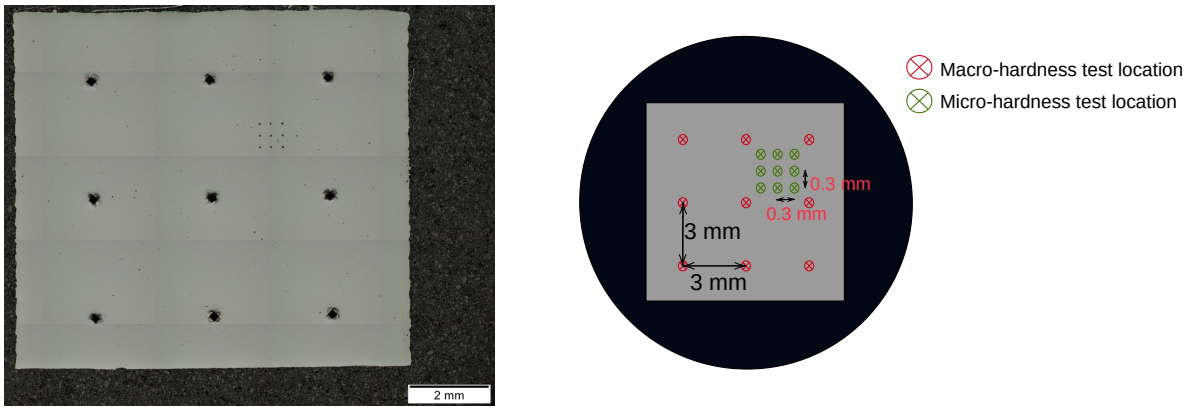

(a) (b)

Figure 2.17: Locations of macro- and micro-hardness indentations on cubic sample cross-section embedded in Bakelite, a) indentation on samples 19 observed using OM at 2.5× magnification, b) scheme of indented sample with the dimensions of the grids.

2.8.3 Hardness on slices from the block

To have an idea of the hardness of the tensile specimens without damaging them before tensile tests and without altering the hardness tests by using the specimens after their failure, it is more suitable to use the remaing material of the slices in which the tensile specimens are machined. Hardness tests are conducted on the surfaces that were in contact with the specimens to obtain the most significant values. As shown in Fig.2.18, a surface along the direction x and the other along y are analysed. To simplify comparisons, each slice will be denoted by the letter "s" followed by a number corresponding to the slice number in the block starting from the top. To distinguish between the two scanning strategies, the slices from the 67° strategy will also include a symbol " ’ " .

To be consistent and allow a fair comparison the exact same parameters as those used for the cubic samples were used here except the shape of the grid which is not possible with the smaller surfaces. As shown in Fig.2.19, only a line of three indentations is applied with the same distance between each indentation as the one used in the grid for macro- and micro-hardness with the cubes. Moreover, the 6 x 7.2 mm sections studied in the blocks, as illustrated in Fig.2.18b are of the same order as the section of 6 x 6 mm studied in the cubes.

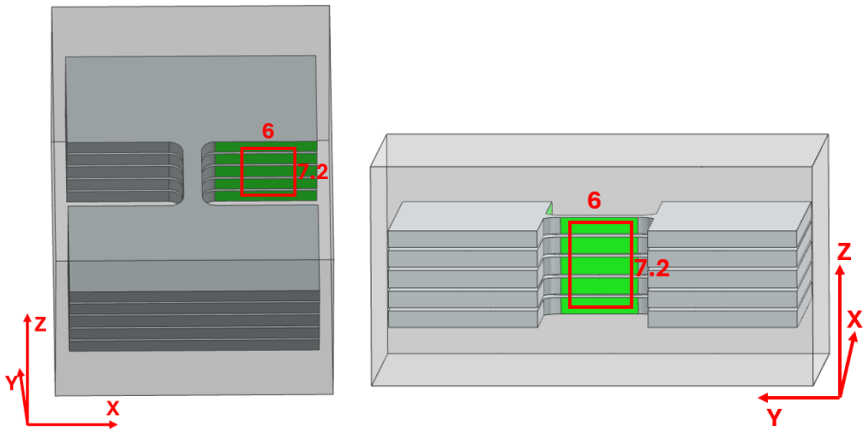

(a) (b)

Figure 2.18: Surfaces highlighted in green on remaining material after machining corresponding the area used for macro- and micro-hardness tests, with a) surface along x and b) surface along y.

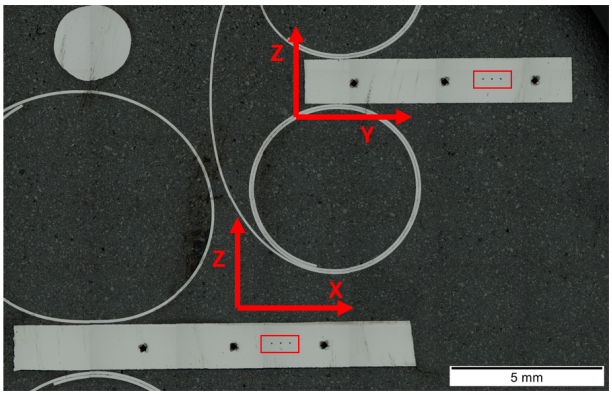

Figure 2.19: Locations of macro- and micro-hardness indentations on cross-section along x and along y inside slices, with micro-indentations in red frames.

2.9 Nano-indentation analysis

2.9.1 Equipment used

The machine used is the Hysitron TI 980 Nano-indenter shown in Fig.2.20. It is equipped with a low load and a high-load indenter, which was the one used here, allowing indentation depths between 100 nm and 1000 nm.

The hardness is measured using a Berkovich indenter which consists of a three-sided pyramidal tip with an angle of 65.3° between the faces and the vertical axis. The hardness directly provided by the software is obtained using the following formulas [16]:

$$H = \frac{F}{A} \tag{2.4}$$

Where F is the applied load and A is the projected area computed using:

$$A = \frac{\sqrt{3}}{4}a^2 \tag{2.5}$$

where a is the length of one side of the indentation in the material, which is given by:

$$a = h \cdot 2\sqrt{3} \cdot tan^2(65.3) \tag{2.6}$$

.

Therefore, the projected area is computed with:

$$A = 24.56h^2 \tag{2.7}$$

But the depth h, corresponding to the displacement of the indenter, needs to be adjusted because the material undergoes elastic deformation. The Oliver and Pharr model suggests using the depth correction [16]:

$$h_p = h - \epsilon\frac{F}{S} \tag{2.8}$$

with $\epsilon = 0.75$ and S is the stiffness.



Figure 2.20: Hysitron TI 980 Nanoindenter [8].

2.9.2 Experimental approach

The nano-indentation was conducted on three samples with varying VED, chosen from the optimal processing window. The indenter was programmed to apply a constant displacement of 500 nm with a loading time of five seconds preceded and followed by loading and unloading periods of 5 seconds. The measurements were performed on a grid of 41 by 41 indentations with a distance of 7.5 μm between two adjacent points, which covers an area of 300 by 300 μm. This grid size corresponds to several MPs but the indentations are too large for the identification of the Heat Affected Zone (HAZ). The grid was positioned on the samples to analyse the last layer printed as shown in Fig.2.21.

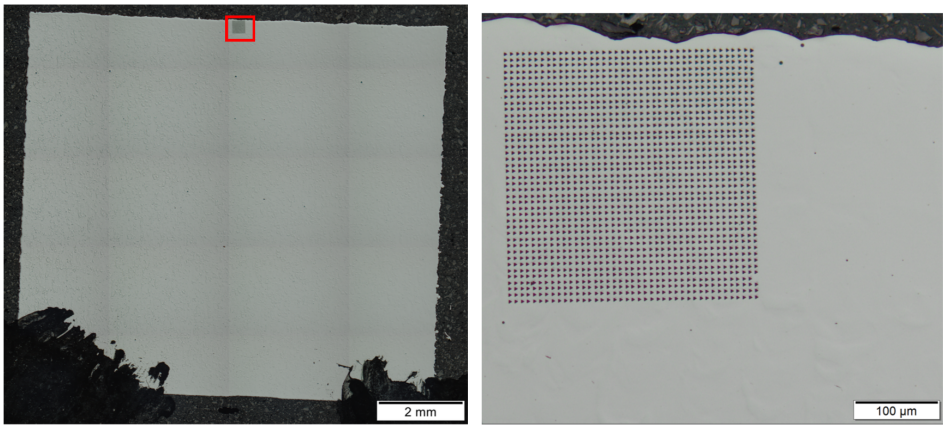

(a) (b)

Figure 2.21: 41 x 41 nano-indentation grid on sample 12 observed with OM using a) 2.5x magnification and b) 20x magnification.

2.10 Scanning electron microscope (SEM) analysis

2.10.1 Equipment

The Tescan Clara SEM with ultra-high resolution and multimodal imaging, shown in Fig.2.22 was used. This SEM allows reaching magnifications much larger than those obtained with the OM. Image and data acquisition were performed with the Tescan Essance software and Esprit Bruker software.

It makes it possible to clearly identify the cellular structure thanks to the generation of images based on secondary electron detection and backscattered electron detection where light elements appear darker. So, in some cases, the images obtained can give a first idea of the distribution of the elements within the material.

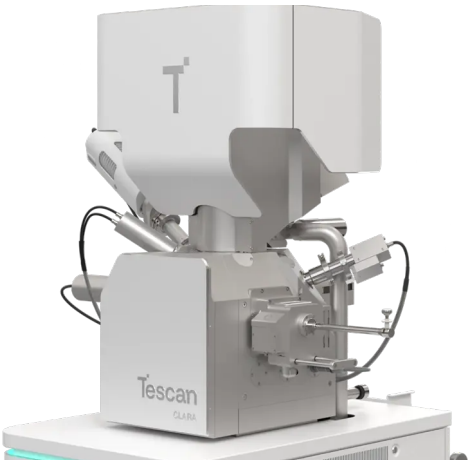

Figure 2.22: Tescan Clara scanning electron microscope with ultra-hight resolution multimodal imaging [62].

2.10.2 Samples preparation

Before the analysis with the electron microscope a chemical etching was performed on the samples that were selected. The samples were immersed in Aqua regia, a solution composed of 1/4 nitric acid at 65% concentration and 3/4 hydrochloric acid at 37% concentration. This reveals the cellular structure for the Energy-Dispersive X-ray (EDX) analysis and also the melt pool which were characterised using the optical microscope. Then a conductive silver paint was applied on the samples as shown in Fig.2.23, it allows a connection to be made with the platform and avoid charge accumulation. For the Electron Back-Scattered Diffraction (EBSD) analysis, a second polishing was performed. Similar to the process presented in section 2.6 but this time it started directly with the 1200-grit paper and finished with the oxide polishing suspension (OPS) solution containing 0.25 μm particles applied to a Chem cloth for ten minutes.



Figure 2.23: Samples after chemical treatment with silver paint near the first layer.

2.10.3 Analyses conducted

Several types of analysis were conducted on the different types of samples studied here. For the cubic samples, a few samples with varying VED were chosen for EDX and EBSD analysis. The EDX analysis was performed to precisely identify the possible compositional variations such as oxide inclusion and to observe the cellular microstructure. Only two samples were analysed, including the one considered optimal. The analysis was performed along a straight line and also over areas. Then, the EBSD analysis was conducted to identify the grain orientations and morphologies. The mean grain size was also obtained corresponding to the diameter of the equivalent circle.

After the tensile tests, a fractographic analysis was conducted on the fracture surface to understand the mechanism of failure. Another EBSD analysis was also performed on samples taken from the remaining material after machining the tensile specimens, the same samples used for the hardness tests shown in Fig.2.18. This allowed the comparison of the microstructure between the different scanning strategies.

Chapter 3

Results

3.1 Cubes analysis

3.1.1 Density

3.1.1.1 Pycnometer analysis

Table 3.1 summarises for each sample the scan speed and laser power values applied and the corresponding conventional and corrected VED values, the average densities and the associated relative densities are given using as reference 8.19 g/cm^3. Each pycnometer measurement used to calculate the average densities is listed in Table A.1 in Appendix i. Before conducting a deeper analysis with the porosity characterisation obtained using OM, some observations can already be drawn from Table 3.1 and from Fig.3.1. Variations in density and relative density between samples, as a function of VED*, can be seen in Fig.3.1 although no clear trend is visible.

First, it is seen that most of the samples show a relative density $> 99.7\%$ which is considered the reference percentage to have a near fully dense material. This value was chosen to be consistent with the research by [60] on which this study is based. Additionally, several samples, i.e. samples 10, 12, 18, 19, 20 show relative densities $> 99.9\%$. So, it seems that the preheating temperature of 200°C was an appropriate choice when only considering the density measured with a pycnometer.

The three samples with the highest relative densities are samples 10, 18, and 19, as can be seen in Table 3.1. One of these three processing parameters configurations was chosen for the blocks discussed in section 3.2. Obviously a higher scan speed makes the entire printing process faster but the VED must be checked too. A too low VED leads to higher cooling rates and higher residual stresses, whereas a too high VED leads to lower cooling rates and consequently larger grains which decreases the hardness of the material. Based on these criteria, the processing parameters of sample 19 seem to be the most suitable.

Sample	Scan speed [mm/s]	Laser power [W]	VED [J/mm^3]	VED* [J/mm^3]	Density [g/cm^3]	Relative density [%]
1	700	100	59.52	68.58	8.1310	99.28
2	800	100	52.08	60.01	8.1683	99.74
3	900	100	46.30	53.34	8.1745	99.81
4	1000	100	41.67	48.01	8.1602	99.64
5	700	125	74.40	85.73	8.1578	99.61
6	800	125	65.10	75.01	8.1722	99.78
7	900	125	57.87	66.68	8.1691	99.74
8	1000	125	52.08	60.01	8.1104	99.03
9	700	150	89.29	102.88	8.1677	99.73
10	800	150	78.12	90.02	8.1874	99.97
11	900	150	69.44	80.01	8.1807	99.89
12	1000	150	62.50	72.01	8.1847	99.94
13	700	175	104.17	120.02	8.1766	99.84
14	800	175	91.15	105.02	8.1776	99.85
15	900	175	81.02	93.35	8.1745	99.81
16	1000	175	72.92	84.01	8.1696	99.75
17	700	200	119.05	137.17	8.1702	99.76
18	800	200	104.17	120.02	8.1876	99.97
19	900	200	92.59	106.69	8.1894	99.99
20	1000	200	83.33	96.02	8.1844	99.93

Table 3.1: Density and relative density obtained from pycnometer and 2D optical cross-sections analysis respectively, with scan speed and laser power and the corresponding classical and modified VED of each sample.

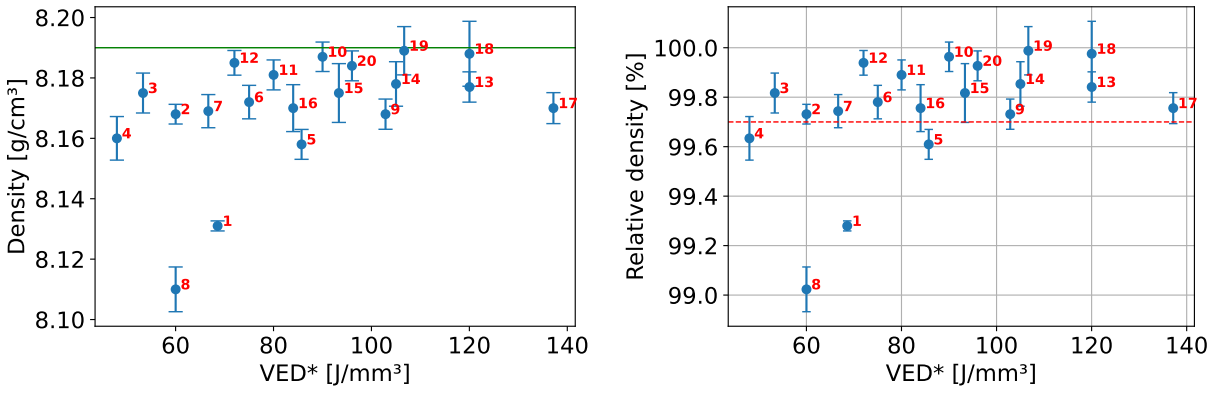

(a) (b)

Figure 3.1: a) Sample densities and b) relative densities as a function of VED^* with the reference density of 8.19 g/cm^3 indicated with the green line and the near fully dense material threshold of 99.7% indicated with the red dashed line.

The PV processing map obtained is shown in Fig.3.2, showing the regions where the relative densities are below the 99.7% threshold. This is mainly the case when low laser powers are applied i.e. 100 and 125 W. However, no clear correlation can be made with the scanning speed. Among the four samples below the threshold, two were printed with the lowest scan speed and the other two were printed with the highest velocity. The other samples printed at these powers but with medium scanning speed have acceptable relative densities as shown in Table 3.1 and in Fig.3.1b. So, a more detailed analysis must be conducted using the different microscopes to determine the type of porosity encountered and identify the optimal processing window.

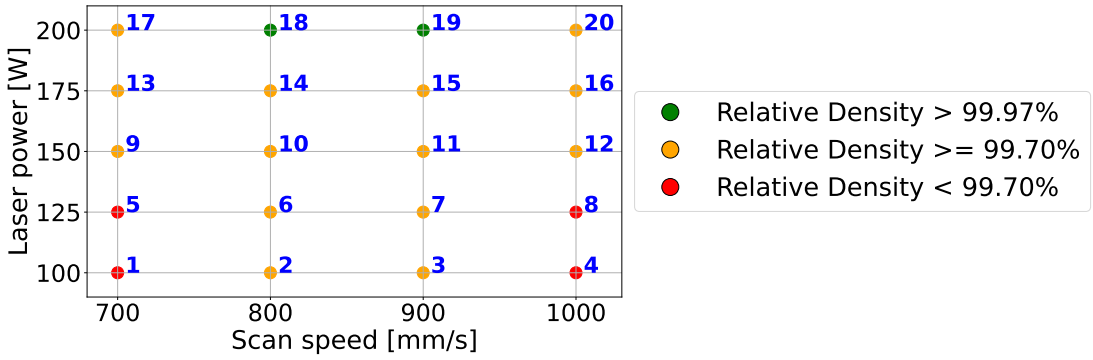

Figure 3.2: PV processing map

3.1.1.2 Optical microscope analysis

The results of the relative densities and the relative surface densities are compared in Table 3.2, where the relative surface densities are the averages of the results obtained with the two thresholds used. It can be seen that the two methods of measurement give similar results. This is clearly highlighted in Fig.3.3, where linear and quadratic regressions were performed. With ideal measurements the linear regression should yield a slope equal to one, which is almost the case with a slope equal to 1.091. Sample 8 was not taken into account in the regression because it distorts the results due to an excessively large variation between the relative densities obtained with the different methods. This sample has the worst density measured with the pycnometer but shows a low internal porosity percentage as given in Table 3.2 and shown in Fig.3.4. To obtain more accurate results with the OM, analyses should be performed on several cross-sections to provide a better estimate of the porosity percentage inside the sample.

Sample	VED* [J/mm^3]	Relative density [%]	Relative surface density [%]
1	68.58	99.28	99.15
2	60.01	99.74	99.91
3	53.34	99.81	99.89
4	48.01	99.64	99.74
5	85.73	99.61	99.57
6	75.01	99.78	99.93
7	66.68	99.74	99.97
8	60.01	99.03	99.97
9	102.88	99.73	99.58
10	90.02	99.97	99.94
11	80.01	99.89	99.97
12	72.01	99.94	99.98
13	120.02	99.84	99.84
14	105.02	99.85	99.92
15	93.35	99.81	99.97
16	84.01	99.75	99.98
17	137.17	99.76	99.63
18	120.02	99.97	99.88
19	106.69	99.99	99.96
20	96.02	99.93	99.98

Table 3.2: Relative densities obtained with pycnometer measurements and relative surface densities obtained with OM with the corresponding VED^*.

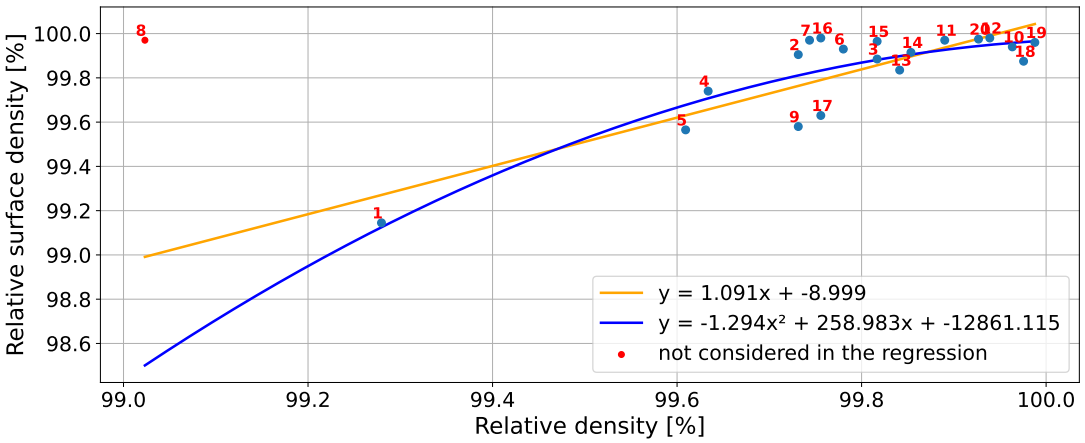

Figure 3.3: Linear and quadratic regression of the relative surface density values obtained with OM as a function of the relative densities obtained from pycnometer measurements.

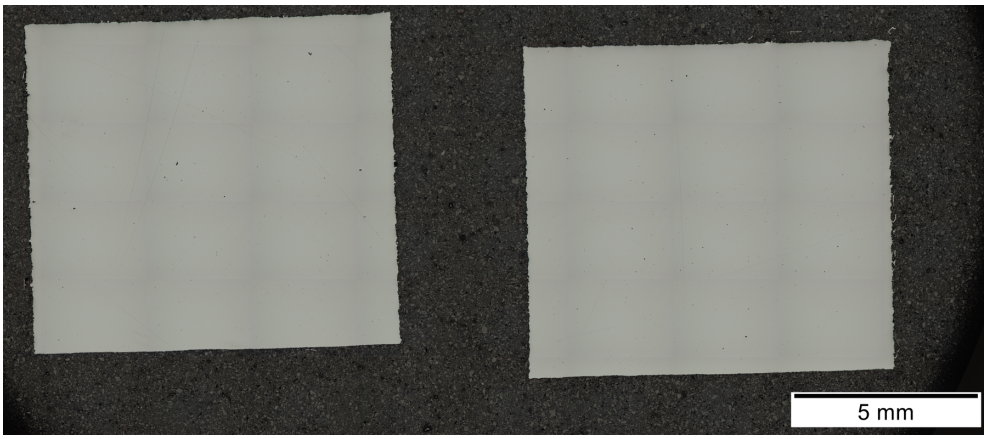

Figure 3.4: Cross-section view of sample 7 on the right and sample 8 on the left with 2.5x magnification.

The cross-section of sample 19 shown in Fig.3.5c, contains very little porosity. The other samples with a relative density above 99.7% with the pycnometer and with good internal density are the samples 11, 12, 15, 16, 19 and 20 shown in Fig.3.5. Therefore, these six samples determine the optimal processing parameter window which is defined between 900 and 1000 mm/s for the scanning speed and between 150 and 200 W for the laser power.

Other samples show the common porosities encountered with the LPBF method. As seen in Fig.3.6, samples 13 and 17 printed with the lowest scanning speed and with laser powers of 175 and 200 W, respectively. Both show many small spherical pores typical of the trapped gas bubble, often encountered in what is called keyhole regime. The samples 1, 2, 3, 4, 5 and 9 present similar porosity with irregular shape and larger than those in other samples. As seen in sample 1 in Fig.3.7, the porosities clearly correspond to a lack of fusion. This occurs mainly in the samples printed using low laser power i.e. 100 W for samples 1, 2, 3, 4 and 125 and 150 W for samples 5 and 9, respectively.

The other samples are at an intermediate stage, they exhibit less porosity than those mentioned in the previous paragraph but still present more porosity than the optimal samples. Indeed, the samples gives a discrete variation between the different regions, but the transition from one mode to another is a continuous phenomenon. More samples with smaller differences between processing parameters should be printed to obtain a more precise definition of the optimal window limits.

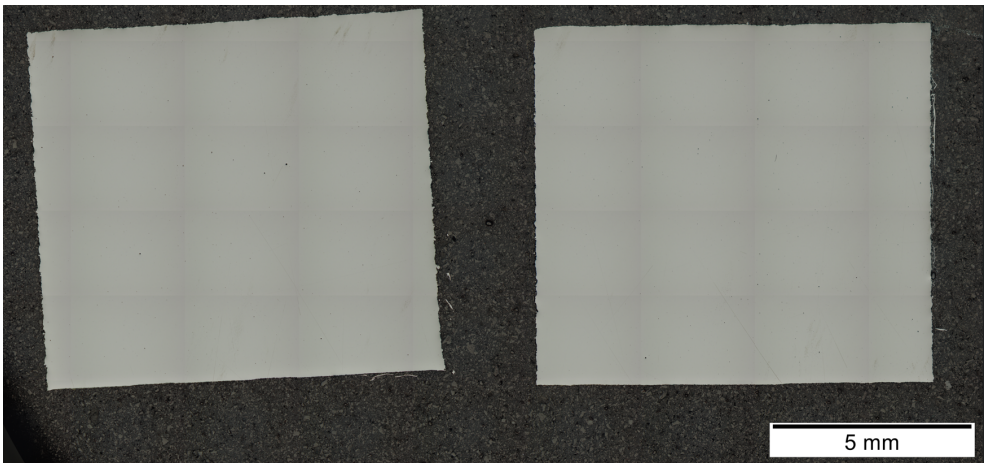

(a) Sample 11 on the right and sample 12 on the left.

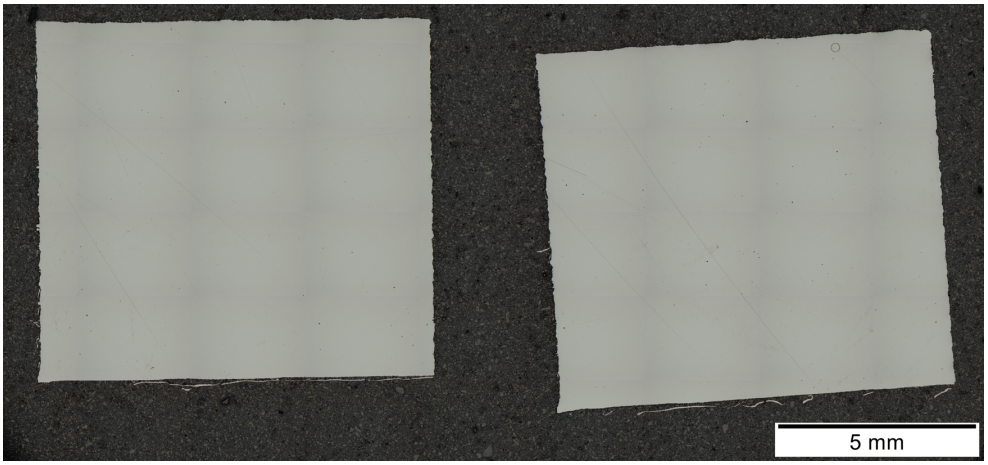

(b) Sample 15 on the right and sample 16 on the left .

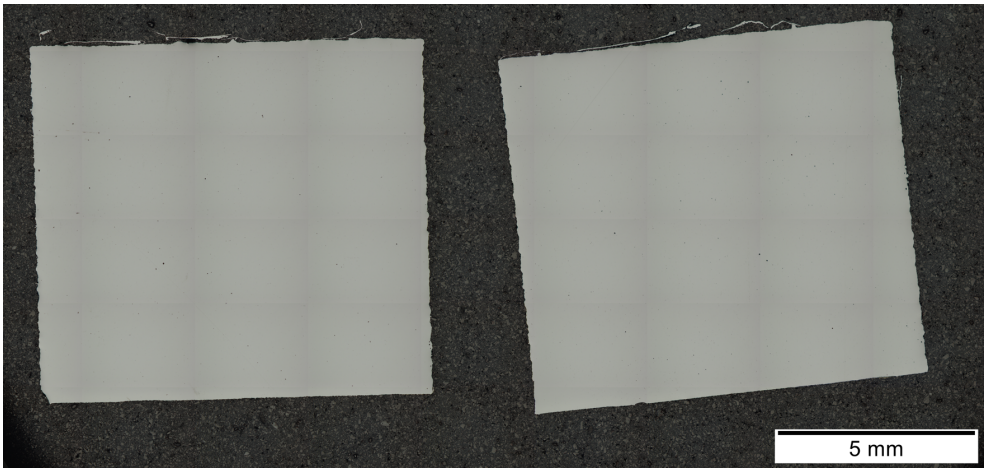

(c) Sample 19 on the right and sample 20 on the left.

Figure 3.5: Cross-section of samples with the best internal densities observed using OM at 2.5x magnification.

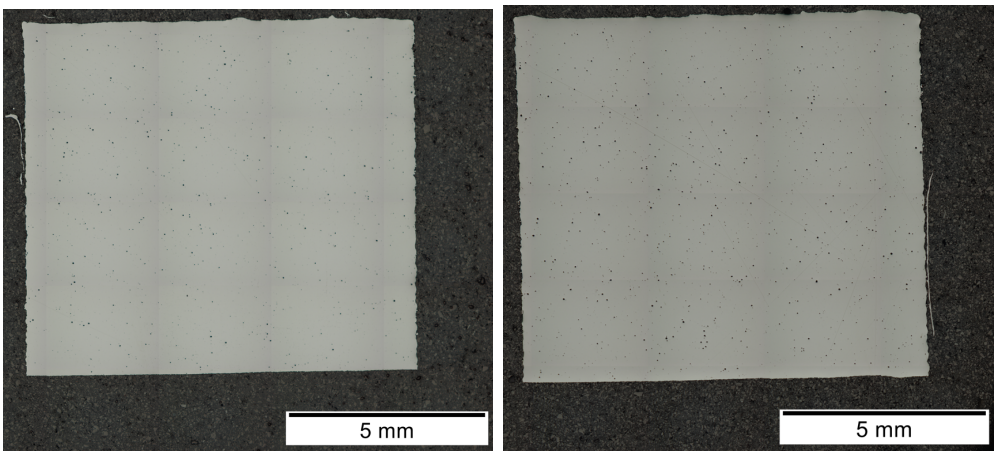

(a) (b)

Figure 3.6: Cross-section view of: a) sample 13 and b) sample 17 at 2.5x magnification showing spherical porosity corresponding to entrapped gas during solidification.

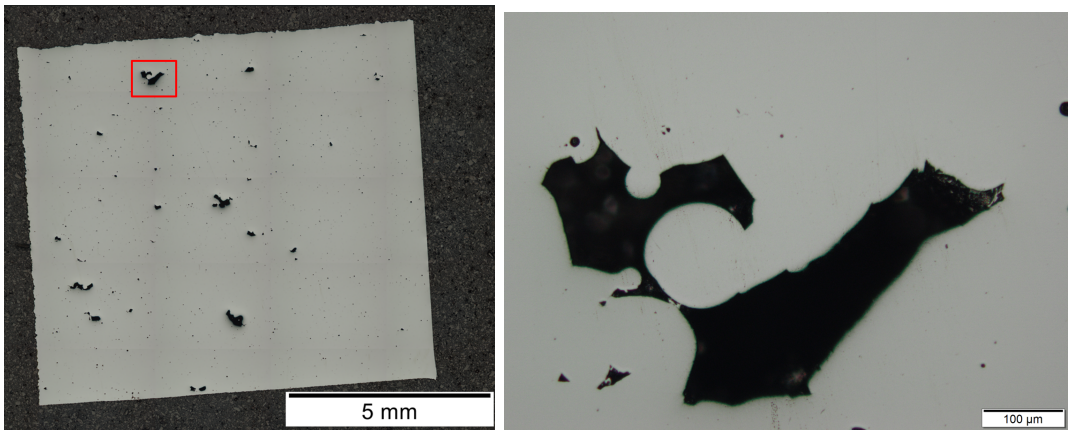

(a) (b)

Figure 3.7: a) Optical microscope view of sample 1 cross-section observed with 2.5x magnification b) close-up view showing porosity with characteristic lack of fusion shape observed with 10x magnification.

3.1.2 Melt pool (MP) characterisation

The dimensions of the melt pool, i.e., the depth of the last layer and the curvature radius of the samples were analysed using Stream Motion software as shown for sample 11 in Fig.3.8. The seven samples, i.e. the six samples in the optimal processing window and sample 17, allow the analysis of the melt pool geometry over a relatively large VED* range spanning up to 65 J/mm^3 as can be seen in Table 3.3.

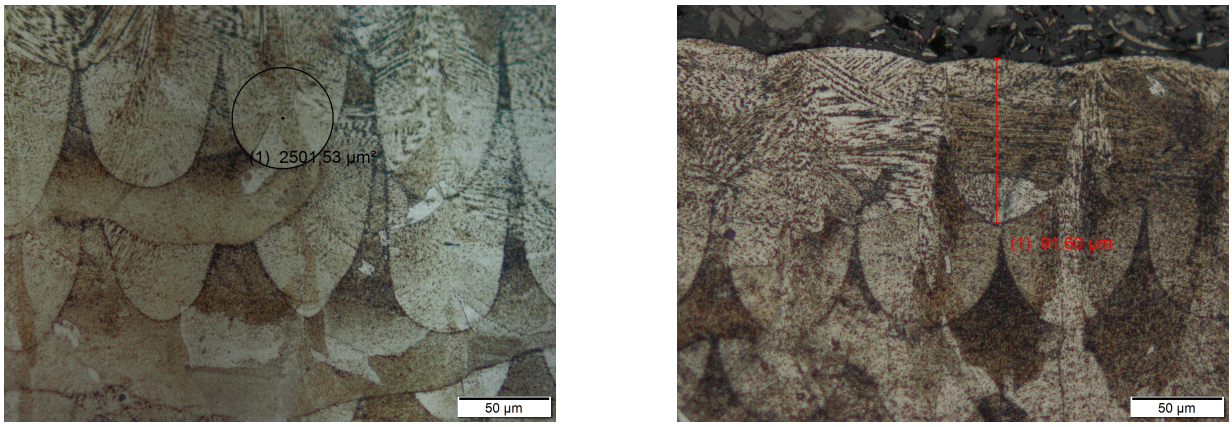

(a) (b)

Figure 3.8: Characterisation of melt pool geometry for sample 11 using Stream Motion software using a 20x magnification lens.

The MP depth and curvature show large standard deviations which make the curve shapes unreliable, but a trend can still be identified. The depth increases as VED* increases which is consistent with observations in the literature [27] [45] [53]. Most studies measured the width at the top of the melt pool and show an increase with VED. Here, the curvature radius refers to the width at the bottom and shows a decrease when $VED*$ increases. These two observations are not contradictory. It seems that the MP boundaries at the bottom become sharper at higher VED which leads to smaller curvature radii.

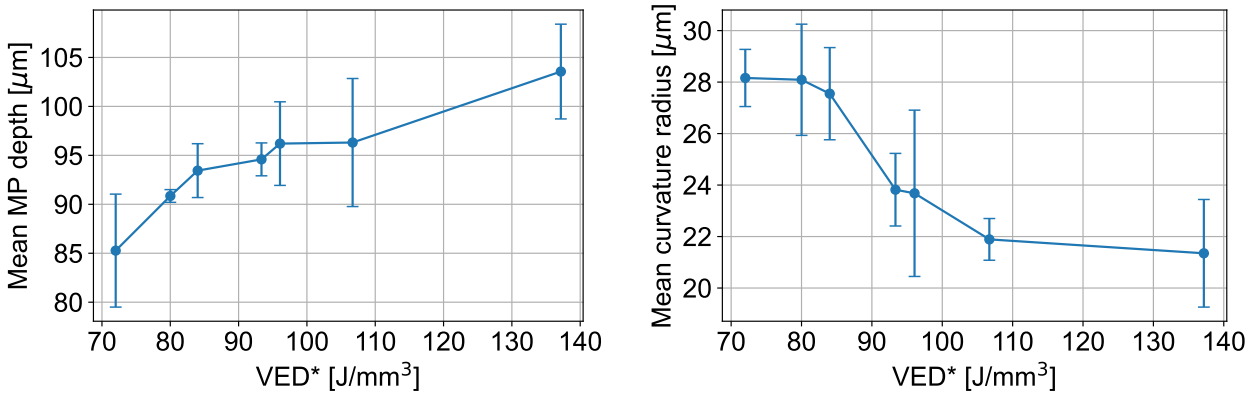

(a) (b)

Figure 3.9: Melt pool dimensions as a function of VED* with a) the melt pool depth of the first layer and b) the curvature radius.

Sample	VED* [J/mm^3]	Mean MP depth [μm]	Standard deviation	Mean curvature radius [μm]	Standard deviation
12	72.01	85.27	5.77	28.16	1.11
11	80.01	90.85	0.65	28.09	2.16
16	84.01	93.44	2.75	27.55	1.79
15	93.35	94.59	1.68	23.82	1.41
20	96.06	96.20	4.27	23.68	3.23
19	106.69	96.31	6.54	21.89	0.81
17	137.17	103.56	4.84	21.35	2.09

Table 3.3: Melt pool dimensions for varying VED* obtained with optical microscope measurements.

3.1.3 Microstructure characterisation

3.1.3.1 Cellular structure and chemical composition

The two samples analysed with the SEM are sample 19, and sample 17 to confirm the presence of gas porosity and to check the presence of oxides. EDX analysis performed over a line, is illustrated for both samples in Fig.3.10, and the obtained results are shown in Fig.3.11 and 3.12. Two EDX mappings are shown in Appendix iv, and give similar results to the linear analyses: the observed elements correspond to the expectation and no oxide inclusion was found. This will further supports that 200°C is the optimal preheating temperature compared to 300°C and 500°C investigated in previous research [60].

The SEM images allow the clear identification of the cellular microstructure as can be seen in Fig.3.10. The cell size is of the order of one micron sometimes a slightly smaller and shows elongated shapes in varying directions.

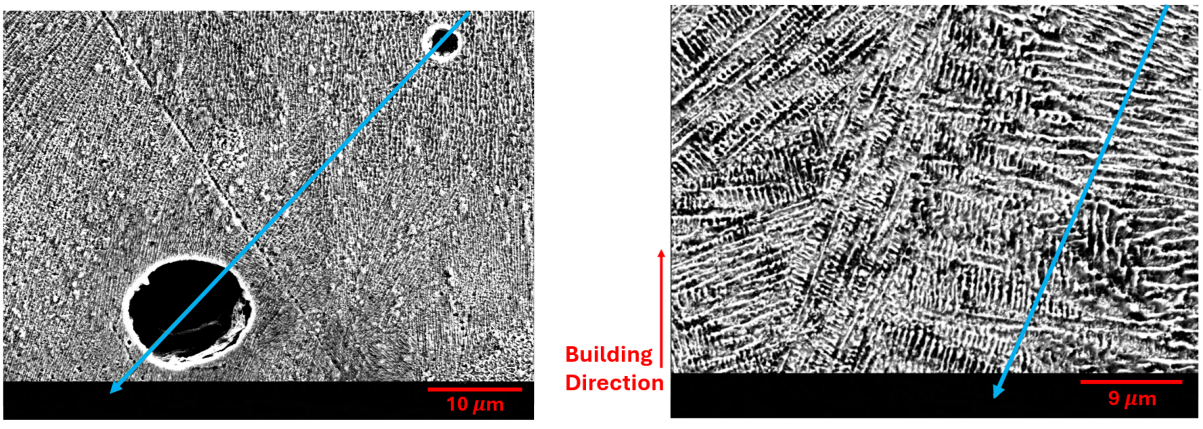

(a) (b)

Figure 3.10: Linear EDX analysis locations on a) sample 19 and b) sample 17.

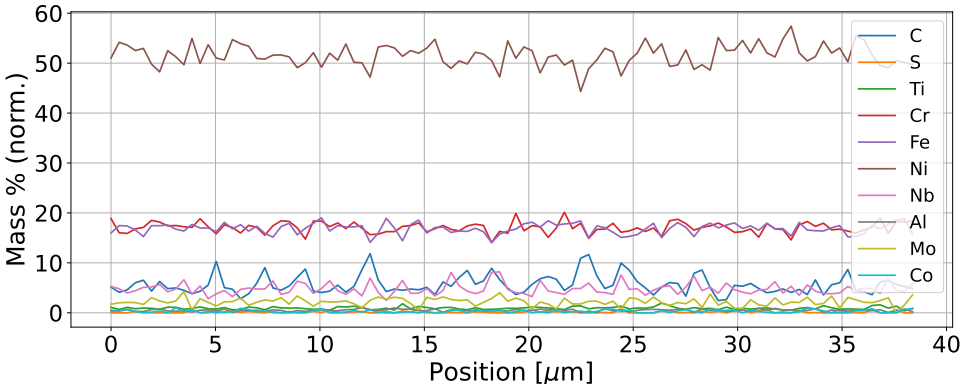

(a)

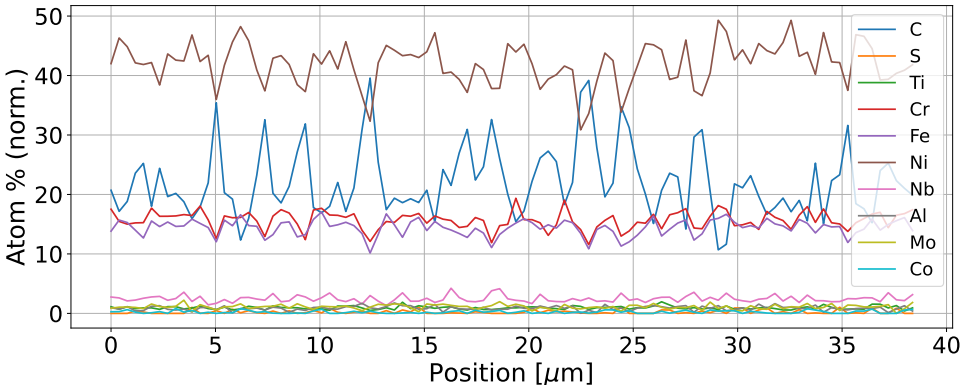

(b)

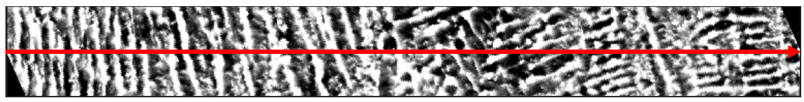

(c)

Figure 3.11: a) Mass percentage, b) atomic percentage obtained from EDX analysis on sample 17 along the straight line in c), enhancing the local chemical gradients due to the cellular-like structure.

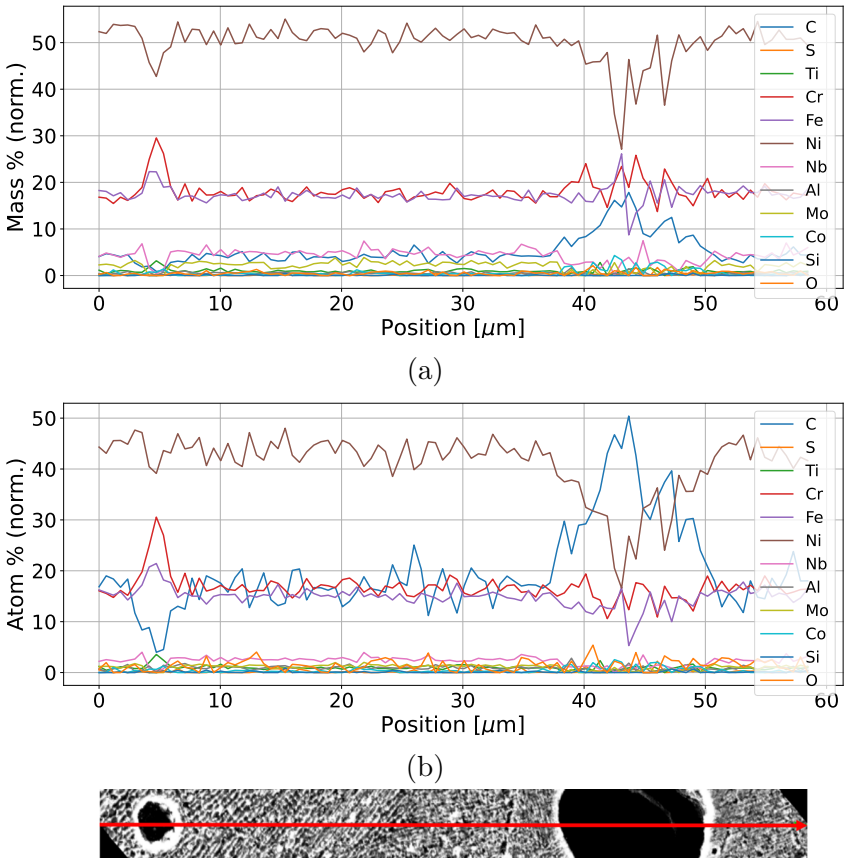

Figure 3.12: a) Mass percentage, b) atomic percentage obtained by EDX analysis on sample 19 along the straight line in c).

3.1.3.2 Grain size characterisation

The EBSD analysis reveals a clear difference between the grain size of sample 11, sample 12 and samples 15 and 19. The mean grain size is 83.3 μm for sample 12, 30 μm for sample 11 and 47.2 and 45.3 μm for samples 15 and 19, respectively. As shown in Fig.3.13, their morphologies are similar especially for samples 11, 15 and 19, the grains seem to follow the MP boundary and do not exhibit the typical epitaxial growth as is often the case with AM processes. However, sample 12 shows elongated grains aligned with the BD at some location, and therefore seems to be printed close to the conditions for the epitaxial growth obtained at lower VED, as observed in [21]. Since this study was conducted within optimised processing parameter window, the structures obtained are neither equiaxed nor columnar, but they are in an intermediate stat forming what can be called fan-shaped grains [35]. The VED* increases, taking the values 72.01, 80.01, 93.35 and 106.69 J/mm^3 for samples 12, 11, 15, 19 respectively. Therefore, the grain size presents a minimum when increasing the VED*, which corresponds to the transition from columnar to equiaxed

grains [35]. Another interesting observation is that successive grains are aligned along the BD, but every 150-200 μm, a shift to the right or to the left is observed all along the layer.

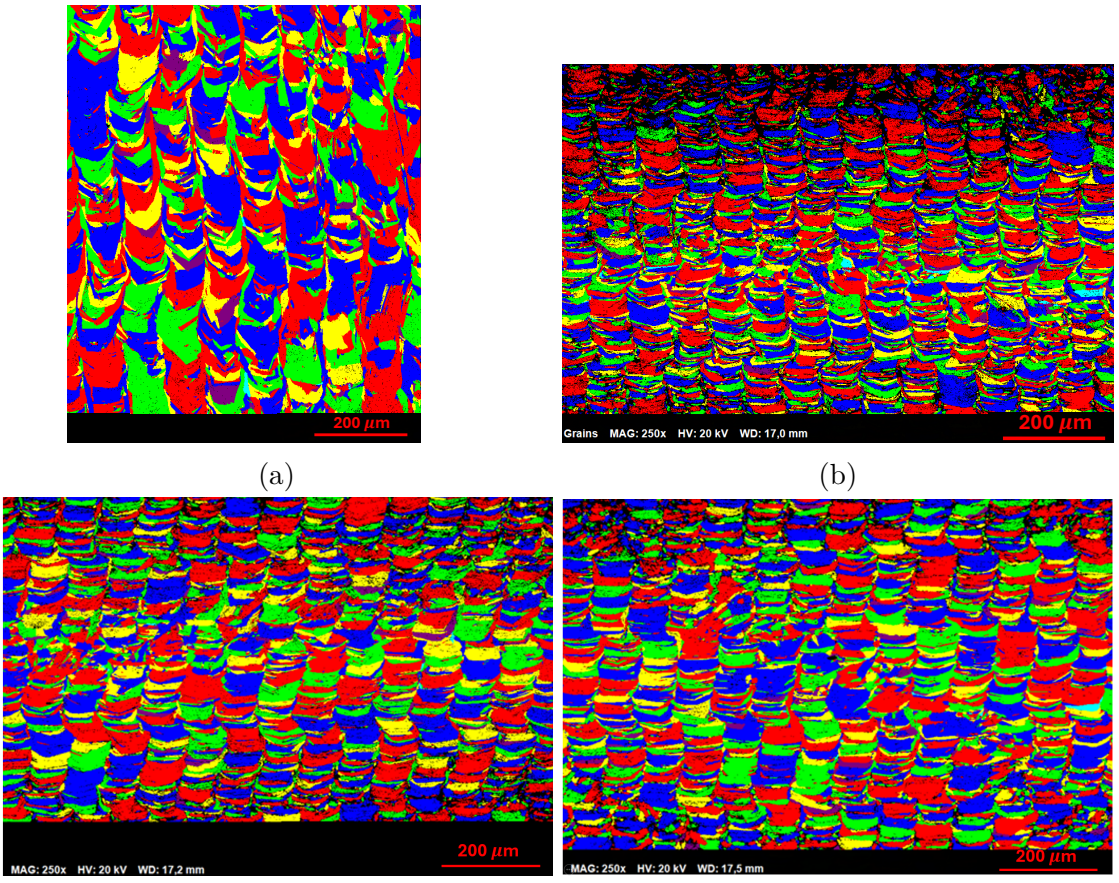

(a) (b)

(c) (d)

Figure 3.13: EBSD analysis performed near the top layer in the XZ plane of a) sample 12 with VED* = 72.01 J/mm^3, b) sample 11 with VED*=80.01 J/mm^3, c) sample 15 with VED* = 93.35 J/mm^3, d) sample 19 with VED* = 106.69 J/mm^3

3.1.4 Hardness analysis

3.1.4.1 Macro- and micro-hardness

The average of the nine indentations for each sample is given in the graph in Fig.3.14 and the values are presented in Table A.3 in Appendix v. It can be seen that both scales give homogeneous results between the samples, the macro-scale tests give values between 300 and 310 HV10 and the micro-scale tests give values between 330 and 340 HV0.3 for each sample. Sample 1 has a very large standard deviation for the macro-hardness test, certainly due to internal porosity which can cause significant variations in the results from

one location to another. This sample is the one with the largest porosities as seen in Fig.3.7a with a size sometimes larger than the indentation size shown in Fig.2.15. The results differ from one scale to another, the macro-hardness depends on the cellular structure and the residual stresses whereas the micro-hardness depends more on the dislocation density and the possible precipitates already present in the as-built material [60].

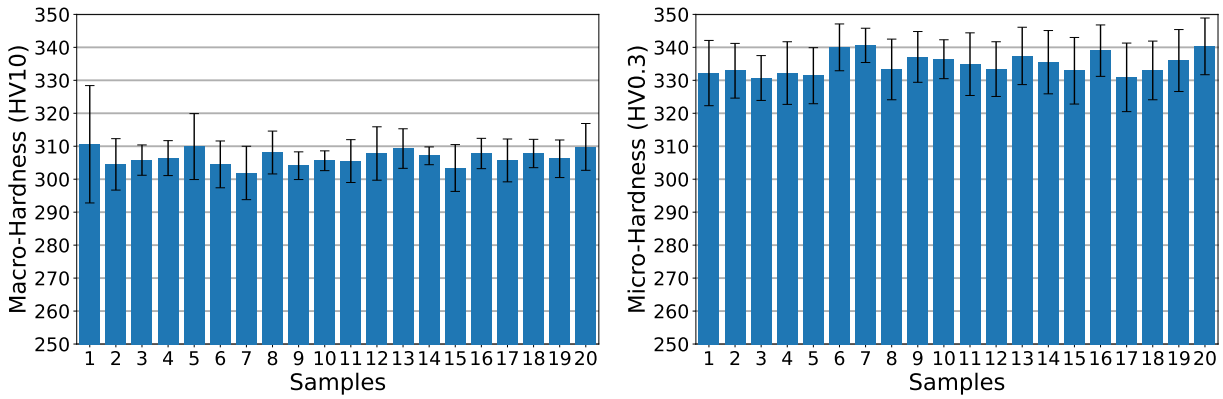

(a) (b)

Figure 3.14: Vickers hardness values of each sample with a) macro-hardness (HV10) and b) micro-hardness (HV0.3).

3.1.4.2 Nanohardness

Nano-hardness highlights several phenomena when comparing samples 12, 15 and 19 with different VED values. The 41 x 41 indentation grids, covering areas of 300 x 300 μm as shown in Fig.3.15, allow the study of hardness variations within several melt pools and grains near the top layer by imposing an indentation depth of 500 nm. The 1681 indentations in each grid were successfully done as seen in Fig.3.15 where it is possible to distinguish rough patches corresponding to grains highlighted by the OPS treatment.

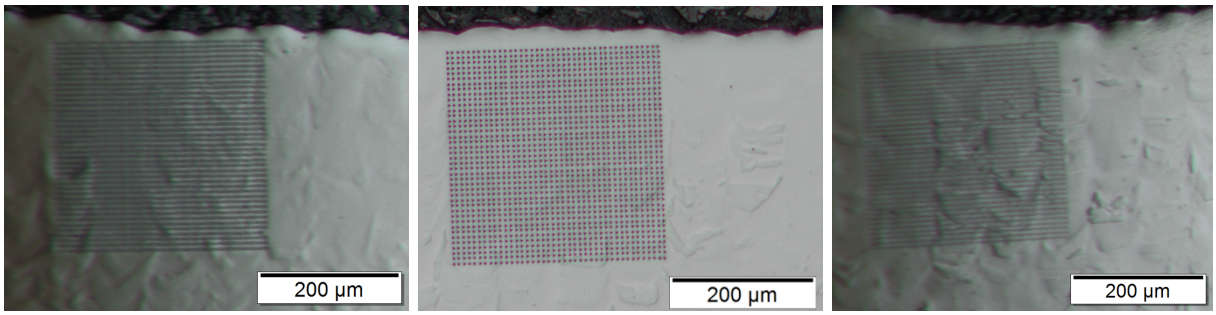

(a) (b) (c)

Figure 3.15: 41 x 41 nano indentation grids near the last layer covering a 300 x 300 μm^2 areas with imposed depth of 500 μm on a) sample 12, b) sample 15 and c) sample 19.

First of all, the heat maps shown in Fig.3.16 highlight the different nano-hardness distributions near the top layer. A gradient along the BD is visible in each sample, but the hardness increase occurs deeper below the surface as VED increases. This can be linked to the MP depth shown in Fig.3.9a where the depth was shown to increase with VED. Therefore, with a smaller depth the previous layers are not completely remelted and an annealing effect occurs, which increases the hardness. With higher VED, the MPs are deeper and a larger volume of material is remelted which leads to lower hardness over a larger region near the top of the sample.

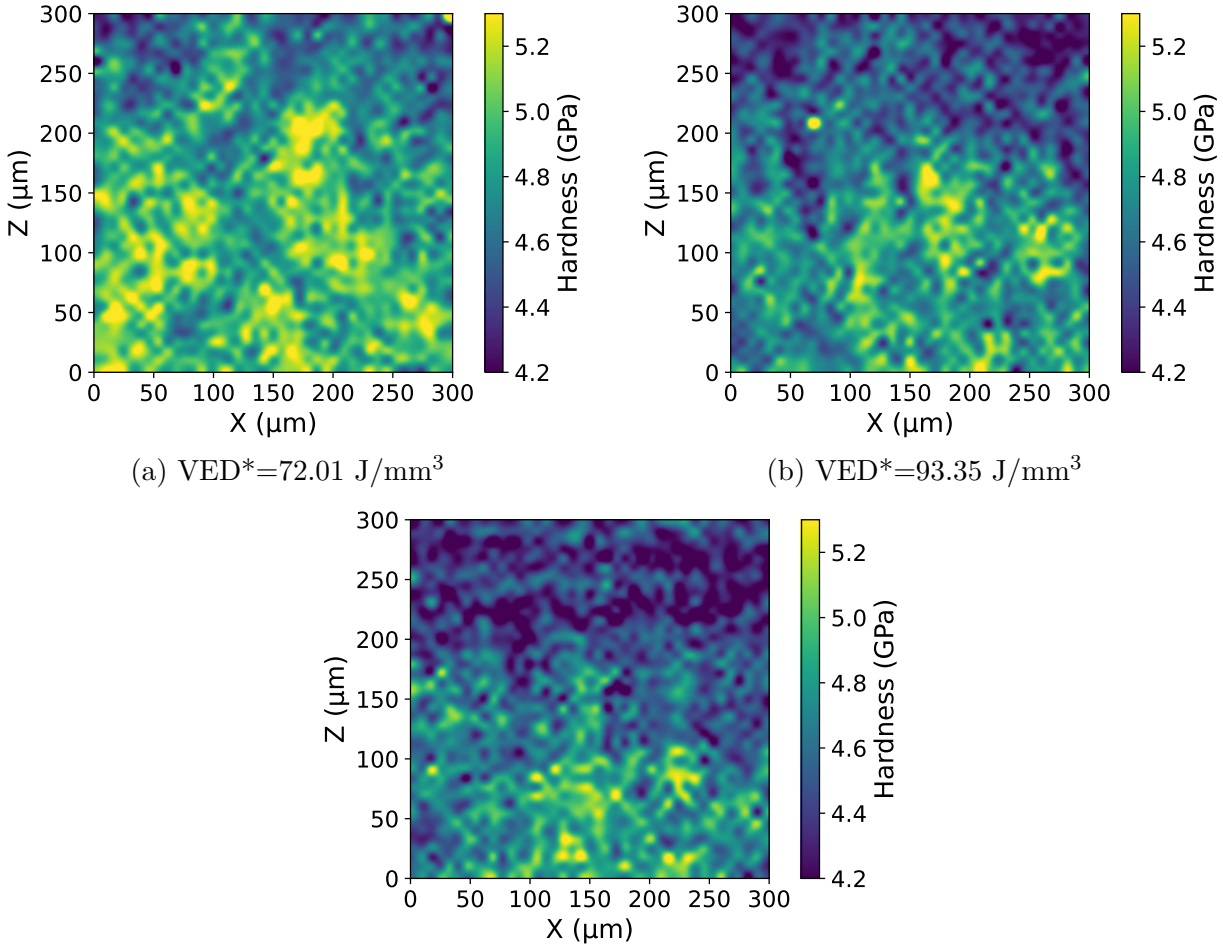

(a) VED*=72.01 J/mm^3

(b) VED*=93.35 J/mm^3

(c) VED*=106.69 J/mm^3

Figure 3.16: Nanohardness of a) sample 12 and b) sample 15 and c) sample 19 with imposed displacement of 500 μm on 41x41 indentation grid.

So, the three samples give similar results which is consistent with the previous hardness tests performed at larger scales. Also, at the nano-scale, hardness seems to depend mainly on the thermal history and Fig.3.17 shows the hardness distribution for the three samples

studied, which are Gaussian distributions, as expected. It can be seen that the mean value tends to decrease slightly when VED* increases. The histograms show similar standard deviations in all cases, indicating that the three distributions are restricted to the same range between 4 and 5.5 GPa. This last observation confirms that similar phenomena occur inside the samples but changes in VED* lead to a shift in the mean value within this range.

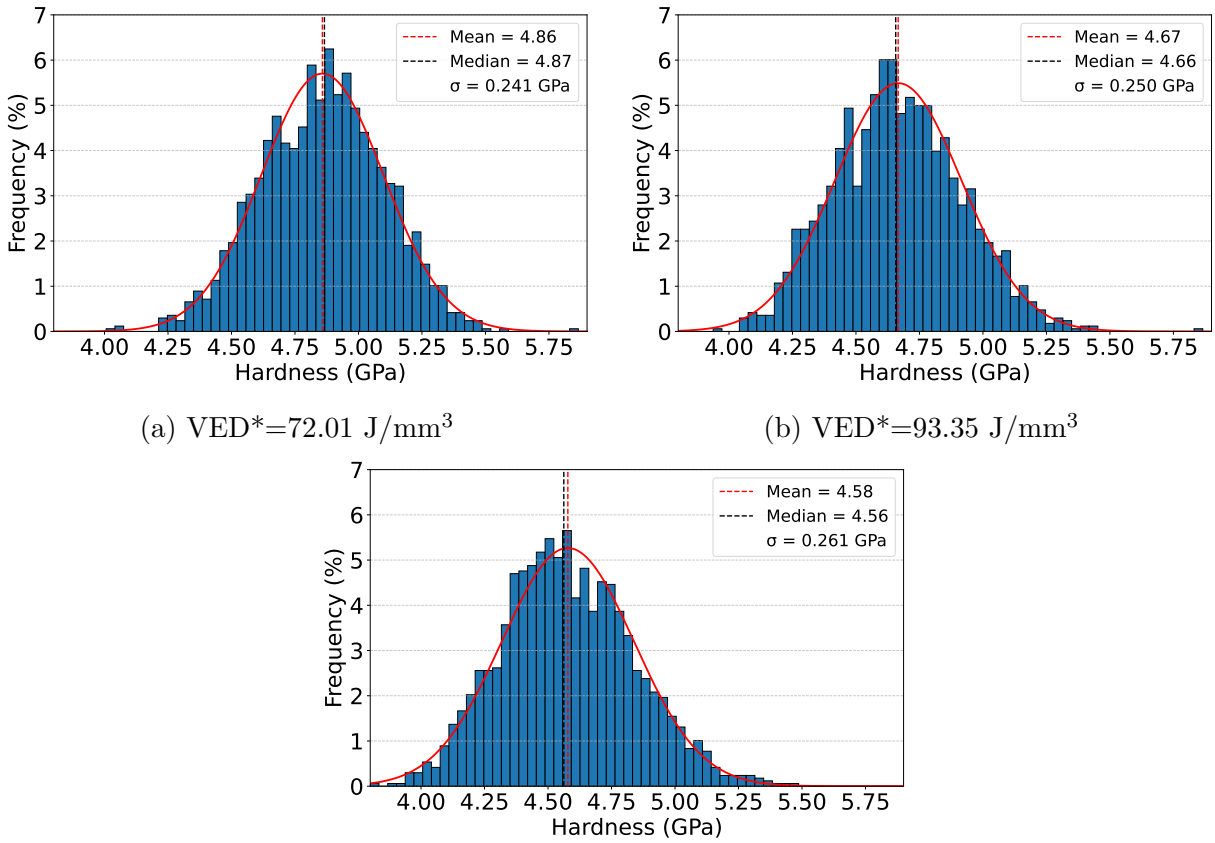

(a) VED*=72.01 J/mm^3

(b) VED*=93.35 J/mm^3

(c) VED*=106.69 J/mm^3

Figure 3.17: Histogram of nanohardness frequency in a) sample 12, b) sample 15 and c) sample 19.

3.2 Blocks analysis

At the end of the printing process, the four blocks show a good surface finish. Probably due to a defect in the recoater, the two blocks positioned on the right exhibit a continuous straight line aligned with the recoater direction, located near their right edge, as visible in Fig.3.18. No interruption was made during the process but a line perpendicular to the build direction is present on the four lateral faces of each block. To assess the precision of the machine, several measurements of the length, the width and the height of the block were taken with digital callipers. The length varies within the range [39.93; 40.06] mm, the width within [3.00; 3.12] mm and the height within [19.87; 20.00] mm. It should be noted that the blocks were kept on the base plate at 200° for hours at the end of the printing process, which could have led to slight settling.

In the rest of the study, the top left block will be referred to as block 1, the top right block as block 2, the bottom left block as block 3 and the bottom right block as block 4. Thus, the blocks upstream of the argon flow refer to blocks 2 and 4 and the blocks downstream of the argon flow refer to blocks 1 and 3.

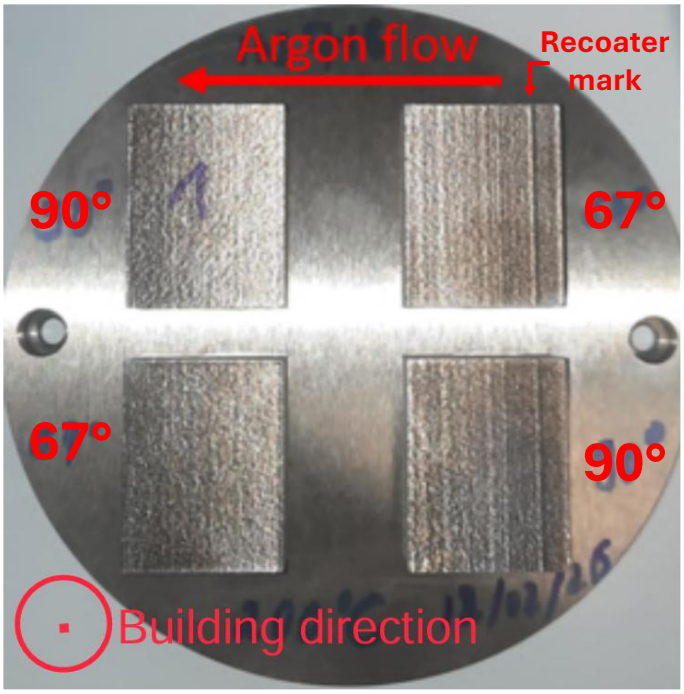

Figure 3.18: Top view of the 4 blocks at the end of the printing process, on the build platform preheated to 200°C, with 90° scanning strategy top left and bottom right and 67° top right and bottom left.

3.2.1 Block top surfaces roughness

The surface roughness analysis of the top surfaces of each block allows the identification of the laser tracks in the last layer in Fig.3.19b, 3.20b, 3.20d, 3.19d and the two scanning strategies can be distinguished. The roughness maps shown in Fig.3.20a and 3.20c exhibit a similar pattern on each block, showing a larger variation near the right and left edges. Blocks 1 and 4, shown in Figs.3.19a and 3.19c, appear to have more homogeneous surfaces. The vertical line on the surfaces of blocks 2 and 4 is clearly visible in Figs.3.19d and 3.20b.

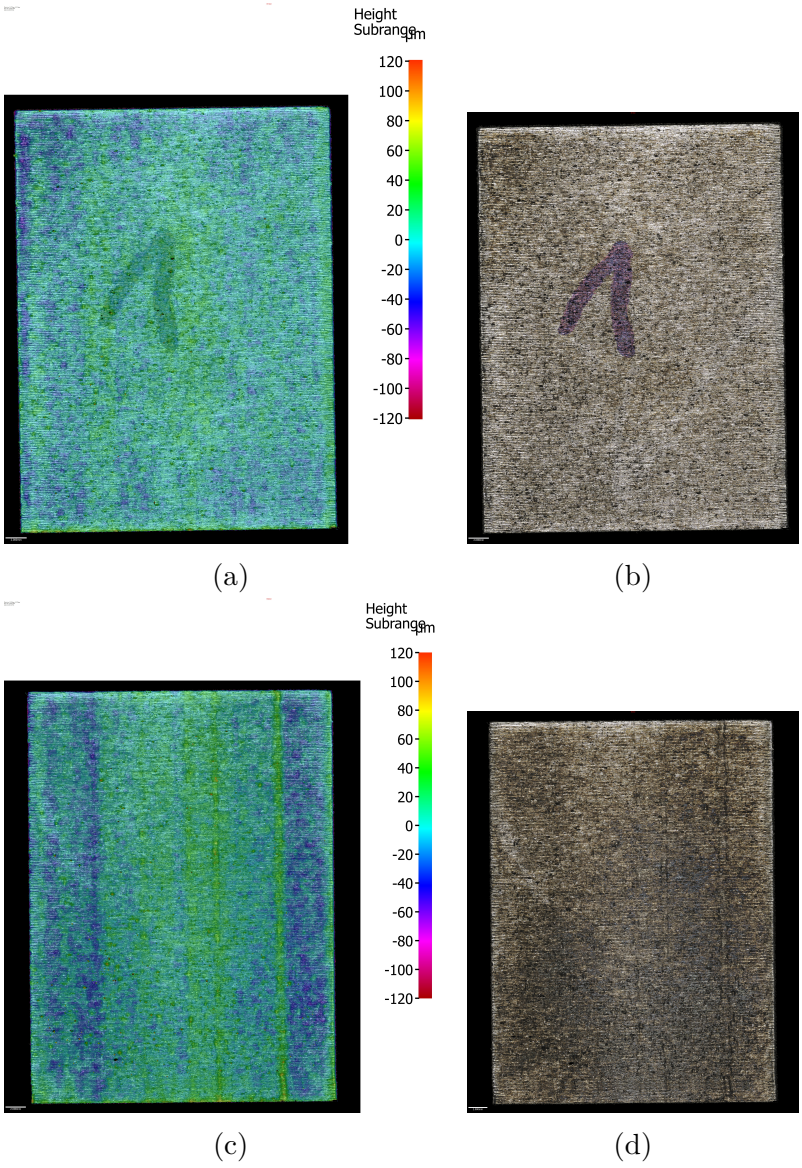

Figure 3.19: Top layer roughness obtained with a 90° scanning strategy with a,b) block 1 and c,d) block 4.

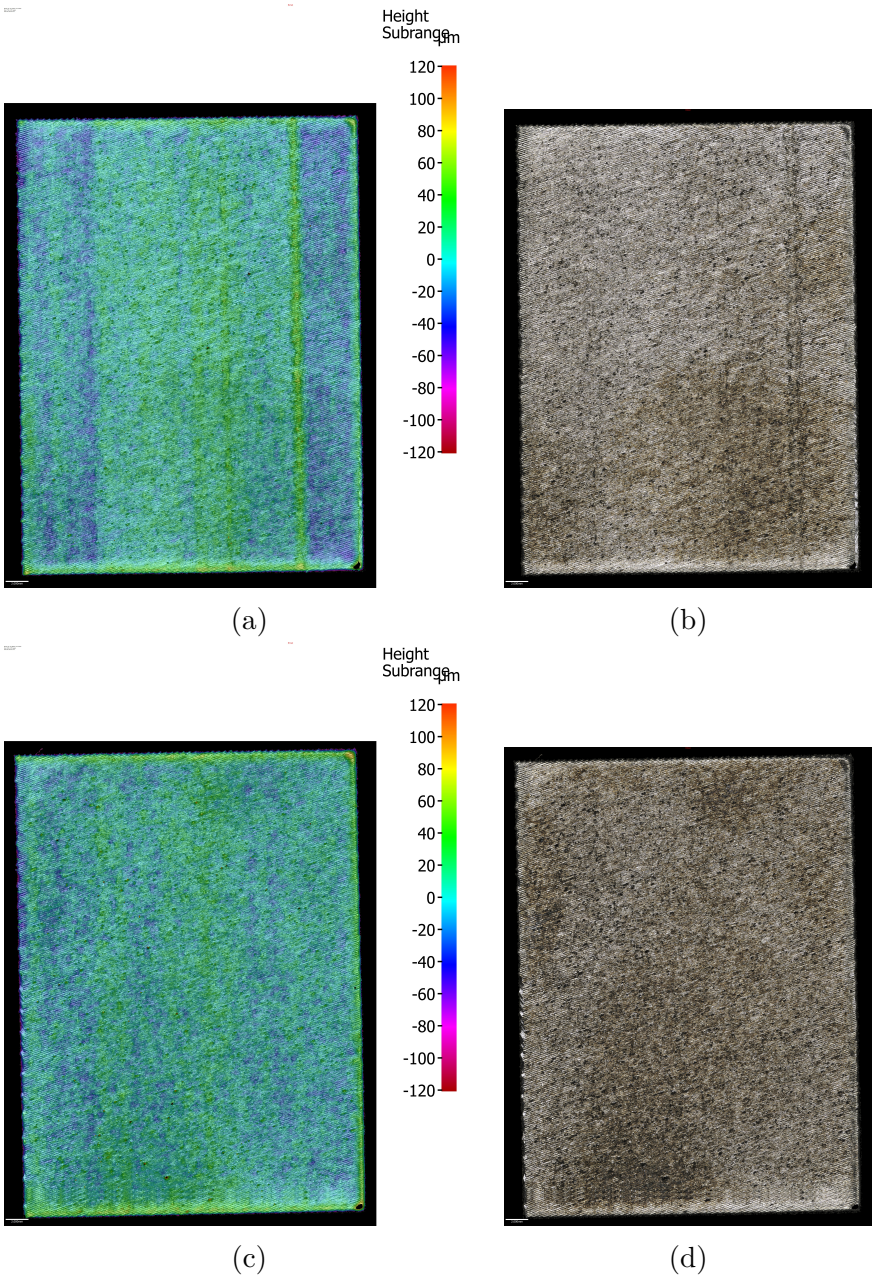

Figure 3.20: Top layer roughness obtained with a 67° scanning strategy with a,b) block 2 and c,d) block 3.

The histograms shown in Fig.3.21 indicate that all distributions are centred around zero with mean values very close to zero as stated in Table 3.4 which demonstrates the relatively homogeneous surface obtained for each block. One difference is that the blocks positioned downstream (blocks 1 and 3) show a higher frequency around zero, which corresponds to a smoother surface. So, the distributions of the upstream blocks are wider compared with those of the blocks printed using the same scanning strategy. Block 1 also has a narrower distribution, as the significant values do not exceed +40 and -40 μm.

Table 3.4 highlights several important points to take into account in addition to the information provided by the histograms. The values for the maximum height represent the difference between the maximum peak height and the maximum valley depth. These values directly provide the largest height variation on the surface. This information is crucial because some very deep valleys and very high peaks can compensate for one another in the mean values. The average height is also given which differs from the mean value by taking only the absolute values of the peaks and the valleys to have a more realistic indication of the average roughness.

Block 1, with the smallest average height is also the block with the highest peak and the deepest valley. So, even if the surface is smoother than the others, it also presents the biggest defects. Compared with block 4, which as printed using the same parameters, a large difference is visible in the maximum height compared to the difference between Blocks 2 and 3 which is smaller. However, no correlation is seen between the values and the position relative to the argon flow. It seems that the blocks using a 67° scanning strategy exhibit less variable characteristics than the 90° strategy and are more predictable.

In fact, the four blocks show a very good surface finish, with small difference, in the order of a few tens of microns. At this stage, i.e. during experimental research on simple geometries, such small variations are not really significant, this needs to be considered only for specific applications.

Parameters [µm]	**Block 1 (90°) top left**	**Block 2 (67°) top right**	**Block 3 (67°) bottom left**	**Block 4 (90°) bottom right**
Mean value	0.091	0.068	0.029	0.096
Average height	10.579	12.727	11.211	13.406
Maximum peak height	236.525	163.702	151.840	168.779
Maximum valley depth	402.496	360.414	329.179	347.816
Maximum height	639.021	524.115	481.019	516.595

Table 3.4: Height parameters of peaks and valleys on the four block top surfaces.

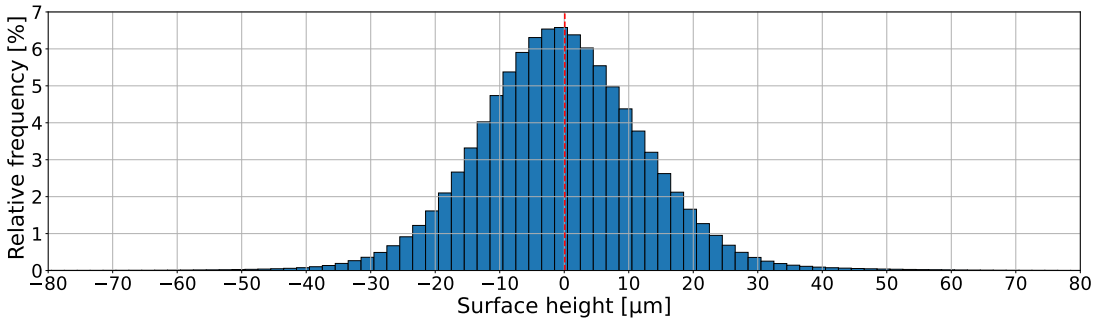

(a) Block 1

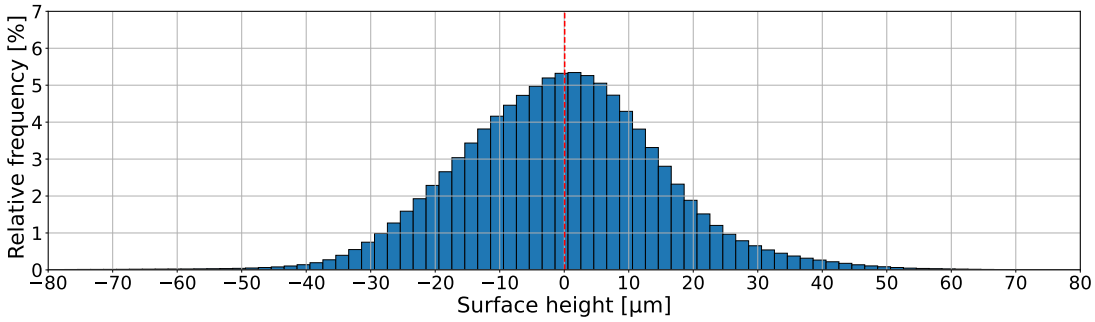

(b) Block 2

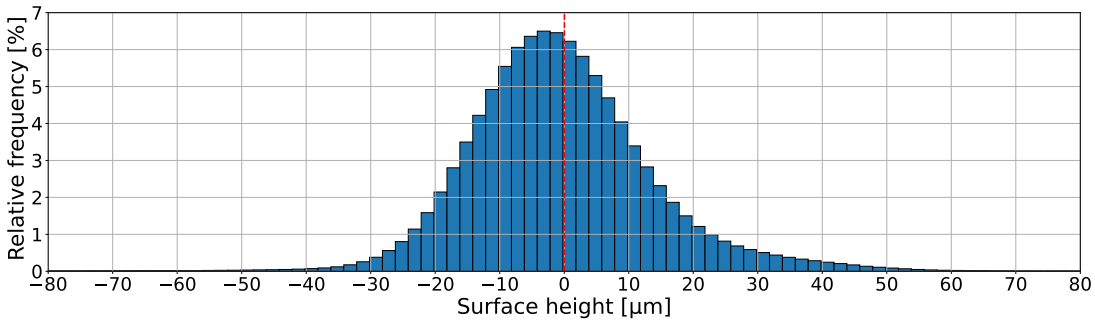

(c) Block 3

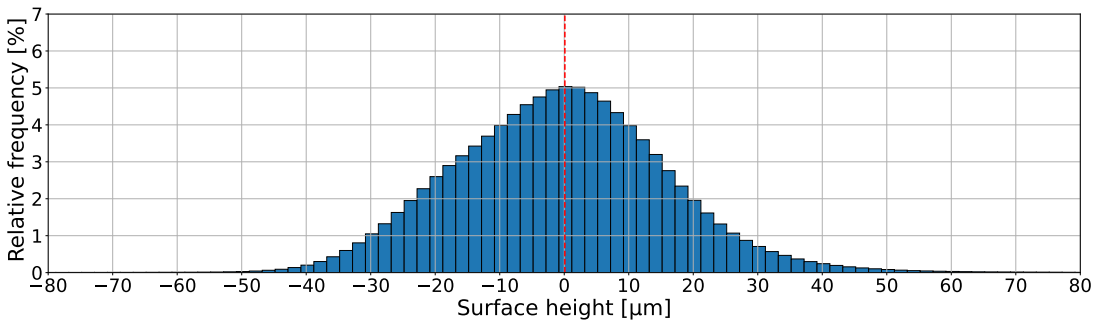

(d) Block 4

Figure 3.21: Histogram of peak height and valley depth distributions on the top layer.

3.2.2 Macro- and micro-hardness on the slices

The results of micro- and macro-hardness tests are given in Table 3.5 and are also shown in Fig.3.22. Compared with the values indicated with the green lines in Fig.3.22 obtained for sample 19, printed using the same processing parameters and a 90° scanning strategy, the results obtained here are much higher in most cases.

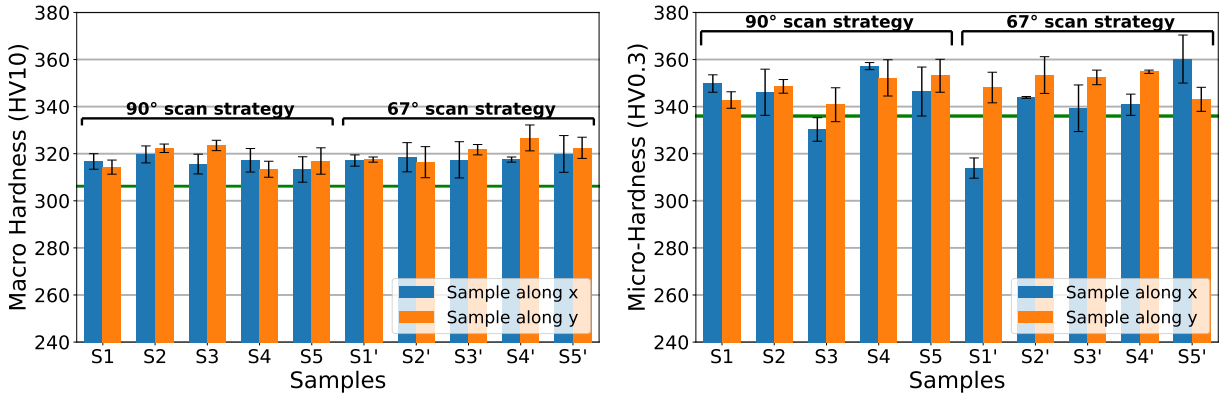

(a) (b)

Figure 3.22: Hardness in sections parallel to the x and y directions in each slices with a) macro-hardness (HV10) and b) micro-hardness (HV0.3).

However, the sections studied here are located 5 mm above the base plate, unlike those analysed in the cubes. It can reasonably be assumed that the temperature in the middle of the blocks is not the same as that at the base. The literature shows that hardness tends to increase at lower temperatures [60] which explains the difference observed compared to the cubes. The temperature of the base plate can also change from one location to another [58]. Due to their size, the cubes are not necessarily affected but the larger blocks may be prone to thermal gradients in the XY plane which explains the large variation between the two directions within the same slices. There is also a 3.5 mm thick layer printed above the studied sections which has induced a greater number of thermal cycles in the rest of the block compared with the cubes. Another significant difference is the environment around the studied zone, the sections here are surrounded by several centimetres of solid material while the sections studied in the cubes were mainly surrounded by unmelted powder. All these differences in the thermal history are linked to the larger size of the blocks, therefore, a comparison between the as-built parts requires a scale factor. However, it is not necessary because a heat treatment must be performed and will affect the material properties linked to the hardness.

Slice	Macro Hardness HV10				Micro Hardness HV0.3			
	Along x		Along y		Along x		Along y	
	MV	SD	MV	SD	MV	SD	MV	SD
S1	316.7	3.3	314.3	3.0	349.8	3.7	342.8	3.5
S2	319.7	3.6	322.3	1.8	346.1	9.8	348.6	2.9
S3	315.6	4.2	323.5	2.2	330.3	5.0	340.8	7.2
S4	317.2	5.0	313.4	3.4	357.2	1.5	352.2	7.7
S5	313.3	5.4	316.9	5.6	346.4	10.4	353.1	7.0
S1'	317.1	2.4	317.5	1.1	313.9	4.3	348.1	6.5
S2'	318.5	6.2	316.4	6.6	343.9	0.4	353.4	7.8
S3'	317.4	7.7	321.7	2.2	339.3	9.9	352.4	3.1
S4'	317.5	1.1	326.7	5.5	340.8	4.5	354.8	0.7
S5'	319.9	7.8	322.5	4.5	360.2	10.2	343.1	5.1
Average	317.29	-	319.52	-	342.79	-	348.93	-
SD	1.82	-	4.03	-	12.44	-	4.89	-
Sample 19	306.2				336.0			
SD	5.7				9.4			

Table 3.5: Mean Values (MV) and Standard Deviation (SD) of macro- and micro-hardness in x and y directions of each slice.

3.2.3 Grain morphology

The slice printed using a 90° scanning strategy exhibits the typical grain morphology referred to as "fan-shaped" [35] observed at "medium" VED values, as can be seen in Fig.3.23. The mean grain size is 42.8 μm similar to the structure observed in sample 19 printed using the same processing parameters already discussed.

The slice printed using a 67° scanning strategy also shows a compact structure but with varying grain shapes and sizes due to the varying laser track orientation and the grain morphology approaches the equiaxed structure at some locations as shown in Fig.3.23b. The mean grain size is much lower than that obtained using 90° strategy and is equal to 34.6 μm. However, this slice presents a very particular characteristic, each grain is enclosed by another grain which forms a boundary around it, clearly visible in Fig.3.23c.

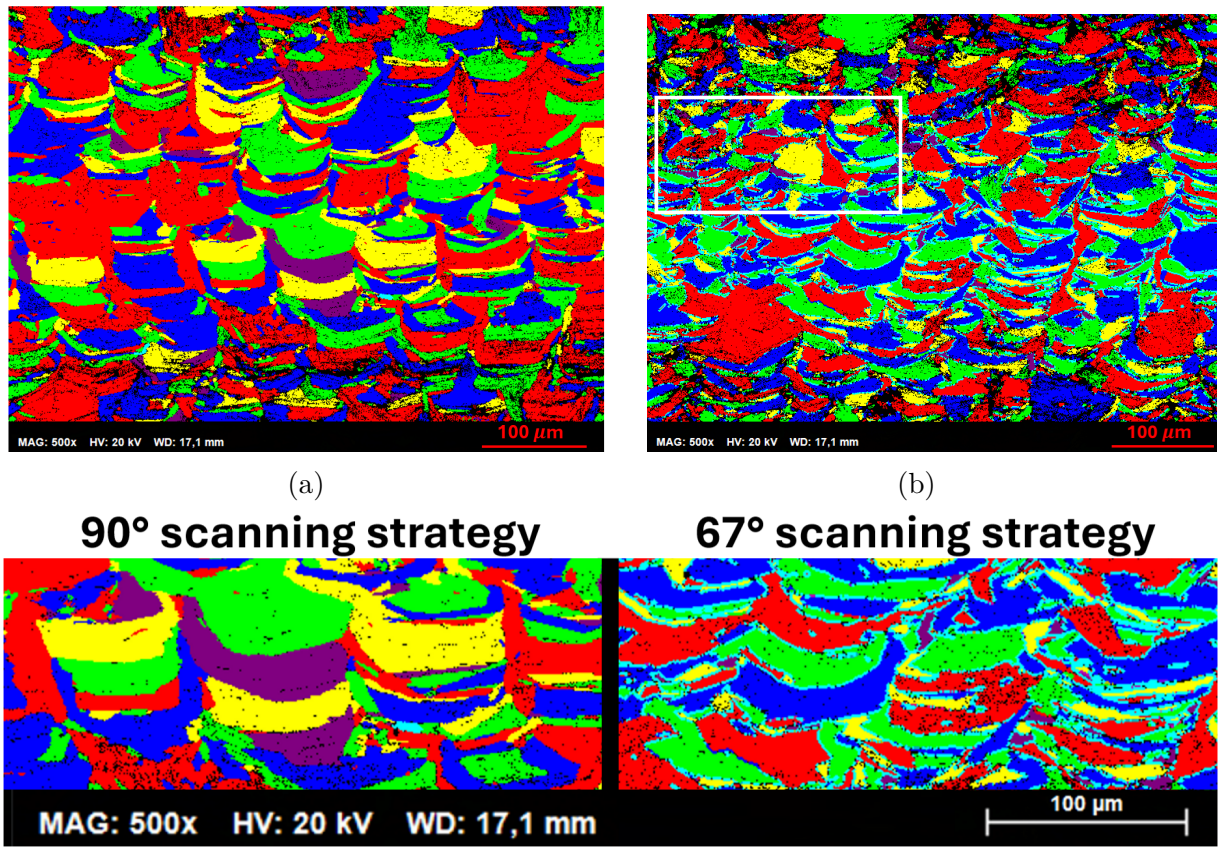

(a) (b)

(c)

Figure 3.23: EBSD analysis of slices with cross-section in YZ plane with a) 90° scanning strategy, b) 67° scanning strategy with equiaxed grains highlighted in white rectangle, c) close-up view on the center of the ROI with cup-shaped grains.

3.2.4 Tensile specimens analysis

3.2.4.1 Verification of failure section locations

As reported in Table 3.6 each tensile specimen fractured in its gauge which ensures the validity of the tensile test results. Fig.3.24 shows measurements for TS1 obtained using the OM.

	Post-fracture gauge length [mm]									
	TS1	**TS2**	**TS3**	**TS4**	**TS5**	**TS1'**	**TS2'**	**TS3'**	**TS4'**	**TS5'**
Part 1	8.09	7.75	8.44	8.60	8.72	8.75	6.77	8.48	8.94	7.53
Part 2	5.21	5.70	4.69	4.19	4.44	4.27	6.57	4.62	4.36	5.72

Table 3.6: Post-fracture gauge length measured from the fracture section to the edge of the grip section.

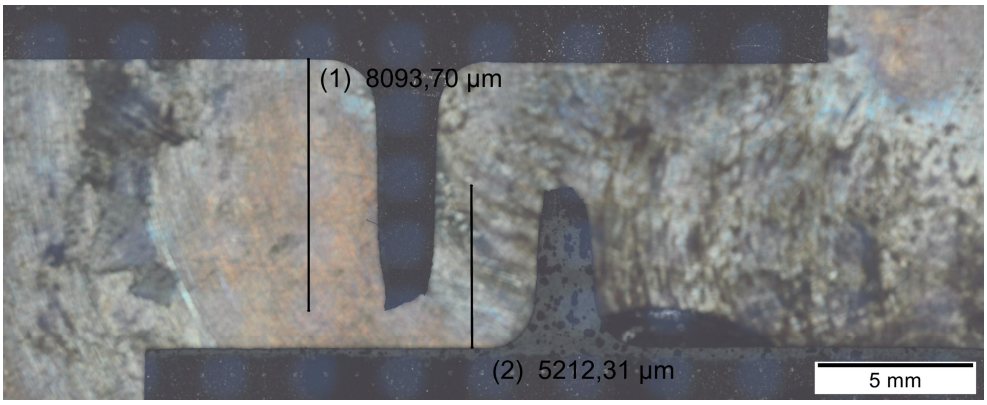

Figure 3.24: Post-fracture gauge length measurements from the failure section to the grip section edge of TS1 using Stream Motion software with OM.

3.2.4.2 Tensile tests

After the tensile tests the engineering stress–strain curves can be obtained as shown in Fig.3.25. It can clearly be seen that the 67° scanning strategy gives higher YS and UTS values for every specimen compared with the 90° strategy. As given in Table 3.7, the smallest YS with the 67° strategy is equal to 794.78 MPa while the largest YS with the 90° strategy is equal to 741.33 MPa. The elongations are generally similar, although the 67° strategy gives the lowest value, equal to 25.96% and the 90° strategy gives the highest value, equal to 33.32% as detailed in Table 3.7. The main difference between the two strategies lies in Young's modulus (E), the mean values of E for the five specimens is equal to 139.74 GPa with the 90° strategy and equal to 193.54 GPa with the 67° strategy, which is closer to the expected value of 200 GPa for In718.

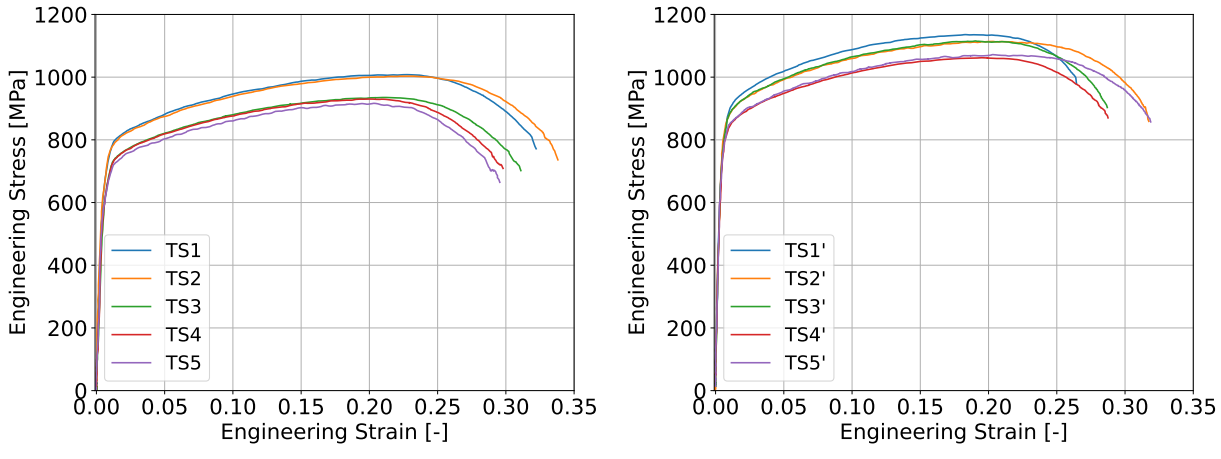

(a) (b)

Figure 3.25: Stress as a function of strain in tensile specimens under unidirectional tensile tests with a) a 90° scanning strategy and b) a 67° scanning strategy.

The set of parameters used here is highly conclusive when comparing the mechanical properties obtained in the literature reported in Table 3.7. The results obtained by *Chen et al.* [12], who used a 67° scanning strategy and a preheating temperature of 200°C, show a Young's modulus much lower than conventional In718 and even lower than those obtained with the 90° strategy. However, they report a very high UTS but a lower elongation than in the present study. The results reported by *Sharma et al.* [52] who also used a 67° scanning strategy but with a preheating temperature of 80°C, show lower YS and UTS values compared with those of specimens printed using the same scanning strategy. Their Young's modulus has an acceptable value and the elongation is much larger than those obtained in this work and is twice the elongation reported in [52].

Tensile specimens	**Young Modulus [GPa]**	**Yield Strength [MPa]**	**Ultimate Tensile Strength [MPa]**	**Elongation [%]**
TS1	150.631	741.33	1014.18	31.71
TS2	149.016	722.79	1008.39	33.32
TS3	132.984	667.57	940.86	30.57
TS4	133.022	672.29	936.61	29.26
TS5	133.055	680.98	924.26	29.06
Mean	139.742	696.992	964.860	30.78
SD	9.221	33.029	42.865	1.78
TS1'	203.303	842.16	1144.11	25.96
TS2'	195.135	843.57	1120.90	31.30
TS3'	201.050	828.80	1122.86	28.25
TS4'	185.971	794.78	1064.84	28.29
TS5'	193.541	802.38	1078.64	31.44
Mean	195.800	822.338	1106.270	29.05
SD	6.819	22.601	33.170	2.40
Chen et al. [12]	127	813	1339	20.1
Sharma et al. [52]	190	564	979	43

Table 3.7: Mechanical properties (i.e., Young's modulus, yield strength, ultimate tensile strength, and elongation) obtained by DIC from tensile tests on specimens printed using 90° and 67° scanning strategies compared with literature data from [12] and [52], both using a 67° scanning strategy and a 200°C and 80°C preheating temperature respectively.

3.2.4.3 Fractographic analysis

Using SEM, the fracture surfaces of the tensile specimens were observed and all specimens exhibit similar patterns consistent with what has already been reported in the literature [74] [12]. A very rough central area can be identified and is highlighted with dashed lines in Fig.3.26 showing the fracture surface of TS3. This corresponds to the fracture initiation

region and is surrounded by slopes extending to the outer edge, similar pattern can be seen in Fig.A.5 and A.6 in Appendix vii showing the other examined tensile specimens. The morphology of these sections ensures that failure begins in the centre and propagates towards the edges and that the failures are not due to surface defects on the specimen.

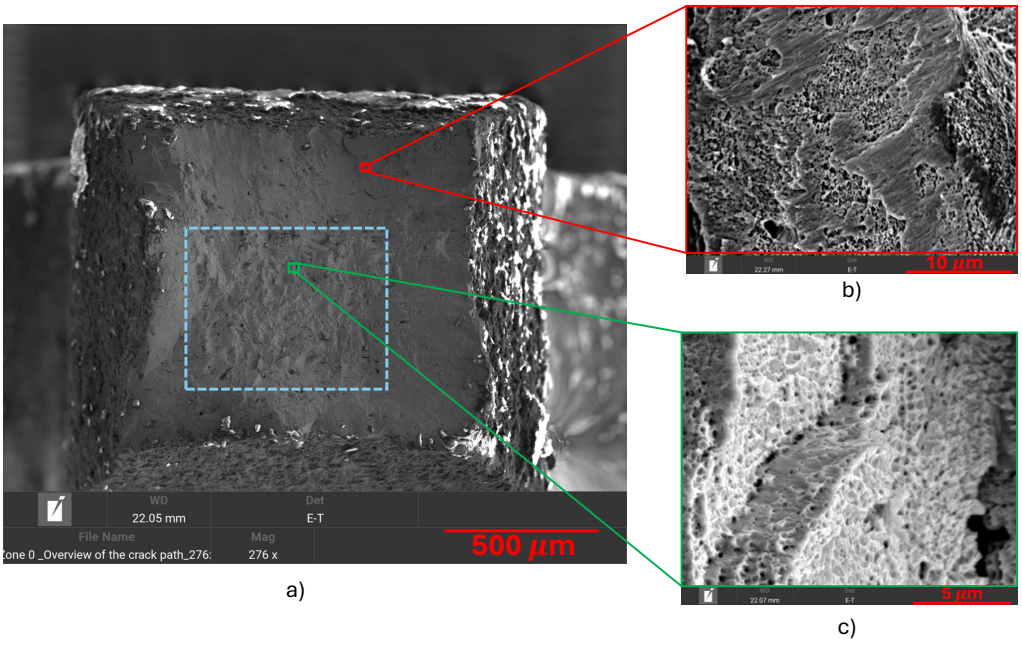

Figure 3.26: Fractography of TS3 with a) overview of the fracture section with rough central area inside dashed line corresponding to the fracture initiation, b) close-up view on dimples and flat area, c) close-up view on secondary crack causing a step-like structure with sheared dimples.

At higher magnification, it can be seen that all the sections are covered with dimples, as shown in Fig.3.27 and also visible in Fig.3.26c. They form a very fine structure, sometimes smaller than one micron. These structures are due to the coalescence of micro-voids and are characteristic of ductile failure [52] [74]. The pores observed are also surrounded by dimples showing that no brittle failure occurred in the material, even in stress-concentration regions, as shown in Fig.3.28a. Not all the observed holes are necessarily porosity but some may be oxide inclusions as confirmed by the EDX analysis of TS1', shown in Fig3.28b, with the EDX results given in Appendix viii in Fig.A.7.

Other observations are similar to all specimens, many sections show secondary cracks leading to step-like morphology and sheared dimples as can be seen in Fig.3.26c. Smoother surfaces, often surrounded by sheared dimples, are observed as shown in Fig.3.26. This is clearly different from the smearing observed in TS3', as shown in Fig.3.28c. This may be due to significant shearing, which leads to the flattening of the dimples.

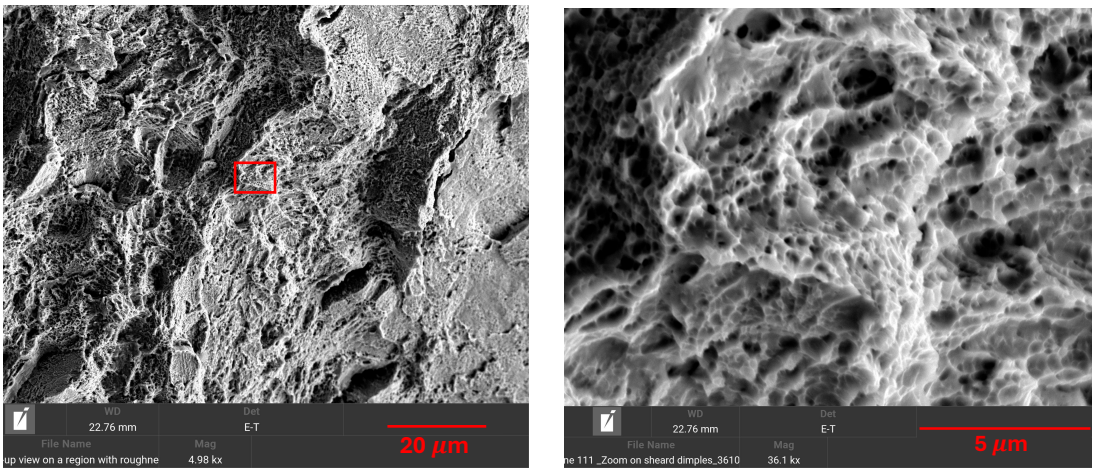

(a) (b)

Figure 3.27: a) Highly irregular and rough area on fracture section of TS2, b) close-up view on red rectangle in Figure a) showing sheared dimples.

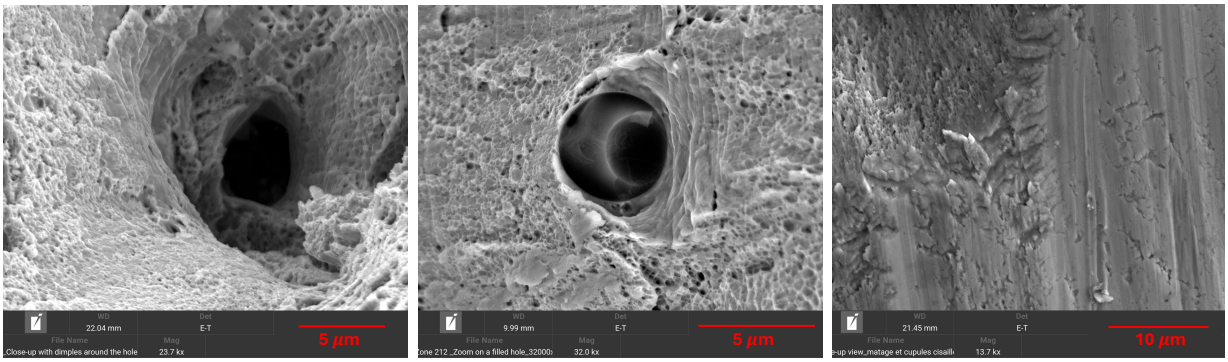

(a) (b) (c)

Figure 3.28: a) Porosity surrounded by dimples in TS5, b) Al oxide inclusion surrounded by dimples in TS1', c) Smearing area in TS3'.

Chapter 4

Discussions

4.1 Validation of 200 °C as optimal experimental preheating temperature

This study was based on the hypothesis that 200°C is the optimal preheating temperature for the base plate to obtain a near fully dense material with enhanced mechanical properties. Different types of tests and analysis were conducted and compared with available data from the literature to check the relevance of this temperature. The temperature of 200°C was proposed after testing 80°C, 300°C and 500°C in [60] which showed an area for improvement for temperatures between 80°C and 300°C. Several experiments performed in this study showed convincing results that tend to confirm the assumption that 200°C is the optimal preheating temperature.

First, no interruption was made when using the 200°C preheating temperature for printing both the larger blocks and the cubes. The other temperatures tested in previous research [60], always needed to interrupt the process for several cubes due to large defects already visible during the process. Using 200°C led in all cases to successful prints regardless of the power-velocity parameter combination. All four blocks with varying scanning strategies also showed very low surface roughness after analysis with the profilometer and no significant differences between the two strategies were observed. So, without considering the mechanical properties, 200°C seems to be the optimal preheating temperature to obtain a smoother surface on the top layer and to print parts without significant defects already visible during the process.

Another significant difference is the densities obtained with the pycnometer measurements when using a 200°C base plate. Even though the processing window used for the cubes was already optimised, only four cubes presented a relative density below the limit of 99.7%, as shown with red points in Fig.4.1. The porosity characterisation allowed the identification of the different regions on the PV processing map in Fig.4.1. The lack-of-fusion region is

mainly associated with low laser power even if samples 5 and 9 presented large porosities despite using a higher power and the lowest scan speed of 700 mm/s. The gas-porosity region is observed when using a low scan speed and high laser power meaning that a large amount of energy is delivered to the powder. The keyhole mode, characterised by a specific porosity shape, is not observed with the processing parameter ranges studied here and certainly requires a higher laser power. In terms of melt pool shape, the "keyhole regime" can be considered to correspond to the gas-porosity region [53]. At least six samples are considered in the optimal processing window based on their density and internal porosity quantification. This region on the PV map corresponds to the samples using high scan speeds and a quite high laser power. This corresponds to a moderate amount of energy and leads, under certain configurations, to VED similar to those used in the lack-of-fusion region namely for samples 5 and 9. These samples may have been damaged by spatters from sample 1, given that the three samples were aligned on the base plate during manufacturing but this point will be more discussed in the next section.

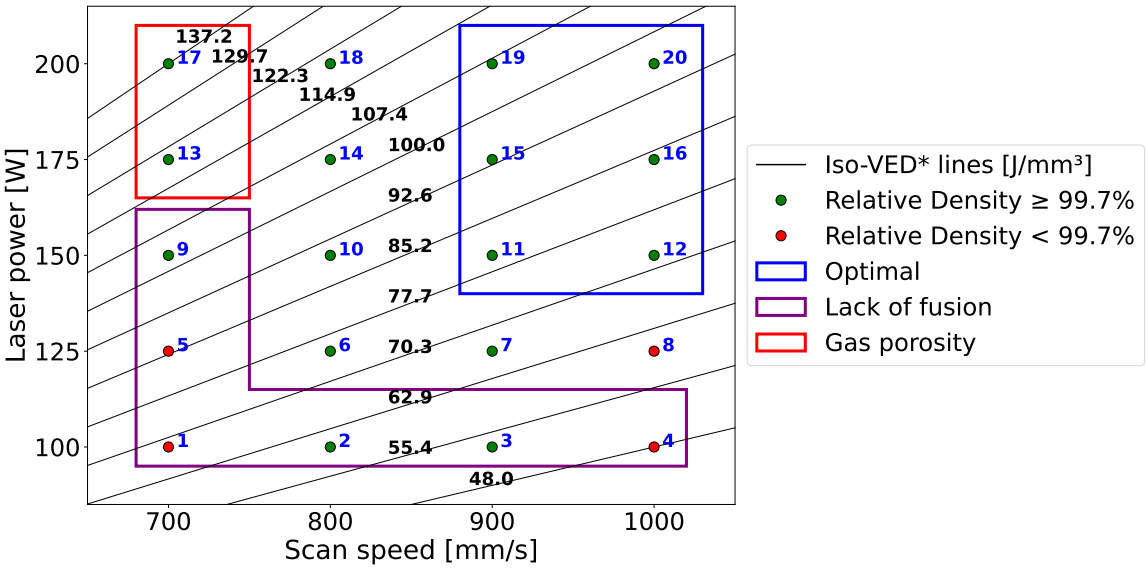

Figure 4.1: PV processing map of the twenty cubic samples with different porosity regions and optimal window, showing iso-VED* lines and highlighting the near fully dense samples with relative densities above 99.7% .

Moreover, the amount of oxide inclusions was reduced with the 200°C preheating temperature. The previous research [60] concluded that a trade-off exists with the preheating temperature between the removal of hot cracks and the formation of oxide inclusions both observed at high temperatures. With 200°C, no inclusion and no hot cracks were found in the cubes and this may correspond to the optimal temperature, which is high enough to avoid crack formation without promoting Si and Al oxide formation.

However, some limitations remain regarding the preheating temperature. As seen with the

macro- and micro-hardness on the block slices it is still difficult to ensure a homogeneous temperature inside the whole part. The blocks were printed with the same processing parameters as sample 19 and tested using the same methodology. Nevertheless, the macro- and micro-hardness results differ significantly from those of the samples and sometimes differ between the two sections from the same slice. In fact, thermal gradients are inevitable, the larger the part, the more difficult it is to have a similar thermal history everywhere in the part. A taller part leads to a greater gradient along the BD. A part extending further on the base plate can have a gradient in the XY plane because the platform is not necessarily uniformly heated as it is already shown in literature [69]. It is also difficult to know experimentally the true temperature at different locations inside the part during the printing process and therefore it makes it difficult to predict property variations linked to the temperature. This requires a hybrid study of the process i.e. an analysis of experimental and simulation data which can provide the thermal gradient due to the base plate as already tested in literature [7] with lower preheating temperature showing significant thermal gradients in the building direction. The temperature of the argon atmosphere also needs to be studied which is experimentally feasible using thermocouples.

Another aspect to take into consideration is the surrounding environment between the core of the part and its edges. The region in the core is mainly surrounded by solid material from the previous layer while the edges of the part are partly surrounded by unmelted powder, which does not have the same thermal properties as the solid part. Also, the first layers printed are subject to a larger number of thermal cycles due to laser passes on subsequent layers. The interlayer times (ILT), which are significantly different between the blocks and the cubes, may have an impact on the relative density and the crack density as reported in [26] which impacts the material properties. Another observation supporting the temperature difference between pieces of different sizes is the presence of oxides in the tensile specimens. This suggests that the temperature inside the larger parts was not uniform since 200°C should prevent their formation as seen with the cubes.

4.2 Impact of VED on material properties

VED was largely used to compare the samples during the different kinds of tests. The most significant result obtained when considering VED as the varying parameter was the melt pool morphology. It was seen in the last layer that the melt pool depth increases when VED increases which is consistent with most of the results reported in the literature [53] [27] [11]. However, simply combining multiple process parameters which vary into a single value such as VED seems to be an oversimplified approach to understand thermophysical processes involved in the melt pool. In fact, the scan speed and the laser power are inversely proportional and proportional to the VED respectively, but the MP depth is linearly proportional and negatively proportional to the power and scan vocality respectively [53]. However, the variation in laser power has larger impact on the MP geometry than the variation in scan speed, estimated to be approximately ten times greater [53].

This means that VED can be considered as the only parameter when hatch spacing and layer thickness are kept constant. The relative variation of the scan velocity must be small to not affect the VED more then it affects the MP geometry. Therefore, VED has an indirect impact on many other material properties through the shape variation of the MP. Indeed, several variations studied as a function of the VED are actually a consequence of the MP depth variations [35].

The first correlation linked to MP depth is the variation in the nano-hardness near the top layer. The nano-hardness tests, imposing an indentation depth of 500 nm, showed a gradient oriented in the opposite direction of the BD and the hardness starts to increase further below the top layer when using a higher VED. When the last layer is printed, the MP remelts completely several layers below given that the MPs have a depth of at least 80 μm for the samples studied and the theoretical layer thickness spread by the recoater is only 30 μm. The boundaries of the MP, with possible hardness variations in the heat-affected zone, are not observable with the too large indentation size used. However, the interior of the MP is remelted while the region just below the new MP, is locally heated, and then an annealing effect and the formation of MC carbide might be observed in the previous layer as described in [26]. Also, higher VED leads to a larger remelting zone and to fewer and smaller MC carbide at melt pool boundaries [26]. The hardness is then higher just below the last one or two layers which are the only layers not reheated by subsequent melt pool. This explains why the hardness remains lower on a larger part when using higher VED.

The second important variation studied with the VED was the grain morphology. It was seen that grains clearly follow the MP boundaries forming fan-shaped grains and leading to a more compact structure when VED increases. Since the MPs are larger at higher VED and the temperature also increases, the cooling rates must be lower, leading to larger grains. However, the higher VED also increases the thermal convection or Marangoni convection which decreases the thermal gradient. This increases the cooling rate at the MP boundaries which increases grain nucleation and leads to smaller and more equiaxed grains [35]. So, the increase in VED involves two competing effects, first, it decreases the thermal gradient and therefore decrease grain size by mitigating the epitaxial growth and the second effect is the increase in temperature which increases grain size [35]. The results obtained suggest that in the range of VED* studied here, a transition from columnar to equiaxed grains occurs with an intermediate fan-shaped morphology [35]. From 72.01 J/mm^3 to 80.01 J/mm^3 the grain size decreases due to the mitigation of the columnar grain, the first effect prevails. Then, above 80.01 J/mm^3 when the epitaxial growth leading to columnar grain is completely inhibited, the grains become larger to reach a more equiaxed morphology.

In addition, even if no mechanical tests were performed to compare the different VED, in theory the grain size variation should inevitably have an impact on the mechanical properties according to the Hall-Petch law. The finer grains and their more equiaxed structure may also increase the Young's Modulus of the material to reach the values obtained with

CM [2].

As can be seen in Fig.4.1 the same iso-VED* line can pass through several zones. Sample 1 with the largest porosities has a VED* very close to the VED* of sample 12 which is considered an optimal configuration. So, the amount of energy represented by VED* is more related to the melt pool size and all the consequences that entail on the other properties listed above. Only for specific applications as it is the case for porosity characterisation it is interesting to know how the energy is provided. The same amount of energy does not have the same impact if it is delivered abruptly or smoothly. But for most applications a strong correlation is observed with VED, such as MP geometry which impacts grain size and morphology, which then affect the mechanical properties.

Since the processing window used in this work was already optimised leading to a smaller VED* range and highly dense samples, no specific trend was identified between VED (or VED*) and the relative density. If a wider VED range is used, a parabolic trend can be clearly identified with an optimal density between the lack-of-fusion mode at low VED and the keyhole mode/regime at high VED [72]. However, a real limitation of the VED is observable with the variation in macro- and micro-hardness. The classical VED cannot explain the variation in hardness and the modified VED* which takes into account the preheating temperature, can lead to confusion in the interpretation of the results. It was seen with the samples that the hardness does not depend on laser power and scan velocity, this sets the limits of the classical VED. The results obtained at 200°C follow the trends highlighted in the previous study and thus confirm the observations made with the other preheating temperatures as shown in Fig.4.2. The drop in the macro-hardness happens before the 200°C and then might suggest that there exists a lower temperature before the drop while preserving the advantages of the 200°C discussed in the previous section. Therefore, the VED* can be used to explain these kinds of variations linked to the temperature but only if using similar processing parameters.

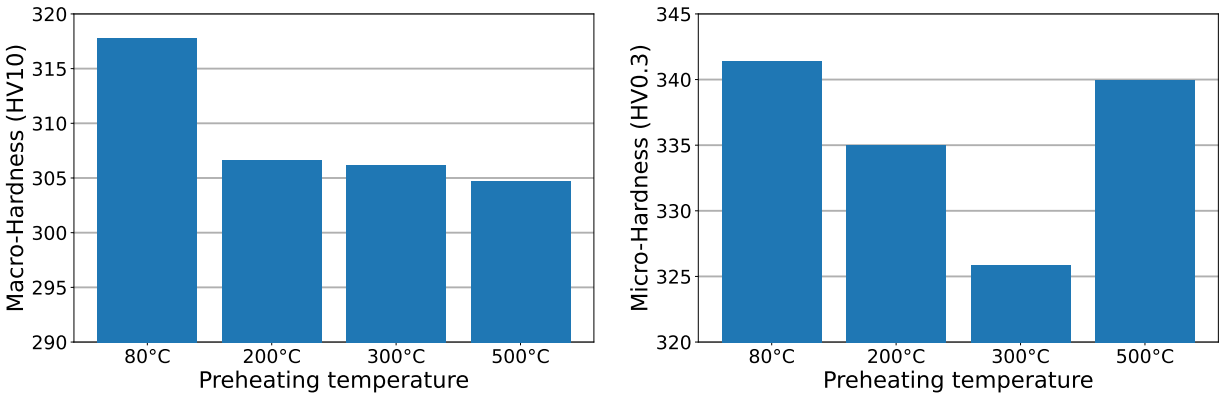

(a) (b)

Figure 4.2: Comparison of hardness between samples printed using a 200°C preheating temperature from this work and samples printed using 80°C, 300°C and 500°C from previous research [60] with a) macro-hardness HV10 and b) micro-hardness HV0.3.

4.3 Impact of scanning strategy on microstructure and mechanical properties

The two scanning strategies used, 90° and 67°, are the two most commonly used in literature. Using 90° is the most intuitive strategy, since 0° rotation leads to several internal and external defects [75]. The 67° strategy is also well documented since it makes a very low orientation repetition between layers. In this work, no significant variation could be observed between the scanning strategies for the surface roughness. Then, both macro- and micro-hardness also showed similar results between the strategies. The two scales do not depend on the exact same properties, macro-hardness is mainly affected by the cellular structure and the residual stresses whereas the micro-hardness depends on the dislocation density [60]. So, the scanning strategy does not seem to affect these properties at least with the processing parameters used. It is well known that the scanning strategy allows to avoid edge effects and reduces internal porosity [75] but the processing parameters used here mitigate these defects regardless of the 90° or 67° strategy. Indeed, the other printing parameters being already optimised, the potential improvement that the scanning strategy can provide is therefore limited.

However, the tensile tests showed a clear difference in mechanical properties between the two scanning strategies. The resistance of the material is clearly enhanced when using the 67° strategy. The yield strength and the ultimate tensile strength were higher than results obtained using the 90° strategy. This also led to satisfactory values when compared with the literature [52] [12] using other processing parameters which also confirms the choice of the optimal processing window and preheating temperature. The most significant difference lies in the Young's modulus results. The 67° strategy led to values close to those obtained with the conventional method while the 90° strategy was much lower. The important characteristics of the material on which the mechanical properties depend is the grain size, morphology, and orientation. The grain analysis by EBSD showed a similar microstructure with the two strategies but highlights that the 67° strategy led to the formation of new grains which surround the other grains. Following the Hall-Petch law, this might mitigate the dislocation motion since the average grain size is reduced. These grains formed at the boundaries of the "primary" grains may be due to a higher thermal gradient at the MP boundaries. Since the grains follow the MP and the cooling rate is higher and the growth rate is lower at the MP boundaries, the ratio G/R decreases at the MP centre, leading to cellular structure near the MP boundary and to columnar micro-structure inside the MP [26]. This difference of solidification mechanism between the centre and the boundaries of the MPs may lead to the formation of a border grain. This does not happen with the 90° strategy because of the high orientation repetition between layer and the heat accumulation involved. Another aspect that has not yet been discussed is the dislocation density. The Kernel Average Misorientation (KAM) obtained by EBSD analysis, shown in Fig.A.8 in Appendix ix, gives an indication on the dislocation density more specifically on geometrically necessary dislocation (GND) density. The slice using 67° rotation angle has much higher dislocation density than the 90° slice and the dislocations seem to be localised

at the bottom of the grains for both scanning strategies. This higher dislocation density when using 67° scanning strategy also play a significant role in the enhancement of the resistance of the material [37].

Nevertheless, even if the grain structure is not the same and the mechanical properties are impacted, the failure mode remains the same between the two scanning strategies. The same ductile failure mode is observed with very fine dimple structures in the fracture section, showing a similar failure mechanism, with a failure initiation at the centre of the gauge section.

Chapter 5

Conclusions and perspectives

5.1 Conclusions

This work focusing on as-built Inconel 718 obtained by the LPBF method, allowed to highlight many phenomena from the manufacturing process that influence the material properties. An optimisation of the processing parameters was set and consequently showed the properties that can be achieved with as-built material. So, several conclusions can be drawn and are presented in the following.

First, the 200°C preheating temperature is indeed the optimum temperature for enhancing the properties of the material but larger as-built parts require absolutely a heat treatment to homogenise the properties throughout the material. The 200°C preheating temperature allows to obtain a near fully dense material over a wide range of processing parameters with an optimal window between 900 and 1000 mm/s for scan speed and 150 and 200 W for laser power. Heating the base plate to 200°C also prevents both crack formation and oxide inclusions enhancing the as-built material properties.

This study also shows the evolution of grain size and morphology with VED* varying in a restricted range since the processing window was optimised. In agreement with the literature [35] the increase in VED* tends first to decrease grain size by inhibiting the columnar morphology and then to increase grain size due to the higher temperature induced. In the range studied the grains remain with a fan-shaped morphology with a minimum size obtained at 80.01 μm. So the VED* which takes into account the base plate temperature is a good proxy for energy input. However, all material properties do not depend on the VED* such as the macro- and micro-hardness which confirms that they only depend on the preheating temperature.

Finally, the 67° scanning strategy did not show clear differences in most of the tests performed, such as roughness and hardness analyses, since these properties had already been enhanced by the other processing parameters used. However, a large variation was ob-

served in tensile tests. They showed that the 67° scanning strategy provides higher yield strength, ultimate tensile strength and Young's modulus, close to the values obtained with CM. This variation in the mechanical properties is attributed to two factors. First, the microstructure, using the 67° strategy, showed new grains surrounding the primary grains, leading to a smaller average grain size. Secondly, the higher dislocation density also led to an increase in the yield strength.

5.2 Perspectives

This study covered a wide range of tests which enable to draw several conclusions exposed above. The results reveal some correlations between the processing parameters and the observations but not in all cases. Therefore, several research avenues have been identified for further investigation or to improve the current results. These experiments can also be carried out to confirm certain uncertainties about the interpretations of the results presented here. The following list sets out the various research areas identified:

- The optimal processing window could be further optimised, large gaps were used between the different scanning velocities and laser power. Therefore, the optimal window can be narrowed and its boundaries can be more precisely defined. In the same vein, different preheating temperatures around 200°C must also be analysed. The other temperatures analysed in the previous research were 80 and 300°C which are quite far from the 200°C identified as the optimal temperature in this study.
- The twenty samples used to study the density and the microstructure were printed with varying scan speeds and laser powers but the scanning strategy was the same for all samples (90° rotation). It could be interesting to conduct an analysis of the impact of this parameter on the density.
- A second parameter to investigate concerning sample densities is the surfaces analysed. The density estimated using the OM might need a scale factor, the surfaces considered given in the appendix iii, may be too small to be truly representative of the material even if they already provide quite satisfactory results in agreement with the pycnometer measurements.
- Using larger tensile specimens with standardised dimensions to get a larger effective section would allow to be more representative of the mechanical properties. It is also possible to keep the small specimens but printed at different positions along the argon flow to check its effect on the material.
- Machining tensile specimens with different orientations within the blocks to compare the variation in the mechanical properties. In addition, a characterisation of the grain morphologies in the XY plane to obtain a better understanding of the 3D shape of the grains and the impact on the mechanical properties.
- The hardness analysis with the nano-indentation can be performed at a smaller scale,

at the scale of a cell to compare the centre and the cell boundaries and the effect of the different segregations present. An intermediate scale can also be used to obtain a better resolution and allow the characterisation of the MP more precisely, especially the identification of the Heat-Affected Zone (HAZ).

– To identify potential precipitates, Differential Thermal Analysis (DTA) can be performed. It is possible to compare the unused powder and powder already preheated at different temperatures and also to take samples from the two other blocks printed using 90° and 67° scanning strategies.

– A more in-depth analysis of the potential scale factor identified with the macro- and micro-hardness differences between the cubic samples and the larger blocks needs to be performed. Other properties, such as density and porosity, may also be impacted.

Appendices

i

Sample	Measured values [g/cm^3]					Average [g/cm^3]
1	8.1303	8.1306	8.1338	8.1309	8.1294	8.1310
2	8.1646	8.1711	8.1682	8.1720	8.1656	8.1683
3	8.1781	8.1821	8.1660	8.1769	8.1694	8.1745
4	8.1548	8.1676	8.1566	8.1537	8.1685	8.1602
5	8.1653	8.1562	8.1543	8.1602	8.1532	8.1578
6	8.1765	8.1785	8.1693	8.1647	8.1719	8.1722
7	8.1623	8.1698	8.1775	8.1685	8.1674	8.1691
8	8.1116	8.1151	8.0979	8.1107	8.1167	8.1104
9	8.1696	8.1682	8.1726	8.1690	8.1593	8.1677
10	8.1864	8.1829	8.1943	8.1902	8.1831	8.1874
11	8.1741	8.1777	8.1812	8.1867	8.1838	8.1807
12	8.1863	8.1860	8.1899	8.1818	8.1795	8.1847
13	8.1811	8.1821	8.1764	8.1727	8.1707	8.1766
14	8.1798	8.1737	8.1785	8.1878	8.1680	8.1776
15	8.1829	8.1592	8.1830	8.1730	8.1746	8.1745
16	8.1815	8.1715	8.1714	8.1617	8.1640	8.1696
17	8.1764	8.1731	8.1688	8.1627	8.1700	8.1702
18	8.1738	8.2026	8.1874	8.1822	8.1918	8.1876
19	8.2014	8.1918	8.1872	8.1797	8.1868	8.1894
20	8.1808	8.1879	8.1914	8.1816	8.1804	8.1844

Table A.1: Iterations of density measurement with pycnometer and their averages for each cubic sample.

ii

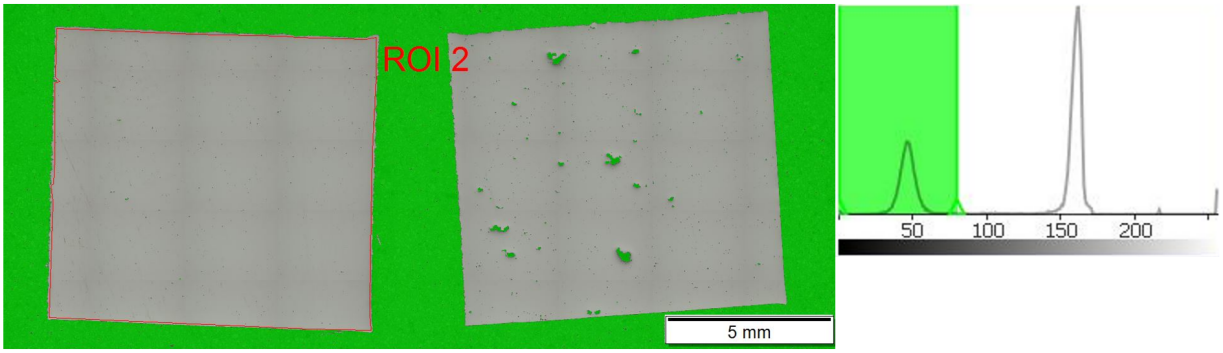

(a) Low threshold.

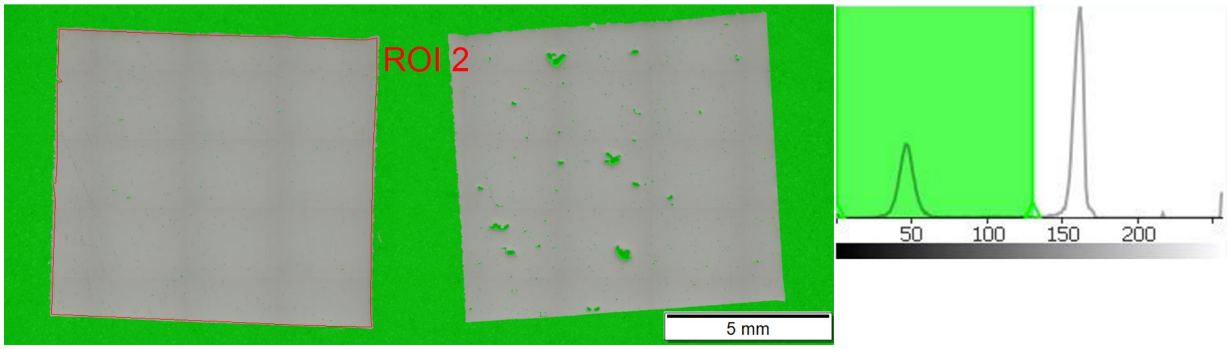

(b) High threshold.

Figure A.1: Threshold used for porosity percentage estimation with OM analysis, with sample 1 on the right and sample 2 on the left.

iii

Sample	Area of Interest [mm^2]
1	86.489
2	87.454
3	85.514
4	86.068
5	84.302
6	86.210
7	84.790
8	85.251
9	85.845
10	87.273
11	85.958
12	86.426
13	87.032
14	87.111
15	87.559
16	87.542
17	86.813
18	86.537
19	88.523
20	88.120
Mean value	**86,483**
Standard deviation	1.123

Table A.2: Areas of interest measured using Image J for each sample for porosity percentage estimation with OM.

iv

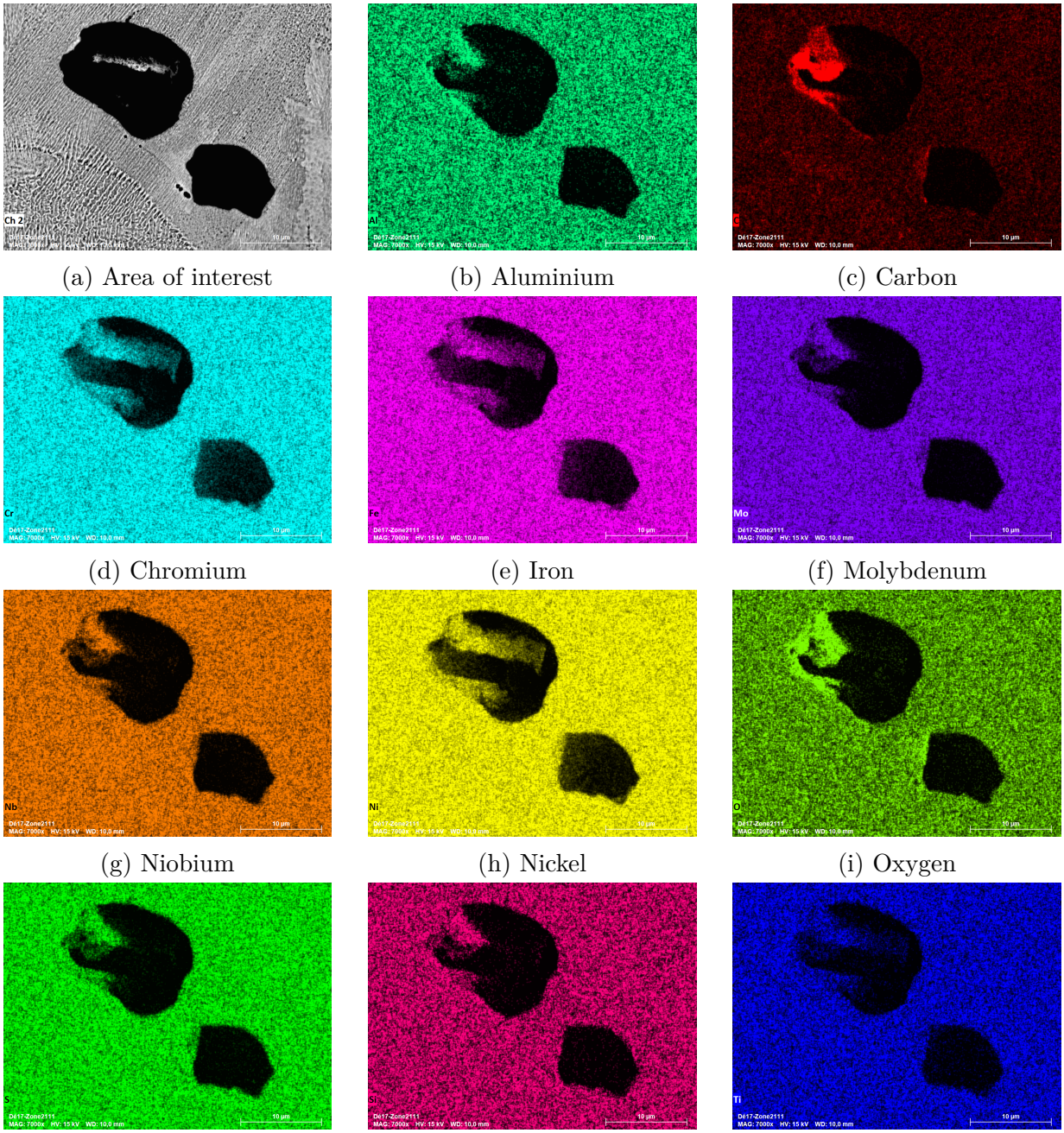

(a) Area of interest (b) Aluminium (c) Carbon

(d) Chromium (e) Iron (f) Molybdenum

(g) Niobium (h) Nickel (i) Oxygen

(j) Sulfur (k) silicium (l) Titanium

Figure A.2: EDX mapping of porosity on sample 17 (P=200 W, V=700 mm/s).

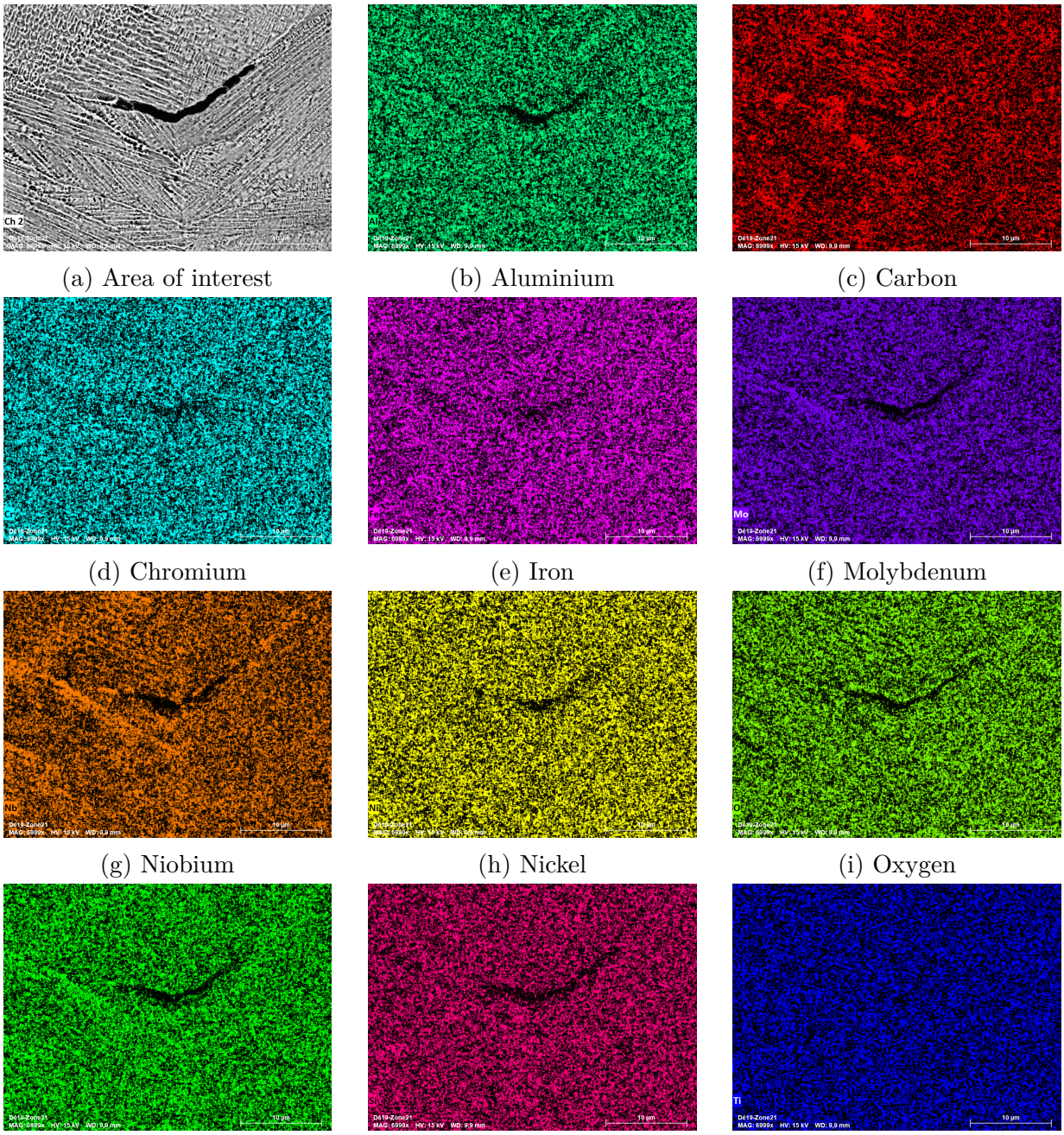

(a) Area of interest (b) Aluminium (c) Carbon

(d) Chromium (e) Iron (f) Molybdenum

(g) Niobium (h) Nickel (i) Oxygen

(j) Sulfur (k) Silicium (l) Titanium

Figure A.3: EDX mapping of porosity on sample 17 (P=200 W, V=700 mm/s).

V

N°	Macro-Hardness HV10		Micro-Hardness HV0.3	
	MV	**SD**	**MV**	**SD**
1	310.6	17.8	332.2	9.9
2	304.5	7.8	332.9	8.3
3	305.8	4.6	330.7	6.8
4	306.4	5.3	332.2	9.5
5	309.9	10.0	331.4	8.5
6	304.5	7.1	340.0	7.1
7	301.9	8.1	340.6	5.2
8	308.1	6.5	333.3	9.2
9	304.1	4.2	337.1	7.7
10	305.6	3.0	336.4	5.9
11	305.5	6.5	334.9	9.5
12	307.8	8.1	333.4	8.3
13	309.3	6.0	337.4	8.7
14	307.1	2.7	335.5	9.6
15	303.4	7.1	332.9	10.1
16	307.8	4.6	339.0	7.8
17	305.7	6.5	330.9	10.4
18	307.8	4.3	333.0	8.9
19	306.2	5.7	336.0	9.4
20	309.8	7.1	340.3	8.6
Average	**306.6**	-	**335.0**	-

Table A.3: Mean Values (MV) and Standard Deviation (SD) of macro- and micro-hardness of each sample.

vi

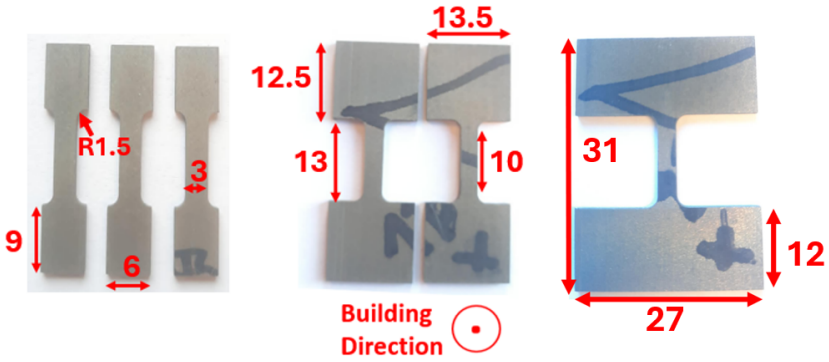

Figure A.4: Precedent tensile specimen designs leading to unsuccessful results with same gauge dimensions and the same total length, with dimensions in mm.

vii

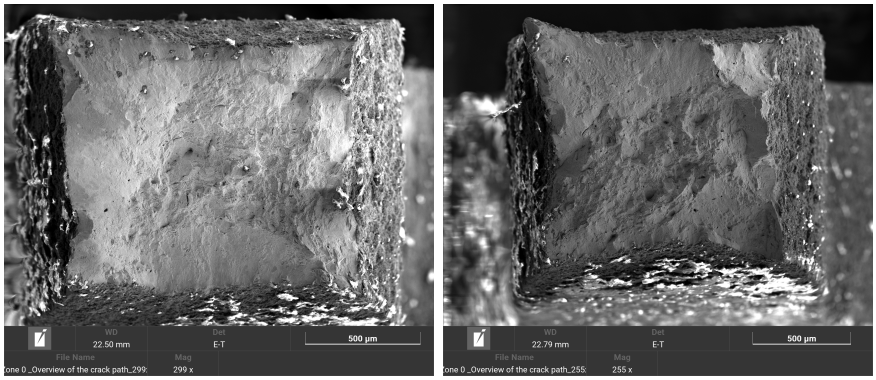

(a) TS1 (b) TS2

(c) TS3 (d) TS5

Figure A.5: Fracture section of tensile specimens printed using a 90° scanning strategy.

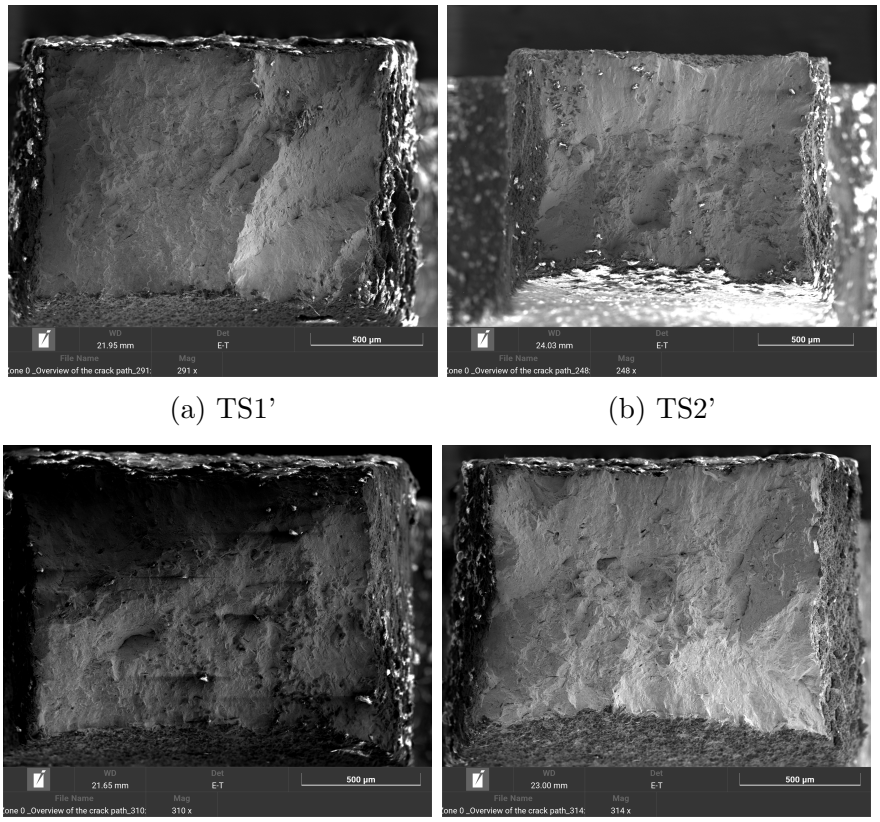

(a) TS1’ (b) TS2’

(c) TS3’ (d) TS5’

Figure A.6: Fracture section of tensile specimens printed using a 67° scanning strategy.

viii

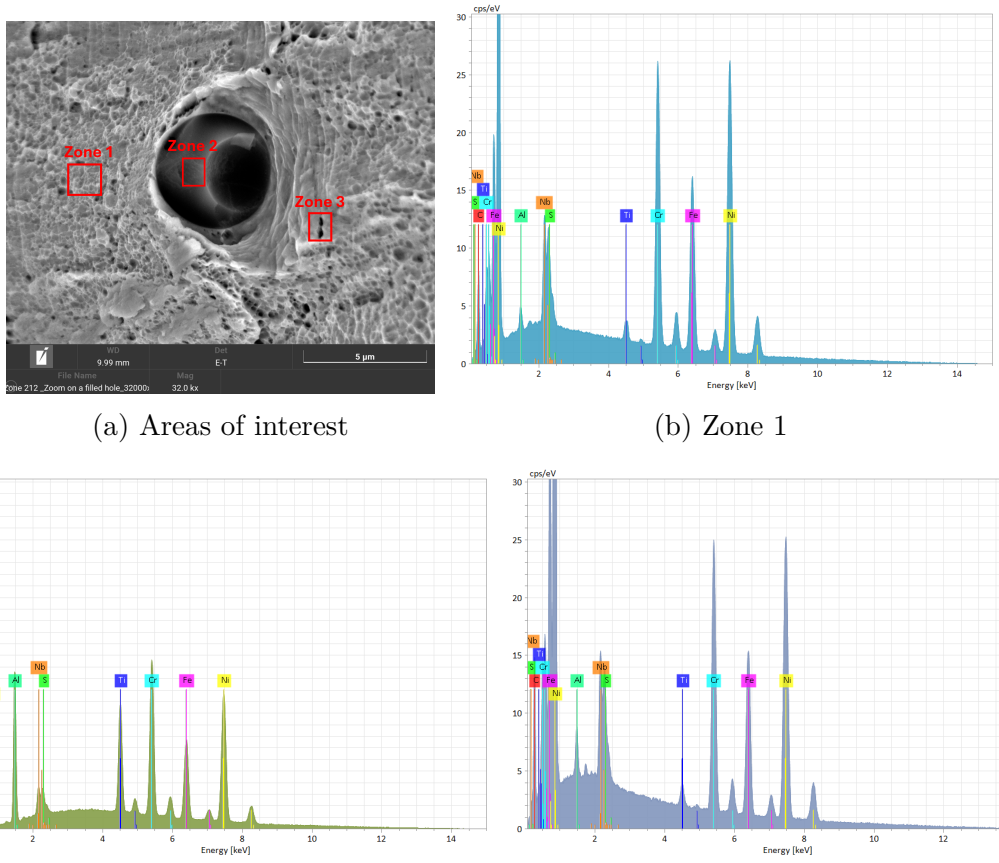

(a) Areas of interest

(b) Zone 1

(c) Zone 2

(d) Zone 3

Figure A.7: Composition spectrum obtained by EDX analyses inside and around oxide inclusion on fracture section of TS1'.

ix

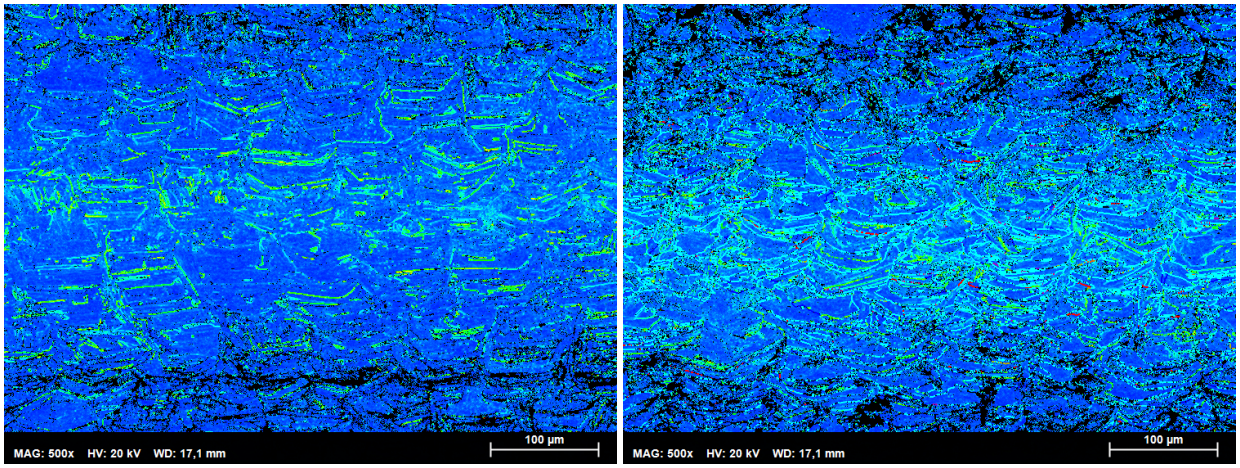

(a) (b)

Figure A.8: Kernel average misorientation (KAM) of a) slice 1 and b) slice 1'.

Bibliography

[1] Ahmed Abdelgawad, Imad Barsoum, and Rashid K. Abu Al-Rub. Influence of scanning patterns on residual stresses and mechanical properties in lpbf-manufactured cellular structures. *Materials and Design*, 258:114607, 2025.

[2] Michele Abruzzo, Giuseppe Macoretta, Bernardo Disma Monelli, and Luca Romoli. Impact of process parameters on the dynamic behavior of inconel 718 fabricated via laser powder bed fusion. *The International Journal of Advanced Manufacturing Technology*, 132:3655–3669, 2024.

[3] Aconity3D. Aconitymini machine description. https://aconity3d.com/products/aconity-mini/. Accessed February 16, 2026.

[4] Ankur K. Agrawal, Behzad Rankouhi, and Dan J. Thoma. Predictive process mapping for laser powder bed fusion: A review of existing analytical solutions. *Current Opinion in Solid State and Materials Science*, 26:101024, 2022.

[5] AXT. Aconitymini. https://www.axt.com.au/products/aconitymini/. Accessed February 16, 2026.

[6] Emilio Bassini, Giulio Marchese, and Alberta Aversa. Tailoring of the microstructure of laser powder bed fused inconel 718 using solution annealing and aging treatments. *Metals*, 11:921, 2021.

[7] Benjamin D. Bevans, Antonio Carrington, Alex Riensch, Adriane Tenequer, Christopher Barrett, Harold (Scott) Halliday, Raghavan Srinivasan, Kevin D. Cole, and Prahalada Rao. Digital twins for rapid in-situ qualification of part quality in laser powder bed fusion additive manufacturing. *Additive Manufacturing*, 93:104415, 2024.

[8] Bruker. Hysitron ti 980 nanoindenter. https://www.bruker.com/fr/products-and-solutions/test-and-measurement/nanomechanical-test-systems/hysitron-ti-980-nanoindenter.html. Accessed April 21, 2026.

[9] Guillian Bryndza, Jérôme Tchoufang Tchuindjang, Fan Chen, Anne Marie Habraken, Héctor Sepúlveda, Víctor Tuninetti, Anne Mertens, and Laurent Duchêne. Review of the microstructural impact on creep mechanisms and performance for laser powder bed fusion inconel 718. *Materials*, 18:276, 2025.

[10] CAE. Bx60m. https://caeonline.com/buy/microscopes/olympus-bx60m/125750. Accessed February 23, 2026.

[11] Qian Chen, Yunhao Zhao, Seth Strayer, Yufan Zhao, Kenta Aoyagi, Yuichiro Koizumi, Akihiko Chiba, Wei Xiong, and Albert C. To. Elucidating the effect of preheating temperature on melt pool morphology variation in inconel 718 laser powder bed fusion via simulation and experiment. *Additive Manufacturing*, 37:101642, 2021.

[12] Yixuan Chen, Weihao Wang, Yao Ou, Hai Chang, Yingna Wu, Rui Yang, Zirong Zhai, Kefei Li, and Liyaowei Shen. Microstructure and mechanical property comparison of inconel alloys fabricated using micro and conventional laser powder bed fusion. *Materials & Design*, 237:112534, 2024.

[13] Conceptek. Principe de l'essai de dureté des métaux. https://conceptek.net/fr/techniques-de-base/materiaux/essais-et-controles/essai-de-durete, 2016. Accessed February 26, 2026.

[14] Kunjie Dai, Xing He, Decheng Kong, Reynier I. Revilla, Yucheng Ji, Tianle Liu, Wei Zhang, Anqing Fu, and Chaofang Dong. High-strength yet hydrogen embrittlement-resistant laser powder bed fusion inconel 718 alloy through heat treatment. *Corrosion Science*, 256:113208, 2025.

[15] demarcheiso17025. En apprendre un peu plus sur les essais de durete. https://www.demarcheiso17025.com/fiche034.html. Accessed February 26, 2026.

[16] Kim Do Kyung. Nanoindentation lecture 1 basic principle. *Department of Materials Science and Engineering KAIST*, n.d.

[17] ems benelux. Alicona - infinite focus g5. https://www.ems-benelux.com/produits/infinite-focus-g5. Accessed February 20, 2026.

[18] William E. Frazier. Metal additive manufacturing: A review. *Journal of Materials Engineering and Performance*, 23:1917–1928, 2014.

[19] Ian Gibson, David Rosen, and Brent Stucker. *Additive Manufacturing Technologies: 3D Printing, Rapid Prototyping, and Direct Digital Manufacturing*, pages 107–144. Springer, New York, second edition edition, 2015.

[20] gindumac. Charmilles robofil 310 erosion machine. `https://www.gindumac.com/product/charmilles-robofil-310`. Accessed March 4, 2026.

[21] Ozkan Gokcekaya, Takuya Ishimoto, Shinya Hibino, Jumpei Yasutomi, Takayuki Narushima, and Takayoshi Nakano. Unique crystallographic texture formation in inconel 718 by laser powder bed fusion and its effect on mechanical anisotropy. *Acta Materialia*, 212:116876, 2021.

[22] Konrad Gruber, Wojciech Stopyra, Karol Kobiela, Philipp Kohlwes, Jan Čapek, Efthymios Polatidis, and Ingomar Kelbassa. Achieving high strength and ductility in inconel 718: tailoring grain structure through micron-sized carbide additives in

pbf-lb/m additive manufacturing. *Virtual and Physical Prototyping*, 19(1):e2396064, 2024.

[23] Chan Guo, Junxia Lu, Xiaopeng Cheng, Shuai Huang, Tianyuan Wang, Yuefei Zhang, and Ze Zhang. Effect of recrystallization on strength and plasticity of lpbf inconel 718 superalloy. *Materials Today Communications*, 46:112775, 2025.

[24] Chuan Guo, Jingchen Wang, Yanmin Wang, Di Wang, Chaolin Tan, Haoqi Zhang, Peng Chen, Jinxing Sun, and Zeping Lv. Nickel-based superalloy matrix composites fabricated by laser additive manufacturing: A critical review of recent advances and overcoming challenges. *Journal of Alloys and Compounds*, 1048:185331, 2025.

[25] I-Ting Ho, Dhruv Tiparti, Zhuo Liu, and Sammy Tin. Insight to potential of tib2 and ceo2 inoculants on microstructural evolution in laser powder bed fusion processed superalloy in718. *Metallurgical and Materials Transactions A*, 55:261, 2024.

[26] Yong Hu, Hui-Bin Jia, Yong-Qi Hu, Cheng Chu, Xu Zhang, Li-Hua Wang, and Dong Zhang. Thermal cycling on microstructure and mechanical properties of laser powder bed fusion manufactured IN738LC alloy. *RARE METALS*, 43:6649–6672, 2024.

[27] Thinh Huynh, Abhishek Mehta, Kevin Graydon, Jeongmin Woo, Sharon Park, Holden Hyer, Le Zhou, D. Devin Imholte, Nicolas E. Woolstenhuime, Daniel M. Wachs, and Yongho Sohn. Microstructural development in inconel 718 nickel-based superalloy additively manufactured by laser powder bed fusion. *Metallography, Microstructure, and Analysis*, 11:88–107, 2022.

[28] Toshi-Taka Ikeshoji, Yusuke Tachibana, Makiko Yonehara, and Hideki Kyogoku. Laser beam powder bed fusion of inconel 718 under high power and scanning speed. *Journal of Advanced Mechanical Design, Systems, and Manufacturing*, 17(6), 2023.

[29] innovatest. Falcon 500g2. https://www.innovatest-europe.com/products/falcon-500g2/. Accessed February 20, 2026.

[30] Muhammad Ahmad Iqbal, Kateřina Skotnicová, Anum Shafiq, and Tabassum Naz Sindhu. Inconel alloys: A comprehensive review of properties and advanced manufacturing techniques. *International Journal of Thermofluids*, 29:101394, 2025.

[31] Junmyoung Jang, Donghyun Van, and Seung Hwan Lee. Precipitation kinetics of secondary phases induced by heat accumulation in the deposit of inconel 718. *Additive Manufacturing*, 55:102831, 2022.

[32] Victoria Kaban, Christoph Leyens, and Julia Kristin Hufenbach. Non-equilibrium solidification of undercooled inconel 718. *Journal of Alloys and Compounds*, 1002:175205, 2024.

[33] Galina Kasperovich, Joachim Gussone, Guillermo Requena, Norbert Schell, Andreas Stark, and Jan Haubrich. Tailoring the strength of inconel 718: Insights into lpbf parameters and heat treatment synergy. *Materials & Design*, 250:113627, 2025.

[34] Yousub Lee, Mark Nordin, Sudarsanam Suresh Babu, and Dave F. Farson. Effect of fluid convection on dendrite arm spacing in laser deposition. *Metallurgical and Materials Transactions B*, 45:1520–1529, 2014.

[35] Xiaofei Li, Huanhuan Cheng, Chengcheng Shi, Rui Liu, Ruyue Wang, and Chuan Yang. Achieving equiaxed transition and excellent mechanical properties in a novel near-β titanium alloy by regulating the volume energy density of selective laser melting. *Materials*, 17:2631, 2024.

[36] Linqing Liu, Di Wang, Yongqiang Yang, Zhi Wang, Zeyu Qian, Shibiao Wu, Jinrong Tang, Changjun Han, and Chaolin Tan. Effect of scanning strategies on the microstructure and mechanical properties of inconel 718 alloy fabricated by laser powder bed fusion. *Advanced Engineering Materials*, 25:2200492, 2023.

[37] Duy Nghia Luu, Jiazhao Huang, YanHan Liew, Andrew Nathaniels, Joel Yi Jin Goh, and Jason Jyi Sheuan Ten. Tailoring mechanical properties and corrosion resistance via recrystallization-induced microstructural control in lpbf-fabricated in718. *Materials & Design*, 262:115426, 2026.

[38] J.F.S. Markanday, M.A. Carpenter, R.P. Thompson, N.G. Jones, K.A. Christofidou, S.M. Fairclough, C.P. Heason, and H.J. Stone. Effect of nbc inoculants on the elastic properties and microstructure of additively manufactured in718. *Materialia*, 27:101701, 2023.

[39] Metkon. Micracut 202 metallographic automatic high-speed precision cutter. https://www.metkon.com/products/cutting/cutting-equipment/precision-cutting-equipment/micracut-202/. Accessed March 6, 2026.

[40] Micromeritics. Pycnométrie des gaz. https://micromeritics.com/fr/density/. Accessed February 19, 2026.

[41] Tuan D. Ngo, Alireza Kashani, Gabriele Imbalzano, Kate T.Q. Nguyen, and David Hui. Additive manufacturing (3d printing): A review of materials, methods, applications and challenges. *Composites Part B*, 143:172–196, 2018.

[42] Mang Ni, Chao Chen, Ruifeng Xu, Seyed Reza Elmi Hosseini, Ruidi Li, Xiaoyong Zhang, and Kechao Zhou. Microstructure and mechanical properties of additive manufactured inconel 718 alloy strengthened by oxide dispersion with 0.3 wt% sc addition. *Journal of Alloys and Compounds*, 918:165763, 2022.

[43] Thaviti Naidu Palleda, Santhosh Banoth, Mikiko Tanaka, Hideyuki Murakami, and Koji Kakehi. The role of yttrium micro-alloying on microstructure evolution and high-temperature mechanical properties of additively manufactured inconel 718. *Materials & Design*, 225:111567, 2023.

[44] Ajay Polasani and Vikram V. Dabhade. Heat treatments of inconel 718 nickel-based superalloy: A review. *Metals and Materials International*, 31:1204–1231, 2025.

[45] S. Pramod and D. Kesavan. Melting modes of laser powder bed fusion (l-pbf) processed in718 alloy: Prediction and experimental analysis. *Advances in Industrial and Manufacturing Engineering*, 6:100106, 2023.

[46] radaco. Micromeritics: Accupyc ii 1340. https://www.radaco.com/produit/micromeritics-accupyc-ii-1340. Accessed February 19, 2026.

[47] Lakshmi Ramineni, Abdalmageed Almotari, Majed Ali, Anwar Algamal, and Ala Qattawi. Residual stress mapping in heat-assisted additive manufacturing of in 718: An x-ray diffraction study. *Journal of Materials Engineering and Performance*, 33:4124–4135, 2024.

[48] Singaravelu Rajan Sabari, N.T.B.N. Koundinya, S.V.S. Narayana Murty, B.K. Nagesha, G.D. Janaki Ram, and Ravi Sankar Kottada. Understanding the role of microstructure on creep anisotropy in additively manufactured in718. *Materials Characterization*, 223:114935, 2025.

[49] Vikrant Saumitra. Microstructural evolution and precipitation kinetics of carbides in l-pbf processed inconel 718 during long-term homogenization. *Materials Today Communications*, 42:111192, 2025.

[50] Md Shahwaz, Prekshya Nath, and Indrani Sen. A critical review on the microstructure and mechanical properties correlation of additively manufactured nickel-based superalloys. *Journal of Alloys and Compounds*, 907:164530, 2022.

[51] Md Shahwaz, Prekshya Nath, and Indrani Sen. Recent advances in additive manufacturing technologies for ni-based inconel superalloys - a comprehensive review. *Journal of Alloys and Compounds*, 1010:177654, 2025.

[52] Sunny Sharma, Karthik Palaniappan, Vagish D. Mishra, Srikanth Vedantam, H. Murthy, and Balkrishna C. Rao. Mechanical characterization of near-isotropic inconel 718 fabricated by laser powder-bed fusion. *Metallurgical and Materials Transactions A*, 54:270–285, 2023.

[53] Abhishek Shrivastava, S. Anand Kumar, and Samrat Rao. Multi-scale modelling for optimization of process parameters of laser powder bed fusion processed inconel 718 surrogate part. *Engineering Failure Analysis*, 155:107713, 2024.

[54] sigma. Citopress mounting press. https://www.sep.ae/product/citopress-mounting-press. Accessed February 23, 2026.

[55] Struers. Tegramin. https://webshop.struers.com/en/products/grinding-and-polishing/grinding-and-polishing-equipment/tegramin. Accessed February 23, 2026.

[56] Ching-Hua Su, Kristina Rodgers, Poshou Chen, Ellen Rabenberg, and Sridhar Gorti. Design, processing, and assessment of additive manufacturing by laser powder bed fusion: A case study on inconel 718 alloy. *Journal of Alloys and Compounds*, 902:163735, 2022.

[57] Nedim Sunay, Mert Kaya, Mustafa Safa Yılmaz, and Yusuf Kaynak. Effects of heat treatment on surface integrity and wear performance of inconel 718 alloy fabricated by laser powder bed fusion process additive manufacturing under different laser power and scanning speed parameters. *Journal of the Brazilian Society of Mechanical Sciences and Engineering*, 45:430, 2023.

[58] Vishwas Swarnkar, Gurunathan Saravana Kumar, and Murugaiyan Amirthalingam. Does base plate preheat temperature and gas flow rate distribution significantly affect the bead morphology in single-track experiments fabricated using lpbf? In R. Gnanaamoorthy et al., editors, *Advanced Materials and Innovative Processing*, volume 84 of *Springer Proceedings in Materials*. Springer, 2025.

[59] Emre Taşcioğlu, Yusuf Kaynak, Safian Sharif, Fatih Pıtır, and Mohd Azlan Suhaimi. Machining-induced surface integrity of inconel 718 alloy fabricated by powder bed fusion additive manufacturing under various laser processing parameters. *Machining Science and Technology*, 26(1):49–71, 2022.

[60] Jérôme Tchoufang Tchuindjang, Edoardo Fassinato, Olivier Dedry, and Anne Mertens. Effect of preheating temperature on the optimal processing windows of inconel 718 processed by laser powder bed fusion. In *ESAFORM 2026*, 2026.

[61] Emre Tekoglu, Alexander D. O'Brien, Jian Liu, Baoming Wang, Sina Kavak, Yong Zhang, So Yeon Kim, Shitong Wang, Duygu Agaogullari, Wen Chen, A. John Hart, and Ju Li. Strengthening additively manufactured inconel 718 through in-situ formation of nanocarbides and silicides. *Additive Manufacturing*, 67:103478, 2023.

[62] Tescan. Ultra-high resolution sem for confident, multimodal imaging. https://tescan.com/product-portfolio/sem/clara. Accessed February 27, 2026.

[63] usine nouvelle. Machine d'usinage par électro-érosion à fil à commande numérique charmilles - type : Robofil 310. https://www.usinenouvelle.com/expo/machine-d-usinage-par-electro-erosion-p176900.html. Accessed March 3, 2026.

[64] usinenouvelle. Système de mesure 3d optique infinitefocus g5. https://www.usinenouvelle.com/expo/systeme-de-mesure-3d-optique-infinitefo-p133849885.html. Accessed February 20, 2026.

[65] Huihui Wang, Qianying Guo, Chong Li, Lei Cui, Haining Yao, and Yongchang Liu. Effect of homogenization treatment on the microstructure and creep properties of additively manufactured inconel 718 alloy modified by Ti_2 AlC inoculants. *Journal of Alloys and Compounds*, 1017:179062, 2025.

[66] Lilin Wang, Fan Yang, Tianhong Gui, Weiming Huang, Xin Lin, and Weidong Huang. Improved creep properties of inconel 718 fabricated by selective laser melting from boron-phosphorus interaction. *Materials Research Letters*, 12(9):661–667, 2024.

[67] Yi Wang, Hongmei Zhang, Hairong Bian, Jialong Du, Mingwei Lu, Kaiyu Luo, and Jinzhong Lu. Tailoring microstructure and mechanical properties of in738lc fabricated

by laser powder bed fusion through processing parameter optimization. *Optics and Laser Technology*, 188:112887, 2025.

[68] Yurong Wang, Buwei Xiao, Xiaoyu Liang, Pengcheng Lv, Qingze Liu, Jun Zhou, Huabei Peng, and Feng Lin. Highly controllable material properties of inconel 718 fabricated by a novel liquid metal-assisted laser powder bed fusion. *Additive Manufacturing*, 109:104868, 2025.

[69] M. Yesim Yalcin, Bora Derin, and Eda Aydogan. Development and additive manufacturing of oxide dispersion strengthened inconel 718: Thermochemical and experimental studies. *Journal of Alloys and Compounds*, 914:165193, 2022.

[70] Huihui Yang, Zemin Wang, Hongze Wang, Yi Wu, and Haowei Wang. Microstructure, mechanical property and heat treatment schedule of the inconel 718 manufactured by low and high power laser powder bed fusion. *Materials Science & Engineering A*, 863:144517, 2023.

[71] Jialiu Yang, Chuanwei Li, Yao Yuan, Yuwen Huang, Hao Zhang, Xudong Yang, and Jianfeng Gu. Nanoscale Y_2O_3 particle-derived mechanical properties improvement in in718 superalloy fabricated by powder bed fusion. *Materials Science and Engineering: A*, 944:148919, 2025.

[72] Tianyang Yue, Zhiyi Zou, Sheng Zhang, Haodong Liu, Qingyu Chen, Wei Wen, and Yong Zang. Effects of volumetric energy density on melting modes, printability, microstructures, and mechanical properties of laser powder bed fusion (l-pbf) printed pure nickel. *Materials Science & Engineering A*, 909:146871, 2024.

[73] Xiaoya Zhai, Liuchao Jin, and Jingchao Jiang. A survey of additive manufacturing reviews. *Materials Science in Additive Manufacturing*, 1(4):21, 2022.

[74] Liuwei Zheng, Leilei Shen, Yingzhi Wang, Hongxia Wang, Yakai Zhao, Upadrasta Ramamurty, and Jun Hu. Effect of the solutionizing temperature on the strength and hydrogen embrittlement resistance of the laser powder bed fused inconel 718 superalloy. *Corrosion Science*, 262:113642, 2026.

[75] Qiao Zhong, Kaiwen Wei, Taoyuan Ouyang, Xiangyou Li, and Xiaoyan Zeng. Effect of rotation angle on surface morphology, microstructure, and mechanical properties of inconel 718 alloy fabricated by high power laser powder bed fusion. *Journal of Materials Science & Technology*, 154:30–42, 2023.

[76] Longfei Zhou, Jenna Miller, Jeremiah Vezza, Maksim Mayster, Muhammad Raffay, Quentin Justice, Zainab Al Tamimi, Gavyn Hansotte, Lavanya Devi Sunkara, and Jessica Bernat. Additive manufacturing: A comprehensive review. *Sensors*, 24:2668, 2024.